Phase-field modelling of diffusive dynamics of slowly miscible liquids

Ruilin Xie

Faculty of the Engineering and Environment

University of Southampton

This dissertation is submitted for the degree of

Doctor of Philosophy

Energy Technology Research Group

November 2017

Declaration

I hereby declare that except where specific reference is made to the work of others, the contents of this dissertation are original and have not been submitted in whole or in part for consideration for any other degree or qualification in this, or any other University. This dissertation is the result of my own work and includes nothing which is the outcome of work done in collaboration, except where specifically indicated in the text.

Ruilin Xie
November 2017

Acknowledgements

First of all, I would like to acknowledge my supervisor Dr Anatoliy Vorobev for offering me the opportunity to carry out this research. I appreciate and have been always benefited from his patient guidance, encouragement, prompt response and constant support. It couldn't be luckier to have a supervisor who cared so much about my work and thus I feel deeply grateful. I would also like to thank my supervisor Dr Anatoliy Vorobev for providing me with the opportunity of a three months research visit to the biomass energy research group in GIEC (Guangzhou Institute of Energy Conversion) and another three months research stay in the Perm state university. Meanwhile, I must also thank the supports of the EU Marie-Curie ECOFUEL Project and the Royal Society for the supports to these two trips to GIEC and the Perm state university. I also want to thank the host of GIEC and the Perm state university, and the academics and staffs in these two institutes for all the valuable supports they provided to me. I would also like to acknowledge the use of the IRIDIS High-Performance Computing Facility and associated support services at the University of Southampton in the completion of this work. Finally, I also want thank my examiners, Dr Edward S Richardson and Dr Ranga Dinesh Kahanda Koralage for the valuable insights and suggestions.

Abstract

The mixing of miscible liquids is essential for numerous processes in nature and industry. The rate of mixing is ultimately determined by the slow interfacial diffusion process that is initiated by the contact of two miscible liquids. The hydrodynamic flows near interfacial boundaries may strongly affect the diffusion process, sometimes resulting in deformation or even disintegration/disappearance of interfaces.

The mixing dynamics of miscible liquids remains poorly understood. The diffusion flux is traditionally defined through the classical Fick's law (i.e. with the diffusive flux being proportional to the gradient of concentration), which is only applicable to the cases of small concentration gradients. At least, at the moment of an initial contact of two liquids the concentration gradient across the interface boundary is strong, which renders the classical Fick's inapplicable for accurate description of this system.

To prove this statement, we have fulfilled the numerical studies of the recent experiment, in which the diffusive mixing of two miscible liquids was studied. The liquids were saturating a capillary tube. A visible liquid/liquid boundary was observed for prolonged time periods, and the time evolution of the boundary shape and its propagation dynamics were documented. Through the set of 1D, 2D, and 3D numerical simulations, we proved that the experimental observations cannot be reproduced on the basis of the Fick's law. Neither the shape of the liquid/liquid boundary nor its time dynamics have been correctly reproduced. We have added to the model the effects of hydrodynamic motion and surface tension (the Korteweg's term), and still the simulation results have remained different from the experimental observations.

Further, we have performed the simulations on the basis of the phase-field model. This time the diffusion process has been defined by the extended Fick's law, i.e. through the gradient of the chemical potential. In addition, the model included the capillary effects associated with the interface. We found that such an approach is capable of producing a realistic shape of the liquid/liquid boundary. However, the numerical predictions for the movement of the boundary have remained different from the experimental observations. With a hope to make the numerical results more aligned with the experimental observations, the hydrodynamic effects were added. Although, the flows induced in a capillary were too

weak, and, in particular, the experimental dependence on the tube's diameter have been not described by the flows.

Finally, we have tried to use even more sophisticated mathematical models, e.g. the models that were previously developed for explanation of diffusive dynamics in polymer systems, where the non-Fickian behaviour is also frequently reported. However, the attempted modelling (namely, the inclusion of viscoelastic effects) still has failed to provide the experimentally observed dependences.

To conclude we would like to state that the diffusive dynamics of miscible liquid/liquid interfaces cannot be explained by the classical Fick's approach. The phase-field approach can be used to provide the accurate shape of the miscible interfaces. Nevertheless, the diffusive dynamics of miscible liquid/liquid interfaces have remained poorly described and thus the further research work is suggested.

Table of contents

Table of contents ix

List of figures xi

1 Literature Review 3

1.1 Industrial applications . . . 4

1.1.1 Enhanced Oil Recovery (EOR) . . . 4

1.1.2 Enhanced Aquifer Remediation (EAR) . . . 8

1.1.3 Biofuel engineering . . . 9

1.2 Thermodynamics of non-equilibrium liquid/liquid mixture . . . 16

1.2.1 Phase behaviour of a liquid/liquid system . . . 18

1.2.2 Dynamic surface tension . . . 19

1.2.3 Diffusion in a liquid/liquid mixture . . . 22

1.2.4 Hydrodynamic flows near the liquid/liquid interface . . . 25

1.2.5 Wetting and contact line . . . 26

1.3 The mathematical model of the fluid flows in porous media . . . 28

1.4 Kinetic model of lipid extraction . . . 31

1.5 The mathematical model of the convective and diffusive evolution of the miscible liquids . . . 34

1.5.1 Molecular dynamics simulation . . . 34

1.5.2 The macroscopic description of the convective and diffusive evolution of the two liquids system . . . 35

1.6 Phase-field approach . . . 38

2 Mathematical model 43

2.1 Fick's law . . . 43

2.1.1 Fickian diffusion with hydrodynamics . . . 44

2.1.2 Non-Fickian diffusion . . . 45

2.2 Phase-field approach 48
2.2.1 Free energy function 49
2.2.2 Cahn-Hilliard model and Cahn-Hilliard-Navier-Stokes model . . . 52

3 Numerical procedure **57**
3.1 The model geometry and imposed boundary conditions 57
3.2 The vorticity-stream-function formulation 61
3.2.1 The finite-difference approach 65
3.3 1D and 2D model 68
3.4 3D model 69
3.5 Numerical accuracy of the model 70

4 Results and discussion **75**
4.1 Experimental results 75
4.2 Results for the Fickian model 78
4.2.1 1D model 78
4.2.2 2D model 78
4.2.3 3D model 85
4.3 Non-Fickian diffusion in polymers 92
4.4 Phase-field approach 93
4.4.1 Phase-field results 96
4.4.2 The parameter study of the phase-field model 100

5 Conclusion **111**

6 Future work **115**
6.1 Anisotropy 115
6.2 Non-isothermal effects 117

References **125**

List of figures

1.1 Water alternating gas EOR. 6
1.2 The scope of the combination of EOR and CCS project. 8
1.3 Hydrologic cycle. 9
1.4 The open pond raceway (a) and the closed photobioreactor (b). 11
1.5 Harvested algae biomass. 12
1.6 The experiment rig for the SCCO_2 extraction. 14
1.7 The experiment rig for the DME extraction. 15
1.8 A phase diagram. 19
1.9 The calculated result (the mass fraction of the amount of solvent entering the solute phase) for Fickian diffusion with a concentration-dependent diffusion coefficient [1]. 23
1.10 Wetting and contact angle. 27
1.11 Macromodels and micromodels. 29
1.12 Network models. 31
1.13 The sharp interface model and the diffusive interface model 37

2.1 A sketch of the Landau free energy function. 50
2.2 A sketch of the regular solution of the free energy function. 51
2.3 A sketch of the function of the chemical potential (Eq.(2.26)). 52
2.4 A flat interface between two fluids. 54
2.5 A sketch of Eq.(2.37)($C_0 = 0.5$). 55

3.1 The geometry of a single capillary tube. 58
3.2 The geometry of a single capillary tube with two blocks at both open ends. . 59
3.3 The schematic diagram of the iteration procedure to solve the vorticity field. 66
3.4 The geometry of the model. 70
3.5 The analysis of the accuracy of the mesh size. 72
3.6 The schematic diagram of the procedure to determine the size of the time step. 73

3.7 The mass of solvent penetrating into the capillary tube. 74

4.1 A sketch of the experiment configuration of the diffusion experiment that are going to be reproduced in our numerical work. 75

4.2 The observations of the shape of the glycerol(G)/water(W) interface reported in the experimental work [2]. The upper row and lower row show the interfaces entering into the tube from different sides of the capillary tube. 76

4.3 The rate of diffusion in glycerol/water reported in paper [2]. This figure shows the data measured under $20°C$. The figure also compares data under different tube diameters, namely, 0.6mm (the square symbols), 0.8mm (the orthodox triangles symbols), 1.2mm (the reversed triangles symbols), 1.6mm (the circle symbols). 77

4.4 The one dimensional concentration field for the Fickian diffusion. 79

4.5 The mass of solvent penetrating into the tube evaluated from the one dimensional Fickian model. 79

4.6 The average concentrations of the solute ($< C_1 >$) and solvent ($< C_2 >$) phases as the function of time. 81

4.7 The Fickian evolution of the solute/solvent mixture. 82

4.8 The mass of the solvent that penetrates into the tube as a function of time. . 83

4.9 The snapshots of the concentration field and vector field for the Fickian diffusion with the Korteweg force. 84

4.10 The mass of solvent that enters into the tube as a function of time. 85

4.11 The snapshot of the concentration field at 6000s (the gravity is neglected). . 86

4.12 The mass of solvent penetrating into the tube evaluated from the Fluent solver. (a) The mass of solvent penetrating into the tube as a function of time in normal scale; (b) The mass of solvent penetrating into the tube as a function of time in logarithmic scale. The solid lines are for results calculated from Fotran codes and the dashed lines are for results calculated from Fluent solver. 87

4.13 The snapshot of the concentration field for the dissolution under normal gravity ($t = 1000s$). 88

4.14 The evaluation of the mass transfer under gravity. (a) The mass of solvent penetrating into the tube as a function of time in normal scale; (b) The mass of solvent penetrating into the tube as a function of time in logarithmic scale. In both (a) and (b), dashed line is for 2D tube, dash-dot-dot line is for 3D tube, solid line is for 2D block, dash-dot line is for 3D. In (b), three reference lines are added to identify the time dependencies and their information are as follows: the solid line with square symbols is for $m \propto t^{1/3}$, the solid line with delta symbols is for $m \propto t^{2/3}$, the solid line with circle symbols is for $m \propto t^{1/2}$. 88

4.15 The snapshot of the concentration and velocity fields at the initial ((a) and (c), $t = 100s$) and later ((c) and (d), $t = 1000s$) time movements ($g = 9.8\frac{m}{s^2}$). The initial fields are similar to the profile of the lock-exchange flow. 89

4.16 The snapshots of the pattern of the lock-exchange flow reported in paper [3]. (a) the initial state; (b) the onset of the lock-exchange flow; (c) the pattern of lock-exchange flow at longer time period. 90

4.17 Dissolution in a 5 cm tube (normal gravity). 91

4.18 The mass of solvent penetrating into the tube as a function of time. (a) The mass of solvent penetrating into the tube as a function of time in normal scale; (b) The mass of solvent penetrating into the tube as a function of time in logarithmic scale. In both (a) and (b), solid lines are for tube diameter equals to 0.4mm, dashed lines are for tube diameter equals to 0.2mm. In (b), three reference lines are added to help identifying the time dependencies and their information are as follows: the solid line with square symbols is $m \propto t^{1/3}$, the solid line with delta symbols is $m \propto t^{2/3}$, the solid line with circle symbols is $m \propto t^{1/2}$. 92

4.19 Diffusion in the solvent/polymer mixture. 94

4.20 The mass of solvent penetrated into the tube as a function of time. 95

4.21 The evolution of the solute/solvent mixture modeled by the phase-field approach. The results are obtained for the rigid wall boundary conditions for the tube walls. (a,c,e) show the snapshots of the concentration and velocity fields at initial condition $t = 0$ and (b,d,f) show the results at $t = 0.03$. The results are shown for the single tube (a,b), for the block geometry without hydrodynamics (c,d); and for the block geometry taking into account the hydrodynamic flows (e,f). The parameters used for above cases are $A = -0.5$, $Ca = 10^{-4}$, $Gr = 1$. For (e,f), the additional parameters are $Pe = 10^4$, and $Re = 100$. (g,h,i) are the snapshots of the experiment observations of the glycerol/water interface reported in paper [2] ('G' represents the glycerol phase and 'W' represents the water phase). 97

4.22 The evolution of the solute/solvent mixture modeled by the phase-field approach. The results are obtained for the solute-philic boundary conditions for the tube walls. (a,c,e) show the snapshots of the concentration and velocity fields at initial condition $t = 0$ and (b,d,f) show the results at $t = 0.03$. The results are shown for the single tube (a,b), for the block geometry without hydrodynamics (c,d); and for the block geometry taking into account the hydrodynamic flows (e,f). The parameters used for above cases are $A = -0.5$, $Ca = 10^{-4}$, $Gr = 1$. For (e,f), the additional parameters are $Pe = 10^4$, and $Re = 100$. (g,h,i) are the snapshots of the experiment observations of the glycerol/water interface reported in paper [2] ('G' represents the glycerol phase and 'W' represents the water phase). 98

4.23 The mass transfer evaluated in the phase-field model (a) The mass of the solvent penetrating into the tube as a function of time. (b) The position of the liquid/liquid interface as a function of time. The mark "1" and "2"correspond to the results obtained for the tubes with walls neutral to both liquids and the results with the solute-philic tube wall, respectively. The results are plotted for $d = 0.1$, $A = -0.5$, $Ca = 10^{-4}$, $Gr = 1$, $Pe = 10^4$, and $Re = 100$ (the curves obtained for the cases with the included effects of hydrodynamics). The dash–dot–dot lines depict the results for the single tubes; the dashed lines for the block geometry without hydrodynamics; and the solid lines for the block geometry with hydrodynamics. (c) and (d) show the same results but in logarithmic coordinates. The thicker solid lines show the reference dependencies. 99

4.24 The average concentrations within the solute ($< C_1 >$) and solvent ($< C_2 >$) phases as a function of the time 100

4.25 The snapshots of the concentration fields for (a) $A = -0.1$, $Ca = 10^{-4}$, $Gr = 1$, and $t = 2.4^{-2}$ and (b) $A = 0.5$, $Ca = 10^{-4}$, $Gr = 1$, and $t = 2 \times 10^{-2}$ (c) $A = -0.1$, $Ca = 10^{-4}$, $Gr = 1$, $Re = 10^2$, $Pe = 10^4$ and $t = 6.24 \times 10^{-2}$, (d) $A = -0.1$, $Ca = 10^{-4}$, $Gr = 1$, $Re = 10^2$, $Pe = 10^4$ and $t = 3 \times 10^{-2}$. . . 101
4.26 The comparison between experimental and computational results. 103
4.27 For different values of the parameter A. 104
4.28 The shape of the interface for the cases of the neutral walls. 105
4.29 The shape of the interface for the case of the solute-philic walls. 106
4.30 The mass of solvent penetrating into the tube as a function of time for different values of the parameter Ca. 107
4.31 The effect of hydrodynamics on mass transfer. 108
4.32 The mass transfer in tubes of different tube diameters. (a) The mass of the solvent penetrating into the tube as a function of time. (b) The portion of the capillary occupied by the solvent phase vs time. The values of the tube's diameter have already been marked onto the relevant curves. (c) and (d) show the same results in logarithmic coordinates. The ticker solid lines show the reference dependencies. 110

Chapter 1

Literature Review

Mixing of miscible liquids plays a vital role in various applications, especially, enhanced oil recovery, CO_2 sequestration, aquifer remediation and solvent extraction. The miscible injection is considered to bring several advantages compared against the conventional water injection, including the recovery of the unrecoverable oil left after the water injection. It has been proved to be an effective method by various practical operators [4–6]. In addition, it [7] was also suggested that the miscible displacement has a potential usage if combined with the CO_2 sequestration to wash the abandoned oil reservoir and to increase the capacity of the CO_2 sequestration. The similar usage has already been also found in the application of the aquifer remediation where miscible liquids are frequently used to clean aquifers by removing unwanted chemicals [8]. The solvent extraction is another important application in food and biofuel engineering that is used to collect oil squeezed out from the feedstock (e.g. soybean, rice, cotton, sunflower seeds, and so forth.) in the extraction vessel [9].

The above paragraph briefly mentioned several important applications that involve miscible liquids. The details will be provided in the subsequent sections of this chapter where we aim to elaborate the importance of using miscible injection in different practical applications and we outline the mathematical model that were developed from diverse backgrounds. We have divided this chapter into three parts: 1, the applications that are based on miscible displacement; 2, the physics of non-equilibrium liquid/liquid mixture; and 3, the computational methods used to solve the problems.

1.1 Industrial applications

1.1.1 Enhanced Oil Recovery (EOR)

In petroleum engineering, the oil recovery is traditionally split into primary, secondary and tertiary recovery stages [10]. At the stage of primary recovery, the natural pressure in the reservoir is used to drive oil to the surface. This method becomes less efficient along with the oil production because the reservoir pressure decreases with time. Thus, the secondary recovery operation is required to maintain the reservoir pressure to displace oil. The most popular method at this stage is water flooding, in which, water is injected through the injection wells into the oil reservoir in order to displace oil toward the production wells. Injection of immiscible gas can be used instead of water, but it is less efficient and popular than the water flooding [11]. However, the water/oil displacement front is unstable: it breaks into a set of streams (fingering shape flow) leaving a significant amount of oil unrecovered. To increase the overall recovery, the tertiary recovery techniques need to be implemented. At this stage, surfactants, polymers, chemicals, miscible gases, thermal methods, and even micro bacterias may be used to increase the oil production [10]. The above description of oil recovery process implies a chronological sequence of three stages during oil recovery. However, practically, EOR can be used directly after primary production or even at the time of the primary recovery method due to the various conditions of oil reservoirs [10].

There are various methods of EOR designed to improve oil or reservoir characteristics to enhance the recovery. For efficient engineering applications, a good understanding of different oil recovery methods is needed. One of the most important factors to evaluate an method of EOR is the displacement efficiency. The displacement efficiency is defined as the product of the macroscopic and microscopic displacement efficiencies [10]. The macroscopic displacement efficiency refers to the effectiveness of the displacing fluid flows through the reservoir and the microscopic displacement efficiency refers to the effectiveness of displacing fluid to move the oil at the pore scale.

To increase the macroscopic displacement efficiency, efforts can be made to increase or maintain a proper mobility ratio between displacing fluids and oil [10]. The idea of the related EOR methods is to use surfactants, polymers and foams to obtain the preferred mobility [12]. In cases with a special geological formation, the density of the displacing fluid is also an important factor to affect the mobility ratio under the help of gravity [10].

To increase the microscopic displacement efficiency, efforts are made to obtain favourable phase behaviour between the displacing fluids and the phase of oil, such as lower interfacial tension, lower oil viscosity, oil swelling (oil volume expansion), and also miscibility with oil [13]. Common ideas of relevant method are to use chemicals [14], thermal energy

[15], steams [16], and also miscible liquids [17] to achieve the above goals. Other different EOR processes use microbial injection, fire flooding (through combustion) [18], ultrasonic transducers [19], pulsed plasma thruster [20], etc.

The selection of an EOR method should be made by taking into consideration of various information as the geological formation, oil properties, practical applicability, potential risk and also the cost [10]. For particle applications, there is a screening criterion to evaluate the feasibility of each EOR process for a specific oil reservoir [21].

Miscible displacement

One of the methods of EOR is the miscible displacement. The idea of this method is to generate a single phase out of oil and the injected fluid, which helps to displace additional oil blobs trapped in the pore structure. The method of the miscible displacement can be classified to be the “first –contact-miscible” (FCM) method and the “multiple-contact-miscible” (MCM) method. The “first–contact-miscible” method refers to the process of injection of a fluid that can be fully mixed with oil once they get into contact with oil [10]. Such fluids are often considerably expensive to use. The common displacing fluid selected for this method are the hydrocarbon gases (CH_4 or liquefied petroleum gases). Practically, to reduce the cost, the expensive solvent are only used to generate a miscible front, and then the secondary displacing fluid (normally cheaper solvents) is injected to keep the stability of the connection between displacing fluids. The final displacing fluid (normally water) are injected to move the miscible front [10].

Another variation of the miscible displacement is called the “multiple-contact-miscible” method. This method is to inject a fluid that may not be miscible or partially miscible with oil under normal condition but can be processed to achieve the so-called "multiple-contact-miscibility". The "multiple-contact-miscibility" can be obtained by enriching the immiscible fluids with other additives that are miscible oil and the ternary phase diagram is often used to analyse the phase behaviour [22].

The most popular example of miscible displacement is the CO_2 displacement. At the supercritical conditions, it is miscible with oil. The criteria for screening reservoirs for CO_2 EOR suitability published by the National Energy Technology Lab in the US is shown in Table.(1.1). It is used as a guide to determine whether the method of supercritical CO_2 EOR should be used.

In fact, EOR operations that use the supercritical CO_2 has one disadvantage. Compared with oil, the supercritical CO_2 has a much lower viscosity and lower density, so CO_2 will tend to over-run oil blobs. This implies the super-critical CO_2 flow may have a finger-shaped movement across the oil and hence leaves oil unrecovered like water flooding [10].

To improve this, one variation of this method, called the "water alternating gas" method, has been developed [10]. The idea is to inject water after the super-critical CO_2 front and maintain the stability of the phase and favourable mobility ratio [10, 23]. One example of such process is shown in Fig.1.1.

Table 1.1 The criteria for Screening Reservoirs for CO_2 EOR Suitability [24]

Depth, m	< 9800 and > 2000
Temperature, °F	< 250, but not critical
Pressure, pa	> 1,200 to 1,500
Permeability, md	> 1 to 5
Oil gravity, °API [1]	> 27 to 30
Viscosity, cp	$\leq$ 10 to 12
Residual oil saturation after water flood, fraction of pore space	> 0.25 to 0.30

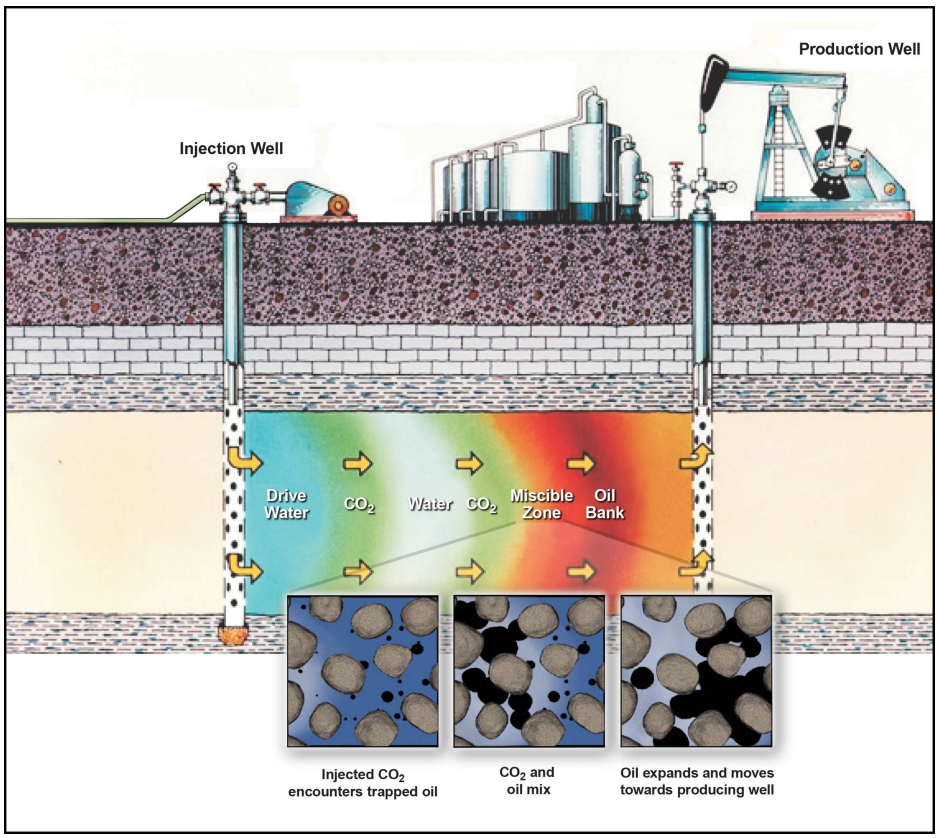

Fig. 1.1 Water alternating gas EOR[24].

The supercritical CO_2 was proved to be a successful method. Ref.[17] reviewed the development stage of all major EOR methods and it indicated that the super-critical CO_2

injection is becoming a favourable selection in various cases. Up to now, it has already been used in North Sea, Gulf of Mexico, Brazil, Malaysia, etc[4]. One of the largest miscible gas displacement project in the world is in the Prudhoe Bay, in where various miscible gas flooding methods were tested, and the vital experience and information were provided to improve the understanding of the flooding process [5]. In the North Sea, the result from two miscible water-alternating-gas (WAG) injection projects in Magnus and Ula in 2013 even shows nearly 100% of the total oil production can be attributed to WAG (In 2012, the value was 40%) [6].

The combination of the EOR with the carbon capture and sequestration

The CO_2 used for EOR can be captured from the human activities and this has a significant meaning in the sense of environment protection. To control the increment of the global average temperature, a growing attention is paid to the problem of carbon capture and storage (CCS). The wide deployment of CCS sites will provide the reliable source for the supercritical CO_2 EOR, and an idea to combine these two technologies have been raised in report [7].

The details about how to combine CCS and EOR are shown in Fig.1.2. The CO_2 is captured from the power plants and then be transported to the injection rig or platform by pipeline. A compressor is needed to bring CO_2 to the supercritical conditions. The compression process can be done onshore or offshore and depends on the practical requirements. The rest of the CO_2 can be stored in the geological reservoirs, which is the perfect location to store CO_2 [7]. In this sequestration process, the miscible displacement has a potential application to remove the hydrocarbons remaining in the geological storage and hence to increase the storage capacity for CO_2.

The report [7] evaluated the economic applicability of the process and stated that CO_2-EOR would be economic in North Sea oil fields at an oil price of US $70 per barrel if the issue of risks is ignored. If risks are taken into account, it would still be economic at an oil price less than US $100 per barrel. Since reducing CO_2 emission is a vital mission of protecting the environment and it is likely to get the subsidy from government or public, the CO_2-EOR may also be economic if the oil price is even less than US $70 per barrel [7].

[1]The American Petroleum Institute gravity, $API_{gravity} = \frac{141.5}{SG} - 131.5$, where SG=specific gravity at $288.706^{\circ}K$. For oil, $SG_{oil} = \frac{\rho_{oil}}{\rho_{water}}$.

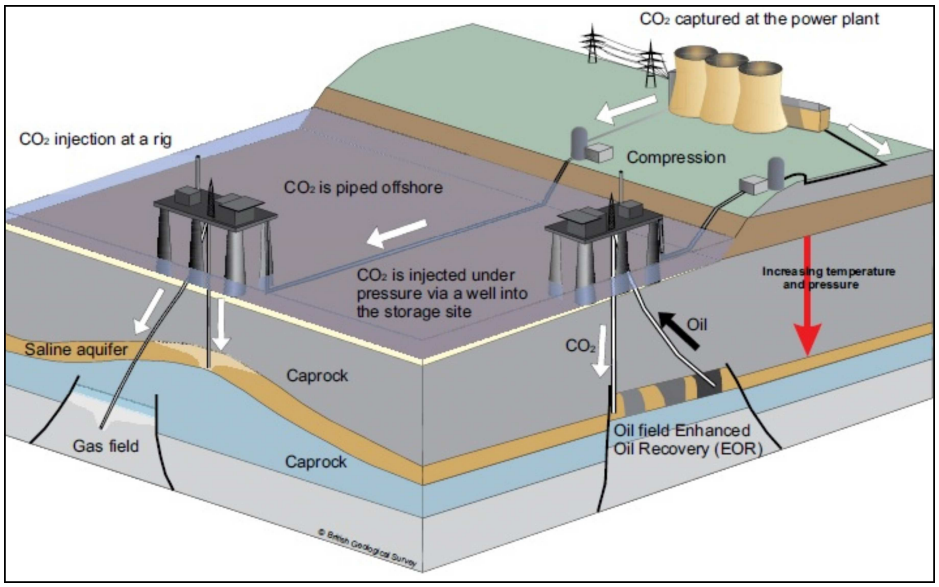

Fig. 1.2 The scope of the combination of EOR and CCS project [7].

1.1.2 Enhanced Aquifer Remediation (EAR)

The similar techniques have also been used in enhanced aquifer remediation (EAR). An aquifer is a layer of porous geological formation that contains groundwater [25]. This aquifer plays an important role in hydrologic cycle (In Fig.1.3), which affects various phenomena closely related to climate, environment, and nature. The quality and quantity of the groundwater are of great importance. Thus the managements on controlling withdrawal of groundwater, adding favourable chemicals and removing unwanted chemicals is important [26]. The groundwater can also be highly polluted by harmful chemicals released from industries, agriculture, and other human activities [8, 27, 28]. One type of these contaminants is called non-aqueous phase liquids (NAPLs) [26, 28]. As its name suggests, such contaminants are not miscible with water (aqueous phases). These NAPLs are also frequently classified as light non-aqueous phase liquids (LNAPLs) that are lighter than water (one typical example is oil or gasoline spillage) and dense non-aqueous phase liquids (DNAPLs) that are heavier than water [26]. The existence of NAPLs can decrease the hydraulic conductivity due to its gravity-driven motion and fingering-shaped motion in the unconsolidated geologic formation [28]. If the volume of NAPLs is relatively large, NAPLs can percolate downwards to the bottom of the aquifer under gravity effect. Due to the density difference, DNAPLs can even form a non-penetrating layer at bottom of the aquifer and hence largely reduce the hydraulic conductivity and storage capacity of an aquifer [26].

The aim of enhanced aquifer remediation is to remove these contaminants from the aquifer. One idea to clean these NAPLs is to increase its solubility in aqueous phases. In

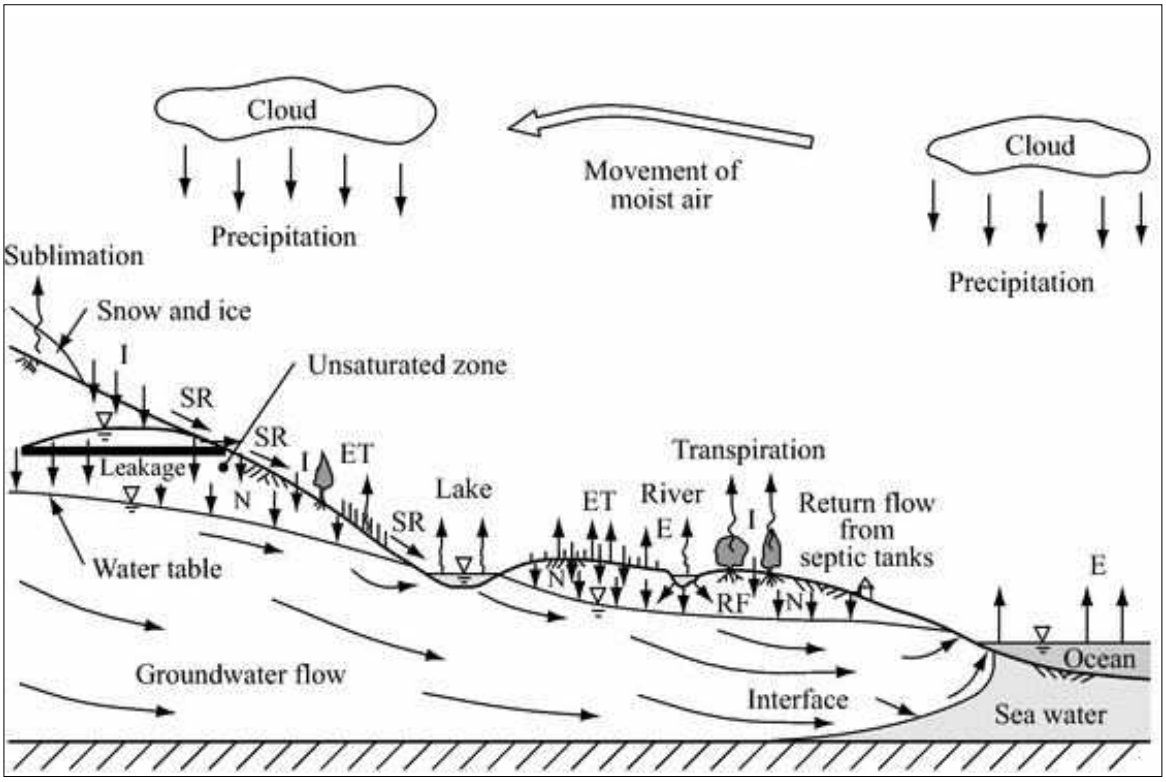

Fig. 1.3 Hydrologic cycle [26].

fact, some LNAPLs can be mixed with aqueous phases due to their volatility. Surfactants can also be added to increase such solubility [29]. For other NAPLs that are hardly solvable with aqueous phases, the particular chemicals can be added to transform the NAPLs to some favourable chemicals that can be mixed with water. One typical example of this method is advanced oxidation process (AOP), which is high effective to eliminate contaminants through Fenton or Fenton-like process [30]. One issue that should be noticed is that the selection of chemicals should be carefully made to stop releasing new contaminants.

1.1.3 Biofuel engineering

The utilisation of conventional fossil fuels brings serious environmental pollution. The main renewable solutions to both the energy crisis and adverse environmental problems, to a large extent, are the clean energy (e.g. solar energy, wind energies, hydropower, etc.) and biofuels [31]. The biofuel has been foreseen as a promising solution not only because it is a renewable and eco-friendly method, but also due to its enormous benefits as fuels. There are various machines that rely on the combustion of fossil fuels (e.g. cars). The electricity produced from clean energy sources cannot directly provide power for these machines.

However, biofuels and fossil fuels are alike and hence these machines can be used without serious modifications.

There are various sources for biofuels, which are usually classified into four generations of biofuels [31, 32]. The first generation refers to the biofuels produced from food crops. One controversial issue here is the economic conflict between the biofuel production and the food crisis which is also an urgent problem to the world [32]. The second generation biofuels come from the non–food sources such as agricultural residual biomass and waste cooking oil that can be converted to bioethanol and biodiesel. The third-generation biofuels are algae-based biofuels and these use wastewater or gas as the source. Plus, algae are richer in lipid-content than other biofuel feedstocks [33]. The fourth generation biofuels are obtained from captured carbon [31]. This is similar to the third generation biofuels. The only difference is that the algae used in this process are genetically modified to have the ability to capture a higher amount of carbon dioxide from waste gas. However, this has a specifical meaning in the sustainable development because energy can be produced from waste. These facts indicate that algae is a promising source of renewable energy for the future. Nevertheless, both technical and economic barriers still exist.

As biofuels can be obtained from various kinds of biomaterials, different regions in the world can develop biofuels derived from their bio-products. The initial oil extracted from bio-materials is the basic vegetable oil and then such oil will need to be converted into biodiesel through the process of transesterification [31]. Currently, the traditional fossil fuel still has advantages in its quality when compared with biofuel. The fuel properties of most biofuels largely depend on the properties of biomaterials and the desirable properties of fossil fuel can be obtained along with the development of suitable biomaterials and transesterification technologies [31]. The biofuel can also be used as a mixture of fossil fuels with adding advantages such as safer and easier transportation or storage can be added due to their higher flash point [34].

Algae Cultivation

The algae-based biofuels require the special facilities to cultivate algae and the most common facilities for algae cultivation are the open raceway pond or the closed photobioreactor (In Fig.1.4) [35, 36]. The open raceway ponds are the simple and common facilities for the algae growth. They are cheap and easy to operate but some parameters such as temperature, light and CO_2 conditions are difficult to be accurately controlled. In a closed photobioreactor system, such conditions can be accurately controlled to increase the biomass productivity [35]. The closed photoreactor has several different designs, e.g. a tubular photobioreactor, a flat plate photobioreactor and a column photobioreactor [36].

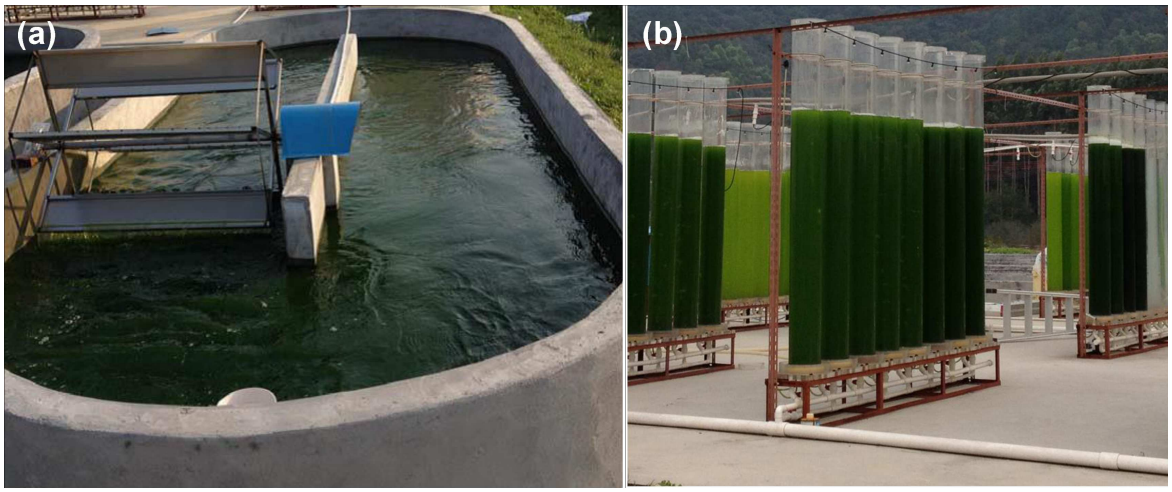

Fig. 1.4 The open pond raceway (a) and the closed photobioreactor (b).

The advantages of the algae-based oil are: (a) algae contains high quantity of lipid and (b) algae itself can be cultivated in waste water because waste-water usually contains nitrogen and phosphorus needed for the growth of algae [37]. Dilution is normally needed because the concentration of nitrogen and phosphorus in most sources of the waste water is too high for the growth of certain kinds of algae, This requires a larger quantity of water, that increases the overall cost [37]. Algae cultivation itself is a challenging problem and the knowledge about how to cultivate algae with fast growth rate with sufficient lipid content or to develop the new species of lipid-rich algae that can grow with sufficiently fast growth rate is always required [31].

Once algae have been harvested, the initial dehydration process is done through flocculation, centrifugation and filtration (In Fig.1.5). The obtained biomass can be used to generate energy (heat or electricity) through digesting and combustion [38]. If the resultant combustion gas can be reused in the algae cultivation, a short and sustainable cycle can be created. It is also believed that the other remaining biochemical compositions contained in algae can be used to develop other products for pharmaceutical industries [35].

Lipid extraction from algae biomass

The lipid extraction is done by crushing plant materials to produce the vegetable oil. The most basic method of biofuel production is the simple mechanical pressing. However, the mechanical pressing is not effective in lipid extraction from algae and ultrasound or microwave exposure is normally added for higher extraction rates [39]. According to the ultrasound and/or microwave assisted oil extraction experiments from seaweed [40], the extraction time can be reduced from 8 hrs to 0.5 hrs. In another research [41], it is also

Fig. 1.5 Harvested algae biomass.

reported that the lipid extraction from green algae (Scenedesmus obliquus) can be reduced to 30 mins with the help of the microwave.

For algae-based biomass, a problem is that the algae biomass is extremely wet (even after flocculation, centrifugation and filtration) and hence the drying process is always needed. The common drying methods are autoclave method under a high temperature [42, 43] or freezing pre-treatment methods [42]. The ultra-sonication and microwave can also be used in this process to improve the dehydration [43]. Ashokkumar's group [43] compared the effect of different drying methods on the lipid extraction of B. braunii and indicated that the highest lipid extraction is obtained with the use of the ultrasonic pre-treatment. However, another research shows the highest lipid extractions for Botryococcus sp, Chlorella vulgaris and Scenedesmus sp are obtained when microwaves pre-treatment is used [39].

The extraction can also be done through the chemical method by using solvents. This process can be quite different as the cell disruption happens simultaneously with extraction. In fact, the cell disruption can be done prior to extraction through various pre-treatment methods, namely, autoclaving, bead-beating, microwaves, sonication, osmotic shock [44]. The experiment with a comparison of different pre-treatment methods showed that the pre-treatment affects the efficiency of extraction and the effect of the pre-treatment varies with

the algae species [44].

The solvent extraction is normally considered as an easy and cheap method, but it consumes a relatively long extracting time (18 hrs) [35]. The possible explanation of this is the mixing between lipid and the solvent stopped after the concentration of penetrated lipid outside the cell reaches an equilibrium state with lipid concentration in algae [35]. Such limitation can be solved by using continuous organic solvent extraction method, but the cost then significantly increases. Furthermore, the possible solvents, like hexane, chloroform and acetone, are toxic. All these effects limit the usage of solvent extraction. The other solvents, such as, difsoxhlet, dichloromethane, chloroform–methanol (2:1), acetonitrile, toluene, isopropanol, n-hexane-diethyl ether (1:1), THF, 1-4-dioxane and n-hexane, have been experimentally studied in Ref.[43].

The ionic liquid is another chemical solvent that can be used for lipid extraction. The ionic liquid is the salt in the liquid state and hence is composed of ions. It is believed that the ionic liquids can change the molecular structure of the cell wall through the intermolecular interaction between ions in liquids and hydrogen bonds on cell walls [45]. In addition, the ionic liquid has various desirable properties such as non-volatility and thermal stability [39], which make the reuse or recovery of chemicals to be possible [45]. In [45], the ionic liquids $[Emim]OAc$, $[Emim]BF_4$, and $[Amim]Cl$ has been tested and the results showed the highest extracted quantity of lipid of 250.0 mg/g cell was obtained through using [Emim]OAc on C. vulgaris (The total fatty acids content was 292.2 mg/g cell) [45]. Experiments were performed under $65°C$ for 18 h and $120°C$ for 2 hrs, indicating higher temperature can reduce the extraction time [45]. The pure ionic liquid may be replaced by the molten salt/ionic liquid mixtures to reduce the amounts of expensive ionic liquid used. The comparisons between single ionic liquid and the molten salt/ionic liquid mixtures indicate that the molten salt/ionic liquid mixtures with a suitable ratio can even improve the lipid extraction yield rate [46].

Another method of lipid extraction is the supercritical extraction usually by using CO_2 at temperature and pressure above its critical values ($31.1°C$ and 7.39 MPa) [47, 48]. The supercritical fluid can be used to extract oil due to its high solvent power under the supercritical conditions. One big advantage is a much easier separation of the solute and solvent that can be achieved simply by the pressure reduction. Such advantage would provide some conveniences in the subsequent biodiesel conversion. The oily compositions extracted through normal solvent extraction method would remain in the solvent's layers after extraction, and hence need to be separated normally through evaporation. The supercritical fluid extraction can be 5 or 6 times faster than solvent extraction. Through changing the experimental condition (temperature and pressure), the 100% lipid yield rate can be obtained for certain

kinds of algae [49]. In the work [50], the residue lipid in the tissue was extracted for 90 mins by using an extra treatment with 200 ml 6 N hydrochloric acids at $100^{\circ}C$.

Unlike other organic solvents, CO_2 has non-polar molecules. To extract the complex compositions such as polar lipids, free fatty acids (FFAs) and some other unidentified compounds contained in algae, the yield performances of the SCCO_2 extraction can be improved by adding ethanol [43, 50]. The supercritical fluid extraction can also be used with pure dimethyl ether. The subcritical dimethyl ether (DME) extraction can even be used for the extraction of lipids from wet algae due to its high affinity to oily composition as well as its miscibility with water [51].

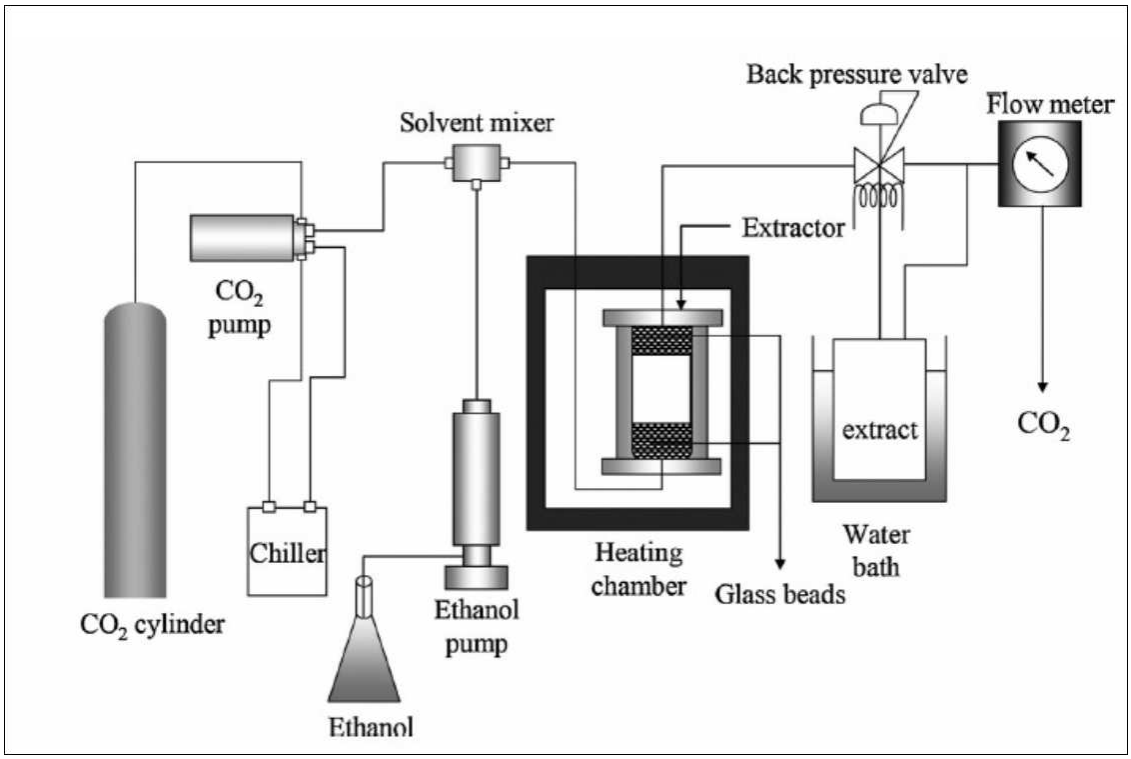

Fig. 1.6 The experiment rig for the SCCO_2 extraction. [47]

The experimental set-ups of supercritical extraction method are shown in Fig.1.6 and Fig.1.9. The microalgae are placed in a heating chamber (or oven) at a high temperature for drying. After the drying process, the CO_2 in super-critical condition is mixed with other solvent e.g. ethanol (In Fig.1.6). The experimental set up for solvent extraction or multi-solvents extraction is similar to the apparatus in Fig.1.6 with CO_2 and ethanol to be replaced by the relevant solvent. For cases where subcritical dimethyl ether is the solvent (The approximate condition can be 0.59 ± 0.02 MPa and 298.15 ± 1 K) [51], the sketch of the experimental rig is shown in Fig.1.9. Then the lipid extraction process will happen in

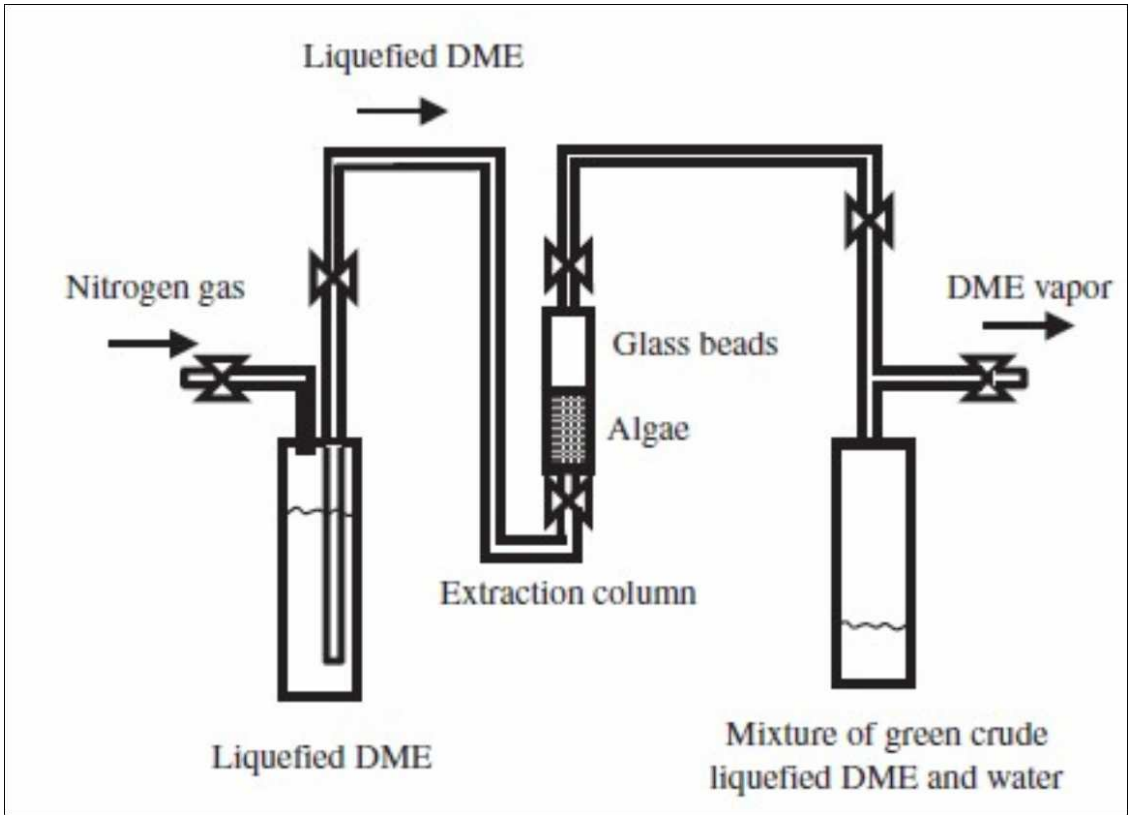

Fig. 1.7 The experiment rig for the DME extraction. [51]

the chamber. The biggest advantage brought by DME is the drying process and even cell disruption due to its extremely high affinity to oily compositions.

The development of the algae-based biofuel production is still at a very early stage. The waste water treatment plants using algae ponds or photobioreactor are operated by some companies confirming that the algae-based biomass can be successfully obtained [52]. However, the extraction of biofuel from algae biomass still needs further improvements. The comparison between different extracting methods indicates [39]. The technologies like the microwave and ultrasonic can enhance the extracting but will also increase the cost. The solvent extraction is also not cheap as plenty of expensive solvents is used. The cheaper solvent can be used when using supercritical extraction but the cost for facilities and potential risk will increase due to the extremely high pressures is applied. One economic analysis for large-scale Algae biofuel production system has proposed a hexane extraction process with a large extraction plant ($4,000$ metric tonnes/day) [52].

1.2 Thermodynamics of non-equilibrium liquid/liquid mixture

In above sections, we introduced the applications where the mixing of two miscible liquids is important. In this section, we want to introduce the thermodynamics of miscible liquid. The phenomenological law to describe mass transport is traditionally defined by the classical Fick's law, which assumes the driving force is given by the gradient of concentration. Diffusion occurs due to the random motion of the molecules. The rate of diffusion is determined on the basis of the Fick's law:

$$\vec{j} = -D\nabla C. \tag{1.1}$$

Here, C is the solute concentration, which is defined as the mass fraction of solute in a mixture. D is the diffusion coefficient. The evaluation of the rate of diffusion is based on the measurements of the diffusion coefficients. There are the self-diffusion coefficient and the mutual diffusion coefficient. The self-diffusion coefficient is for a pure fluid and the mutual diffusion coefficient is for a binary mixture. In book [1], the self-diffusion coefficient is written as:

$$D = \frac{D_0 C}{RT}\frac{\partial \mu}{\partial C}, \qquad D_0 = \frac{RT}{\eta}. \tag{1.2}$$

Here, D_0 is the self-diffusion coefficient when the chemical potential field is uniform, μ is the chemical potential of the fluid, R is the ideal gas constant, T is the temperature, and η is

the resistance coefficient (in book [1], it is assumed that η depends on the chemical composition). The mutual diffusion coefficient is predicted through some expressions that derived from the self-diffusion coefficient [1, 53]. Both the self and mutual diffusion coefficients are measured experimentally and compared with theoretical expression [1].

The diffusion coefficient for a binary liquid/liquid system can be predicted by the Stokes-Einstein model but this approach was however reported to be inaccurate when applying to mixtures with strong concentration differences, such as alcohols [54]. For the mixture with strong concentration gradient, the coefficient of diffusion depends on the solute concentration ($D(C)$). A particularly strong dependence of the diffusion coefficient on concentration allows producing a sharp diffusion front.

This in particular, has been demonstrated in the experiments that were recently set up with the aim to derive the fundamental understanding of how the diffusion through the solute/solvent boundaries happens [2]. The settings of the experiments are simple: a long capillary tube was saturated with one liquid (solute) and then immersed into a solvent-filled thermostatic bath. The left and right sides of the tube were open. The tube was placed in the bath horizontally, and no pressure gradients between the tube ends were applied. The experiments were conducted with different liquids, in particular with the glycerol/water and soybean oil/hexane binary mixtures. The common expectation of this process is that the solute/solvent boundaries should be motionless and should just slowly smear to form a homogenous single-phase system. In contrast with such expectation, the interface between liquids remained visible for very long time periods (about 1hr). It was seen that two interfaces, from two sides of the tubes, were moving towards the middle of the tube. The speed of the interface movement was time dependent, with $t^{-\frac{1}{3}}$ time dependence in the beginning and $t^{-\frac{2}{3}}$ time dependence at later time moments. Such results cannot be explained by the classical Fick's law which predicts the rate of diffusion is $\frac{1}{2}$ time dependence. The rate of interface propagation was found to depend on the tube's diameter (but did not depend on the tube's cross-section), so the dissolution occurs slower in the tubes of smaller diameter. The convective flows were found negligible, concluding that the evolution of the interface was diffusion-dominated.

In fact, the Fick's law would support the common expectations that the interface should just smear in time. That is the reason why the experimental observations reported in paper [2] cannot be explained on the basis of the classical Fick's law. For the liquid/liquid mixture, the new phenomenological law that defines the diffusion rate through the gradient of chemical potential rather than the gradient of concentration is frequently used. This phenomenological law will be accepted in the current work.

In most applications, the diffusion occurs along with the convection. The condition of

pure diffusion is difficult to be kept and convection frequently occurs along with diffusion [55]. By convective motion we understand that the fluid flows driven by gravity and concentration inhomogeneity, which may result in either buoyancy forces or in Marangoni forces (through dependence of interfacial stress on concentration). The details of above mentioned phenomenon is introduced in this section.

1.2.1 Phase behaviour of a liquid/liquid system

Firstly, we would like to start with the phase behaviours in a liquid/liquid mixture. Depending on the miscibility, the miscible liquid/liquid mixture can be divided into the fully miscible liquid/liquid mixture and the partially miscible liquid/liquid mixture. The fully miscible liquid/liquid mixture consists of two liquids that are miscible under all conditions, while in a partially miscible liquid/liquid mixture, the two liquids is not miscible (or not miscible in all proportions) under certain temperature or pressure. The phase behaviour of a partially miscible liquid/liquid mixture needs to be described and this can be described by the phase diagrams of the pressure-temperature (P-T), temperature-composition (T-C), or pressure-composition (P-C).

The phase diagrams demonstrate the partial miscibility of a binary liquid/liquid system depends on pressure and temperature. When a binary liquid/liquid mixture is non-homogeneous at equilibrium state, the temperature, pressure, and chemical potential of each phase are equal. It should be noticed that these equilibrium conditions are obtained for the non-homogeneous mixture (liquids do not mix). The chemical potential of each phase can be expressed by a function of pressure and temperature, and this means the equilibrium of such mixture can only be obtained at certain groups of temperature and pressure, i.e. at one constant temperature or pressure, the mixture can only be reached under particular pressure or temperature [56]. In a P-T diagram, the equilibrium curve consists of various equilibrium points (P,T) shows that the mixture is non-homogeneous at the curve and homogeneous if its pressure and temperature is away from the curve.

The partial miscibility can also be described by a P-C diagram at a fixed temperature or a T-C diagram at a fixed pressure (See Fig.1.8). Thus, to specify a state of the binary mixture, three quantities (i.e. pressure, temperature and concentration) are required. Although the binary mixture only consists of two components (fluids), there are eight different situations and they are described by ten different phase diagrams [56]. The terminate point of curves in a T-C diagram (Fig.1.8) or a P-C diagram is called the critical point. The pressure and temperature at critical point is called the critical pressure and critical temperature. Above this point, the system is homogeneous in equilibrium.

At beginning of the section 1.2, we mentioned the non-Fickian behaviours reported in

the experiment [2]. In the experiment [2], the mixture of two fully miscible liquids (glycerol/water and soybean oil/hexane) and the mixture of two liquids with a limited solubility (IBA/water) were examined. The glycerol/water and soybean oil/hexane mixture are miscible in any proportion. The IBA/water mixture is miscible at temperature above its critical point and is immiscible when the mixture temperature is below the critical point. The phase diagram for this situation is sketched in Fig.1.8.

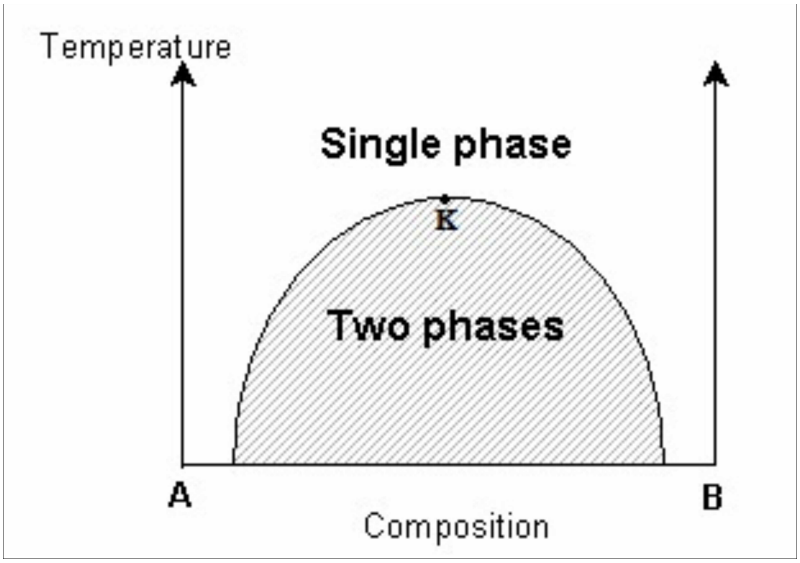

Fig. 1.8 A phase diagram. The liquids are miscible (from a homogenous mixture) at temperatures above the critical point K and the liquids are not miscible at temperature below the critical point K [56].

1.2.2 Dynamic surface tension

When a liquid/liquid mixture is heterogeneous, the phases are separated by interfaces. Various experimental observations (e.g. shape of the droplet, vortex ring, dips on the plate, etc.) indicate that the liquid/liquid interface is endowed with surface tension [57]. The surface tension is believed to be able to maintain the shape of the interface and its relation is expressed by the Laplace expression [58]. Frequently, the surface tension effects compete with gravity. However, for a smaller droplet (with the radius smaller than the capillary length), the surface tension dominates the shape of the liquid/liquid interface determined by the balance between these two forces [58].

The standard and direct measurement of surface tension can be done through the Wilhelmy's method which places an object (normally plate or fibre) on an interface and measures the force exerted on this object [58]. The spinning droplet tensiometry is another

popular method to obtain the shape of the interface of a spinning droplet and then to derive the surface tension through the shape of the interface [58]. This method has many similar variations by observing the extending droplet or any other rising liquids. Another group of methods to measure the surface tension focused on the capillary waves generated by injecting liquids (light scattering may be used to distinguish capillary waves) [58]. Two possible methods of this group are the drop weight method and the oscillating jet method [59]. The details of these two method are introduced in the review [59]. In both methods, it involves a procedure to form a capillary wave by injecting fluid, which introduces the flows to the system. Thus the result from such method is not reliable because of the hydrodynamics [59].

Most measurements of the surface tension are carried out for immiscible liquids, i.e. when the liquids in contact are in the state of thermodynamic equilibrium and the static surface tension coefficient is determined [60]. For miscible liquid/liquid mixtures, the surface tension at the liquid/liquid boundary changes dynamically over the process of dissolution. There are only a few measurements of the surface tension coefficients for miscible liquid/liquid mixtures, which were reviewed in paper [60]. In this paper [60], it is concluded that the Wilhelmy's method is not capable of measuring the dynamic surface tension and the method of capillary wave is not reliable.

The dynamic surface tension is normally measure via the method of droplet (spinning, expending, rising, etc.). The accurate measurements of the variation in a value of the surface tension should be much slower than the typical time needed for measurements. However, for spinning droplet tensionmeter, the droplet usually shrinks in size twice over the duration of the measurements [61].

The earliest studies of the surface tension for the miscible interfaces were done with the research methodologies similar to those for immiscible interfaces [62]. Petitjeans and Maxworthy [62] carried out an experiment using the glycerol-water/glycerol mixture to demonstrate the existence of the surface tension between miscible liquids. They [62] also checked the differences between the miscible interfaces and immiscible interfaces. In their experiment, the glycerol-water mixture was pumped into a horizontally placed capillary tube initially filled with glycerol. A fingering front was observed when water enters into the glycerol phase. The experiments were done with different glycerol-water mixture (with different densities and viscosities) and the results show that the displacement front is affected by gravity. The experiments were fulfilled with tubes of different diameters. The gravitational instability of the interface was always observed and this means the interfaces in miscible systems behave similar to the immiscible interfaces. They also mentioned this phenomenon is not observed when the tube's diameter is less or equal to 1mm. This was

explained theoretically demonstrating that the unstable perturbation for the gravitational instability is limited by the values around 1mm.

Petitjeans and Maxworthy's experimental result [62] were reproduced by the computational simulation based on the classical Fick's law [63]. Despite the good agreement have been achieved, it should be noticed the effect of strong flow was formed in both their experiments [62] and the computational calculations [63]. In the work [63], the miscible dissolution in the liquid/liquid mixture was described by the Stokes equation coupled with the Fick's law for species transport. The profile of the flow is assumed to be the Poiseuille flow. The parameters that affect the results are, namely, the Peclet number (define the ratio between the rate of convection and the rate of diffusion), the gravity parameter, and a parameter related to the viscosity of liquids. They [63] reported that the fingering shaped flow was observed when the large Peclet number (larger than 10^3 and close to ∞) is used, and when a small Peclet number (Pe=100) was used, the sharp fingering shape was no longer observed and the diffusion front slowly smeared. Furthermore, they studied the effect of a pre-existed solvent film on the tube walls of the capillary tube on the displacement [64] and also extended the their simulation to three-dimensional case [65].

Pojman's group [66] measured the surface tension on a miscible liquid/liquid interface by the spinning droplet tensiometry technique. They examined the isobutyric acid(IBA)-water and the 1-butanol-water mixture. They observed the sharp interface separating two phases, which is the evidence of the existence of the surface tension in the miscible liquids. The time-dependent surface tension for both the isobutyric acid(IBA)-water and the 1-butanol-water mixture were obtained under different spinning rates and temperatures. They also [66] reported the observation of the Rayleigh-Tomotika instability when the spinning rate rapidly changed. The phenomenon of instability is related with the hydrodynamic flows at the interface. We will introduce it in the corresponding section.

For the mathematical modelling of the miscible liquids system, Korteweg firstly suggested to express the surface tension based on the gradients of concentration [57],

$$P = P_0(C,T) - \frac{\varepsilon}{2}(\nabla C)^2, \tag{1.3}$$

and the equation of momentum balance changes to be,

$$\rho\frac{d\vec{v}}{dt} = -\nabla\left(P_0 - \frac{\varepsilon}{2}(\nabla C)^2\right) - \nabla\cdot(\varepsilon\nabla C\otimes\nabla C) + \nabla\cdot\sigma. \tag{1.4}$$

Here, P_0 is the pressure in the bulk phase, $\varepsilon\nabla C\otimes\nabla C$ is the Korteweg stress tensor, and σ is for the viscous force.

1.2.3 Diffusion in a liquid/liquid mixture

When two miscible liquids get into contact, the process of mass transfer occurs between two phases, making the composition of the mixture eventually uniform through the entire volume of the mixture. This equalization process is known as diffusion. The diffusion flux (the amount of the components transferred per unit area and per unit time) is traditionally evaluated by the concentration gradient, which is known as the classical Fick's law,

$$\vec{i} = -D\nabla C. \tag{1.5}$$

Here, D is called diffusion coefficient. This relation has been confirmed in the gaseous mixture. However, for diffusion in a liquid/liquid mixture, the driving force for diffusion of each species is the gradient of chemical potential of this species [67]. Such relation is known as the extended Fick's laws,

$$\vec{i} = -\nabla\mu. \tag{1.6}$$

The rate of concentration change of the mixture is evaluated by substituting the diffusion flux into the equation of mass balance, which can be written as,

$$\frac{C}{dt} = -\nabla\vec{i}. \tag{1.7}$$

The rate of mass transfer is transitionally known to be proportion to $\sqrt{Dt}$. According the textbook [1], the $t^{\frac{1}{2}}$ law is only applied for the early stages of the diffusion process. For the problem considered in paper [2], i.e. the solvent enters into a horizontal tube filled by solute, the period of the early times refers to the moments that the concentration at the centre of the tube remains to be the equal to the solute concentration. The time period of the early times is estimated as $\frac{1}{12} \approx 0.083t$ (here, t represents the non-dimensional time scale for the Fickian diffusion and it is expressed as $t = \frac{L^2}{D_0}$, where L and D_0 are the typical length and the diffusion coefficient.). The time period after $\frac{1}{12}$ is the later times of diffusion.

The rate of diffusion follows a different relation, which is known and has been formulated in the book [1]. The evaluation of the later stage requires calculating a new value, i.e. the concentration variation in the centre of the tube. Hence, the time-dependence of diffusion at later times cannot be decided directly. Nevertheless, it is possible to show the direct look of the behaviours at later times (in Fig.1.9). It can be seen that the time-dependence of the later times (after the time scale of $\sqrt{\frac{1}{12}} \approx 0.29$ in Fig.1.9) are rather closed to $t^{\frac{1}{2}}$ except the end of the diffusion process where the curves is just becoming flat. Thus, the

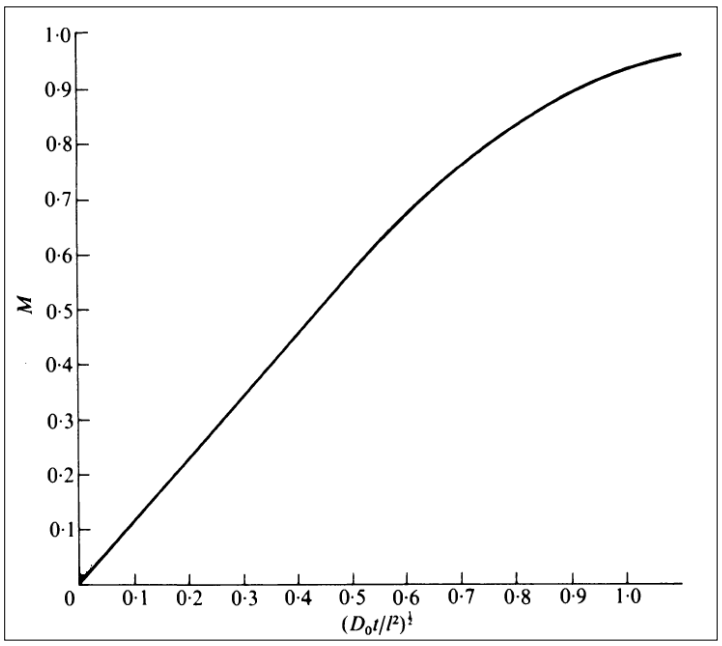

Fig. 1.9 The calculated result (the mass fraction of the amount of solvent entering the solute phase) for Fickian diffusion with a concentration-dependent diffusion coefficient [1].

time-dependence of diffusion rate for the Fickian diffusion is mainly $t^{0.5}$. This, however, was observed to be untrue for liquid/liquid mixtures [2].

With the help of the concentration dependent diffusion coefficient, the classical Fick's law is still widely used to explain the diffusion experiment of liquid/liquid mixture. For instance, Petitjeans and Maxworthy [62] measured the values of diffusion coefficient for the glycerol/water mixture and expressed the diffusion coefficient as a function of concentration. The diffusion experiments were even conducted in the space station in order to get rid of the gravity effect [68]. In paper [68], a series of diffusion experiments of the honey/water mixture and the diluted honey/water mixture was conducted under micro-gravity condition. Firstly, the pure honey was injected into the water and the fingering shape of the honey phase was observed. This interface was reported to be very stable and there was no observation of the Rayleigh-Taylor instability. Then the pure honey phase was replaced by the diluted honey (honey: water=1:4) and repeated the same procedures. The fingering shaped boundary was not observed and it was explained by the similarity between two contacting phases. Then the experiment was continued by injecting water into the diluted honey phases. The pure water phase was observed going upward of tube.

Diffusion between two miscible liquids was also studied with the help of the Wiener's method [69], i.e. the laser line deflection method (LLD). Instead of the optical techniques based on capturing the optical differences in laser line representing different phases, the

deflection of light was used to distinguish different phases [70]. Viner and Pojman conducted a group of experiments with miscible liquids by using the Wiener's method [69]. The experiment examined the isobutyric acid/water mixture and the 1-butanol/water mixture. For the isobutyric acid/water mixture under the temperature above the critical point (when both liquids are miscible in all proportions), the spreading of the droplet occurred with the rate $t^{0.06}$ into the direction of the isobutyric-acid-rich phase. For the mixture of 1-butanol/water, the spreading rate was proportional to $t^{0.09}$. The diffusion experiment in miscible liquid/liquid system is also extended to polymer/monomer mixtures. Diffusion in such mixture is frequently reported to be non-Fickian. The paper [71] also experimentally studied the diffusion in the mixture of dodecyl acrylate. In the work [71], the non-Fickian diffusion was observed for 30 to 50 mins and then the dissolution followed the Fickian time dependence.

It should be noticed that the interfacial diffusion could bring the medium to be anisotropic. In paper [72] and paper [73], the molecular dynamics simulations were used to evaluate the diffusion at liquid/liquid interfaces. The diffusion coefficient of each phase is calculated through the average mean square displacement of the molecules [72] or from the corresponding profile of the velocity of molecules [73]. In both works [72, 73], the calculated diffusion coefficient was observed to be anisotropic at or near the interface: at the bulks the two liquids system, the values of the diffusion coefficient are similar in all directions; while at the interface, the diffusion coefficient normal to the interface is observed to be around twice smaller than the diffusion coefficient parallel to the interface.

Diffusion can be induced by the thermal effect (Soret diffusion) and the gradients in pressure (barodiffusion). The non-homogeneities in pressure can be caused by gravity or capillary effects. If these effects are taken into account, the equation of the diffusive flux is written as [74, 75]:

$$\vec{j} = -\rho D \left(\nabla C + \frac{k_T}{T} \nabla T + \frac{k_p}{p} \nabla p \right). \tag{1.8}$$

Here, the second term at the right-hand side refers to the thermal diffusion effect and the third term at the right-hand side refers to the barodiffusion effect. k_T and k_p are the thermal diffusion ratio and the barodiffusion ratio, respectively. T is the temperature, and p is the pressure. In the work [75], the effect of barodiffusion is expressed by:

$$\nabla C = \frac{k_p}{p} \nabla p = \frac{k_p}{p} \rho \vec{g}. \tag{1.9}$$

Here, ρ is the density and $\vec{g}$ is the gravity acceleration. $\nabla p = \rho g$ means the variation in the pressure field is caused by the gravity force. A series of experiments were conducted to

assess the thermal diffusion [74] and the barodiffusion [75].

Pojman's diffusion experiments with the honey/water mixture on the space station [68] were also repeated with the variation in the temperature to study the effect of thermal diffusion. Because the experiments were done under the micro-gravity conditions, the effect of barodiffusion was negligible. In the work [76], barodiffusion was studied under the isothermal condition. The kinetic equation of the diffusive process is written as:

$$\frac{\partial C}{\partial t} = D\frac{\partial^2 C}{\partial x^2} - mF\frac{\partial C}{\partial x}. \tag{1.10}$$

Here, m is the mobility of the molecules of the dissolved fluid, and F is the gravitational force (or other external forces). The experimental work reported in paper [76] measured the diffusion coefficient entering into Eq.(1.10) and the effect barodiffusion is used to explain the non-Fickian diffusion part.

1.2.4 Hydrodynamic flows near the liquid/liquid interface

The hydrodynamic flows at the solute/solvent interface can be induced by the gradients in the surface tension induced by temperature or concentration variations. Such flows are known as Marangoni flows [77]. The first observation of the Marangoni effect was reported in the alcohol/water mixture [77] and the phenomenon is also known as the "tears of wine" because of the shape of the fingering droplet near the liquid/liquid interface. In the work [78], the Marangoni flow was studied through observing the droplet of liquid (partially soluble in water) deposited into a water bath. The results reported in paper [78] show that the surface tension can cause the Marangoni instability and interfacial turbulence. Paper [78] reported the problem of the insatiability at the liquid/liquid interface, where waves and patterns were observed. The waves were observed propagating on the interface and were driven by the surface tension and gravity. The patterns were formed due to the collisions between waves. The results [78] also proves that the instabilities of the interface and the formation of capillary waves are both determined by the Marangoni number (the Marangoni number is a parameter that demonstrates the effect of convective mass transfer through the interface).

The above paragraph discuss some phenomena caused by the Marangoni flows. Next, we would like to discuss the hydrodynamic instabilities of a liquid/liquid interface. The liquid/liquid interfaces may become unstable under the action of hydrodynamic perturbations. A typical example would be a suspended film of a heavier liquid perturbed by a light liquid. The instability problem on such an interface is known as the Rayleigh-Taylor instability [79]. This instability phenomenon is the fluctuations with a typical wavelength

($\lambda^* = 2\pi\sqrt{2}k^{-1}$)[58]. Another typical type of the interfacial instability problem is the Plateau-Rayleigh instability, which occurs on the interface around a thin cylindrical object. For this problem, the thin cylinder is often used to neglect the gravity effect.

The significance of the gravity force is characterised by the Bond number (Bo):

$$Bo = k^2L^2 = \frac{\rho g L^2}{\gamma}. \tag{1.11}$$

Here, k, ρ, γ and g has already been introduced in the previous section. L is the characteristic length for the Plateau-Rayleigh instability, which is calculated by adding the radius (r) of the cylindrical object and the thickness (e) of the interface together. If the Bond number is small enough (e.g. 0.01), the gravity is negligible and the critical wavelength for the Plateau-Rayleigh instability is $\lambda^* = 2\pi\sqrt{2}r$ [58].

The above analyses are for immiscible liquids. For miscible liquids, the interface will eventually disappear due to diffusion. The effect of the diffusion on the interfacial stability is reported in paper [2]. It was found that the interfacial diffusion causes additional dissipations, slowing the development of the Rayleigh–Taylor instability, and in addition, reducing the propagation speeds of the gravity–capillary waves and increasing the damping of these waves. The mutual action of the viscous and diffusive effects was found to be capable of suppressing the growth of the short wavelength modes. If the liquids in contact are not density-matched, the gravity-driven flows are generated. The effect of gravity and vibrations on the hydrodynamic of a miscible phase boundary are reported in paper [80]. In paper [80], the Kelvin–Helmholtz instability and Rayleigh–Taylor instability were observed at the liquid/liquid boundaries. It was also shown that the rate of diffusion can be increased due to stirring mechanism caused by flows.

A miscible interface may be completely disintegrated as a result of development of these classical instabilities. The stability of a miscible interface in a vertical capillary tube was studied in papers [64, 81, 82]. In such tubes, the quasi-steady state can be held within a certain value for the gravity parameter. If the strong external shear flow existed, then the Kelvin–Helmholtz instability makes the interface unstable. The Kelvin–Helmholtz instability is observed for two density-matched liquids and is characterised by the monotonic growth of perturbations. A shear flow in a stratified layer may also cause the Holmboe-type instability that occurs through the growth of two travelling modes (the modes with non-zero phase speeds).

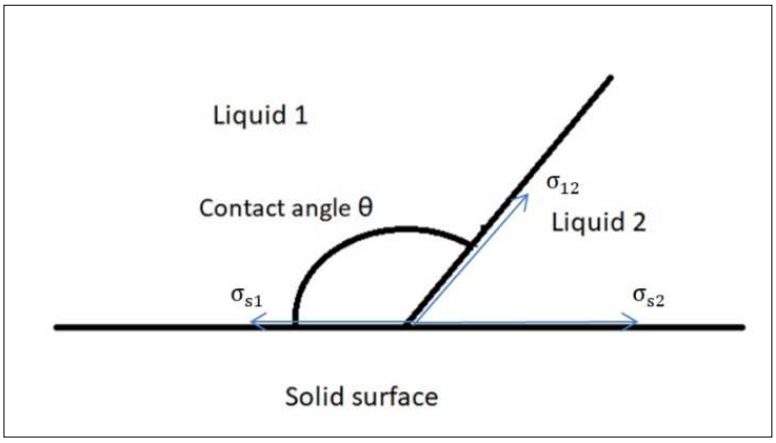

Fig. 1.10 Wetting and contact angle.

1.2.5 Wetting and contact line

The liquid/liquid interface near the solid wall is known as the contact line. The shape of the contact line (i.e. the contact angle of the liquid/liquid interface near the solid surface) is determined by the intermolecular interactions between the molecules of solid and liquids. The wettability of the liquids on a solid surface is measured by the contact angle and described by the Young's relation [58],

$$\sigma_{s1} - \sigma_{s2} = \sigma_{12} \cos\theta. \tag{1.12}$$

Here, σ_{s1} is the surface tension at the interface between the solid surface and liquid 1, similarly, σ_{s2} is the surface tension for the interface between solid surface and liquid 2, and σ_{12} is the surface tension at the interface between liquid 1 and liquid 2. θ is the contact angle of the liquid/liquid interface to the solid surface. A clear description of the Young's equation can be seen from the sketch in Fig.1.10.

From the Eq.(1.12), it is known that the wetting phenomena can be divided into three different types of wetting depending on the strength difference between two different liquids and the solid surface, which are summarised in Table.(1.2).

Table 1.2 The relationship between the wetting conditions and the intermolecular interactions between liquids and solid phases [83]

Contact angle	**Wetting properties**	**The strength of solid/liquid interactions**	**The strength of liquid/liquid interactions**
$\theta = 0^\circ$	Perfect wetting	Strong	Weak
$0^\circ < \theta < 90^\circ$	High wettability	Strong(weak)	Strong(weak)[2]
$90^\circ \leq \theta < 180^\circ$	Low wettability	Weak	Strong
$\theta = 180^\circ$	Non-wetting	Weak	Strong

The liquid film will be formed if the liquid has the perfect wettability to the solid surface. The hydrodynamics of a liquid film on a solid surface is modelled based on the governing equations that reflect the mass, momentum and energy conservation [84]. However, the problem becomes complex when the film is relatively thin. For a ultra-thin film (i.e. thickness is below 100nm), the effect of the solid surface becomes important and the thin film can be unstable due to this force (even for the case of total wetting) [58]. The force contributed from the solid surface to the liquid film is known as the long rang-force and it depends on the thickness of the interface. Thus the stability of the extreme thin film also depends on its thickness.

For miscible liquids, the contact line is a dynamic characteristic, which varies during the dissolution process and becomes constant when the equilibrium state is reached. In the experiment [2], the shape of the contact line was observed to be unchanged with the propagation of solvent phase and no visible solvent phase were observed on the tube walls after the passage of the interface. The contact angles at the upper and lower parts of the interface were different, and it was found that the contact angles changes with temperature and the ratio between the gravity and the capillary force.

1.3 The mathematical model of the fluid flows in porous media

The miscible displacement is carried out in a porous formation, and the efficiency of the displacement strongly depends on the porosity and structure of the porous media. The porous geological formation varies with species of rock (e.g. sandstone, limestone, crystalline, clay, etc) and also with the type of rock interstices (well sorted or poorly sorted sediments). In reality, the problem is more complicated when the sediments or rocks were subjected to some mechanical fracturing or chemical erosion and so new fissures were generated [85–87].

We have mentioned that the concept of macroscopic and microscopic displacement efficiencies have been introduced to characterise each EOR process. There are also macroscopic and microscopic models to evaluate displacement in porous media (In Fig.1.11). At the macroscopic scale, the displacement is evaluated by the Darcy's law. The Darcy's law is derived from the Navier-Stokes equation under the condition that the fluid is incompressible and the flow motion is creeping. The complexity of porous media is simplified by introducing the permeability or porosity to describe the hydraulic conductivity of porous media. These two phenomenological parameters are determined experimentally.

[2]It means the interactions are both strong or both weak.

To describe the evaluation of a multi-phase system of immiscible liquids, the extended Darcy law is developed and this extension brings new phenomenological parameters [88]. These are the capillary pressure and the relative permeability of each phase that are depending on the mass fraction of one component in the mixture and these dependencies are also experimentally measured. In fact, this theory is based on infinite numbers of phenomenological parameters because each parameter normally has the independent relations with other parameter that are generally determined by infinite points [89, 90]. This makes this approach very specific to one particular porous media, one particular mixture, and even the particular process. In addition, the extended Darcy model does not capture the dynamic changes of the relative permeability and capillary pressure that should happen upon mixing of the miscible liquids. Despite these disadvantages, a macro-model is needed for the evaluation at the industrial scale. If the injecting liquid is miscible liquids, an equation for the conservation of the chemical species needs to be added [91]. The macroscopic description of the fluids transportation in porous can be formulated as,

$$\nabla \cdot \vec{v_d} = 0, \tag{1.13}$$

$$\vec{v_d} = -\frac{k}{\phi \mu} \nabla P, \tag{1.14}$$

$$\frac{\partial C}{\partial t} + \vec{v_d} \cdot \nabla C = D_{eff} \nabla^2 C. \tag{1.15}$$

Here, $\vec{v_d}$ is the Darcy velocity of fluid, D_{eff} is the effective diffusion coefficient, k is permeability of the porous media, ϕ is the porosity, and μ is the viscosity of the fluid. It should be notice the fluid velocity calculated here is the averaged velocity of fluid ($\vec{v_d}$) in porous media. The result of the diffusion flux is also an approximated value that ignores the microscopic behaviours at the pore space.

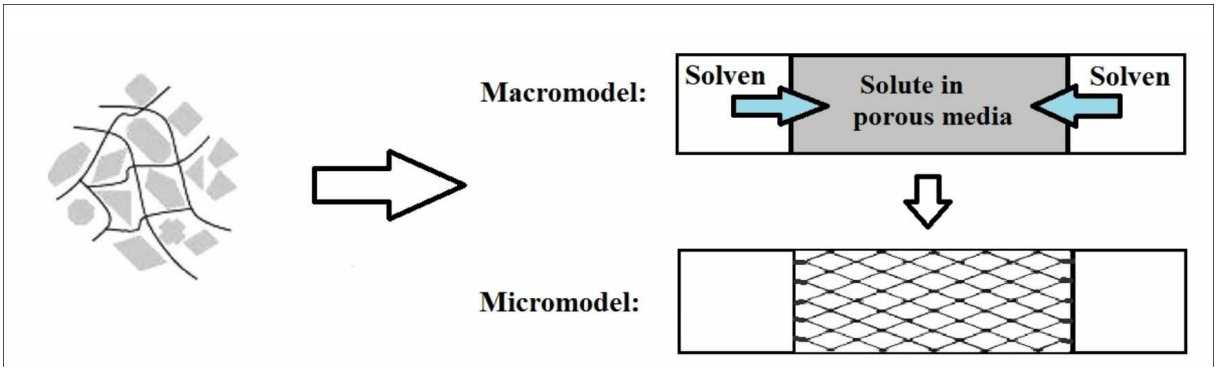

Fig. 1.11 Macromodels and micromodels.

At the microscopic scale, properties at the interface separating different phases become important. Instead of using Darcy's law, the fluid motion at the pore level is determined from the Navier-Stokes equations. The interfacial tension, together with the liquid/rock interactions (wettability), defines the capillary pressure and consequently the viscous forces.

One popular microscopic model is the network approach. It uses a bundle of capillary tubes to represent the pores and pore throats in a porous media. The development of the network model can be dated back to the bundle-of-tubes model (In Fig.1.12(a)) developed by Washburn [92]. The simplicity is the biggest advantage of this model, though the model does not include the cross-connected pores. Such disadvantage was solved by Fatt [93] who developed the network model with cylindrical tubes. The basic network model can be a square network (In Fig.1.12(b))), and it can be extended to the single hexagonal network, double hexagonal or even triple hexagonal network to represent more complex cross-connectivity among pores. These different distributions among void spaces and pores are characterised by the number of flow paths joined into one tube [93]. The effect of cross-connectivity among pores can be better represented when the relation between void spaces and pores are represented by the packing of sphere balls (Fig.1.12(c)), but this would make the dynamical analysis more difficult [93–95].

The porous media in most applications consists of very complex and unexpected structures. As a consequence, network models can be also modified to have complex structures such as unstructured irregular networks [96] and even random void space size (Fig.1.12) to capture various phenomena [97]. However, such complex network models may not be universal because they are built for the particular case.

The network geometry eventually refers to the shapes and sizes of pore bodies and pore throats, which can affect the physical process between pore throat, e.g. snap-off, trapping, wetting, etc. There are various kinds of network geometries and some details about consideration of different options has been viewed by Joekar-Niasar and Hassanizadeh [98]. As a consequence, to comprehend the dynamics of the flows in porous media, the fluid behaviour in a single capillary (Simplest network) needs to be understood first.

Other microscopic models are: Lattice-Boltzmann (LB) model, smoothed particle hydrodynamics approach, level-set models, percolation models [98]. Joekar-Niasar and Hassanizadeh [98] made a comparison of above microscopic models, and they stated that the pore-network model has numerous advantages such as the capability to provide more information about the physics of the phase transition, and also can be applied inexpensively [98]. Due to above reasons, in numerous cases, the pore-network model has been used to mimic the porous media. In our work, we want to use this approach to study the dissolution process in a porous media.

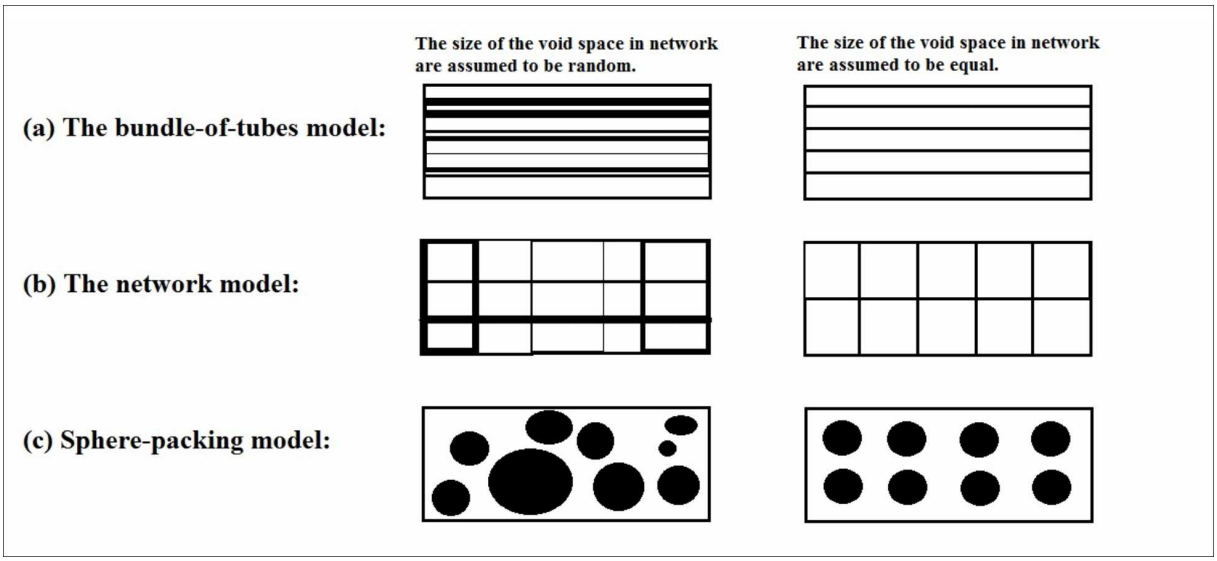

Fig. 1.12 Network models.

The mathematical model of EAR process is developed independently from the EOR process because of the particular modeling difficulties, such as, uncertain boundaries, insufficient data about flow motion, uncertain chemical or bio-chemical reactions, etc [26]. EAR processes are normally modelled by a continuum model with its domain divided by various representative elementary volumes (REV). Depending on the size of REV, it can be classified: molecular scale, microscopic scale, macroscopic scale, and megascopic scale [26]. Important quantities, such as, heterogeneity, mass, velocity, are calculated by using the averaging value in a REV unit [26].

1.4 Kinetic model of lipid extraction

The mathematical model of lipid extraction is also different from above models because lipid extraction is normally considered as a biochemical process or a thermochemical process where the cell disruption and the total lipid (oil) extraction are important [99]. The oil content (or lipid content) in different algae species varies from approximately 10% to 50% [100] and the performance of the lipid extraction is evaluated by the percentage of the lipid that has been yield. The percentage of the lipid yield is mathematically defined as [43, 101, 102]:

$$C = \frac{m_e}{m_0}. \tag{1.16}$$

Here, m_e represents the mass of the extracted lipid and m_0 is the amount of extractable

lipid in algae. It should be noticed that the definition of the quantity "lipid yield" is different from the percentage of oil in the soil/solvent mixture. The paper [102] studied the method of the supercritical CO_2 extraction and they formulated the kinetic model with the extractable lipid and un-extracted lipid,

$$\frac{\partial m_e}{\partial t} = k\left(m_0 - m_e\right). \tag{1.17}$$

Here, t is the extracting time, and k is the rate constant. Although the variable is defined differently, Eqs.(1.19) and (1.17) are similar and the relationship between extracted lipid and extraction time can be obtained similarly.

From the review of the lipid extraction in previous section, it is known that this is not simple mass transferring process because of the cell disruption. Hence the definition of the quantity "lipid yield" hides some essential facts e.g. the lipid translocation in membranes. The model of lipid extraction cannot be represented by a kinetic mode of mass transfer but rather an extraction–transesterification reaction . Paper [101] gives the expression of this transesterification reaction,

$$Triglycerides + 3CH_3OH \leftrightarrow Methylesters + glycerol. \tag{1.18}$$

In paper [101], the transesterification is assumed to be the only sourse of the extracted lipid is assumed and the kinetic model was reformulated by using the amount of methyl esters (biodiesel) formed during the transesterification. The rate of the lipid extraction process is evaluated in a way that is similar to the one used for chemical reactions:

$$\frac{\partial C}{\partial t} = kC^n. \tag{1.19}$$

Here, C is amount of methyl esters produced during the reaction, t is the extraction time, k is the rate constant, and n is the order of the reaction. In the case of the lipid extraction in Algae, n is assumed to follow the first-order law and this has been experimentally verified in papers [43, 101, 102].

The kinetic equation of the lipid extraction (Eq.(1.19)) is a first-order linear ordinary differential equation and its general solution is $C = C_0 e^{kt}$ (C_0 is the initial value of the amount of the methyl esters). With the initial condition, the equation can be solved and gives the relationship between the concentration and extraction time:

$$k = \frac{\ln C_t - \ln C_0}{t}. \tag{1.20}$$

Here, C_t and C_0 represent the concentration of methyl esters at time t and at time $t = 0$, respectively. From Eq.(1.20), it can be seen that the natural logarithm of the lipid yield has

a linear relationship with the extraction time and the slope of the this line is k. This means the experimental data can be arranged to fit the plot of $\frac{\ln C_t - \ln C_0}{t}$.

The rate coefficient k is an important parameter to evaluate the rate of the lipid extraction because it is the slope between $\ln m_t - \ln m_0$ and t. This parameter is calculated through Arrhenius equation [43, 101],

$$k = Ae^{-\frac{E_a}{RT}}. \tag{1.21}$$

Here, A is the frequency factor of the reaction, R is the universal gas constant, T is the absolute temperature, and E_a is the activation energy. Frequently, this equation is written in an alternative form that shows the linear relationship between the natural logarithm of k and temperature T ($\frac{1}{T}$):

$$\ln k = -\frac{E_a}{RT} + \ln A. \tag{1.22}$$

Here, $\frac{E_a}{R}$ is the slope of the straight line of $\ln k$ versus $\frac{1}{T}$. R is a constant and the slope of this straight line can be reduced to the activation energy E_a. For different species of algae, the activation energy is different. For example, the activation energy for algae strain B. braunii AP102 is about $36\frac{kJ}{mol}$ [43], but for Spirulina platensis algae, $E_a = 14.518\frac{kJ}{mol}$.

The parameter A in Eq.(1.21) is a thermodynamic activation parameter between solvent and solute. The expression for parameter A will require knowing other parameters, such as, the activation entropy ΔS, the Gibbs free energy of activation ΔG, and activation enthalpy ΔH. The equations will finally be written as:

$$A = \frac{RT}{Nh} e^{\frac{\Delta S}{R}}, \tag{1.23}$$

$$\Delta G = \Delta H - \Delta S, \tag{1.24}$$

$$\Delta H = E_a - RT. \tag{1.25}$$

Here, the activation entropy ΔS, the free energy of activation ΔG, and activation enthalpy ΔH determine the spontaneity of the extraction process. The above quantities, namely, the Gibbs free energy ΔG, the enthalpy change ΔH and the entropy change ΔS are related to k through the following expression [43],

$$\ln k = -\frac{\Delta G}{RT} = -\frac{\Delta H}{RT} + \frac{\Delta S}{R}. \tag{1.26}$$

The value of ΔG determines whether the extraction process can occur spontaneously (if ΔG

is negative) [43, 101]. And, in contrast to this, the positive values of the ΔG means the process is unspontaneous. The value of ΔS determines the whether the extraction process is irreversible [43, 101]. For the irreversible process, ΔS is positive. In the work [101], the lipid from the Spirulina platensis algae was extracted under 328K(55°). ΔG was obtained as $92.71\frac{JK}{mol}$ and ΔS is obtained as $-232.83\frac{JK}{mol}$. In another work [43] where the algae strain B. braunii AP102 is studied under different temperature ranged from 308K to 338K, ΔG was obtained as $-0.1612\frac{kJ}{mol}$ and ΔS is obtained as $0.5246\frac{J\cdot K}{mol}$ at the 308K. At their highest temperature 338K, ΔG was obtained as $-4.811\frac{kJ}{mol}$ and ΔS is obtained as $1.712\frac{JK}{mol}$.

From the above description of th is model, it can be seen that a description of the diffusion processes is lacking. The kinetic model used in paper [43, 101, 102] only description a bio-chemical reaction and the spatial variations of the concentration are not considered. The percentage of the lipid yield describes only the average lipid content in algae (algae should have a more complex composition, but only the lipid content is characterised). Nevertheless, the extraction of lipids should also involve the diffusive exchange of molecules between the solvent-phase and the lipid-phase.

1.5 The mathematical model of the convective and diffusive evolution of the miscible liquids

In the last section, we viewed the mathematical models of the process of mass transport in the applications we viewed at the beginning of this chapter. The kinetic model of lipid extraction treats the process as a bio-chemical reaction. The Darcy's model describes the fluids motion in porous media but it ignores the microscopic behaviours, which is important for the understandings of diffusion in liquid/liquid mixture. Hence the network approach (diffusion in a network of capillaries) is needed. The most basic network model is a single capillary tube where the diffusion of two miscible liquids have been experimentally studied in paper [2]. We want to build up a computational model that is capable of reproducing this experiment [2]. In this section, we would like to viewed the mathematical model of two fluids system.

1.5.1 Molecular dynamics simulation

There are macroscopic and microscopic descriptions of the two fluids system. The microscopic description is given by the molecular dynamics simulation. This method is built based on the motion of the molecules. Within this method, the motion of a molecular is

described by the Newton's equation of motion,

$$m\frac{d^2\vec{x}}{dt^2} = \vec{f}. \tag{1.27}$$

Here, m is the mass of a molecule, $\vec{x}$ is the position of a molecule, t is the time, $\vec{f}$ is the intermolecular force applied to a molecule, which is calculated by:

$$\vec{f} = -\frac{\partial U}{\partial \vec{x}}. \tag{1.28}$$

Here, U is the Lennard-Jones potential, which can be expressed as [103],

$$U = \frac{1}{2}\sum \phi(r), \quad \phi(r) = 4\varepsilon\left[\left(\frac{\sigma}{r}\right)^{12} - \left(\frac{\sigma}{r}\right)^{6}\right]. \tag{1.29}$$

Here, ϕ is a function of intermolecular distance, r is the intermolecular distance, ε is the energy coefficient, σ is the length parameter (the distance between the molecules when their intermolecular potential equals to zero). $\sum$ means the summation of all molecules.

In another popular method, i.e. the Monte-Carlo simulation, the intermolecular force is evaluated by a probabilistic approach of the binary collisions instead of solving Equation (1.28) and (1.29).

1.5.2 The macroscopic description of the convective and diffusive evolution of the two liquids system

Computational model for the bulk phase

For the macroscopic description, the continuous fields of physical variables of the velocity $\vec{v}$, density ρ (or the concentration C), and pressure P are used. The equation of mass balance reads as:

$$\frac{\partial \rho}{\partial t} + \nabla \cdot (\rho \vec{v}) = 0, \tag{1.30}$$

and the equation of momentum balance reads as:

$$\frac{\partial (\rho \vec{v})}{\partial t} + \nabla \cdot (\rho \vec{v} \otimes \vec{v}) = -\nabla P + \nabla \varsigma. \tag{1.31}$$

Here, ς is viscous stress. If the problem is non-isothermal, the equations of energy balance and entropy balance are also needed.

The above equations are written taking into account of the compressibility of fluids. If

fluids are incompressible, the governing equations changes to be:

$$\nabla \cdot \vec{v} = 0, \tag{1.32}$$

$$\rho_0 \frac{d\vec{v}}{dt} = -\nabla P + \nabla \varsigma. \tag{1.33}$$

Computational model for the interface

The above equations are applicable for the bulk phases. At the interface between two liquids, the above equations are coupled with the equations for the interfacial phenomena. In general, it can be done by imposing the boundary conditions at the interface. Such boundary conditions are made to describe the balance of the quantities (namely, ρ (C), $\vec{v}$, P and T) between two bulk phases. A set of these interfacial balance equations can be written as:

$$\rho_1 (\vec{v}_1 - \vec{v}) \cdot \vec{n}_n = \rho_2 (\vec{v}_2 - \vec{v}) \cdot \vec{n}_n = \frac{dm}{dt}, \tag{1.34}$$

$$-\vec{n}_n (P_2 - P_1) + \vec{n}_n \cdot (\varsigma_2 - \varsigma_1) = \frac{dm}{dt} (\vec{v}_2 - \vec{v}_1) + \sigma \left(\frac{1}{R_1} + \frac{1}{R_2} \right) \vec{n}_n + \frac{\partial \sigma}{\partial x}, \tag{1.35}$$

Here, the notations 1 and 2 represent the liquid 1 and the liquid 2, $\vec{n}_n$ is the unit vector normal to the interface, R_1 and R_2 are the radius of curvature of the interfaces. The gradient $\frac{\partial \sigma}{\partial x}$ the tangential force of the surface tension.

If the variation of the surface tension coefficient, the viscosity, and all the velocity terms can be neglected, the boundary condition can be reduced to the Laplace expression,

$$\Delta P = \sigma \left(\frac{1}{R_1} + \frac{1}{R_2} \right). \tag{1.36}$$

Here, ΔP is the pressure difference across the interface, σ is the surface tension.

This model defines the interface as a surface of discontinuity (a sharp interface, in Fig.1.13), assuming that the typical length scale of the interface is much smaller than the typical length scale of the phenomena occurring in the bulk phase. This is true for most applications [104]. However, in reality, the interface is a layer of molecules and the description of the sharp interface (in Fig.1.13) is just an assumption for the macroscopic theory. The miscible liquid/liquid interface near the critical point cannot be modelled as a surface of discontinuity because of the phase transition. When a liquid/liquid mixture approaches the critical point from a point slightly below the critical point, the interface becomes very diffusive and the variation of the diffusive interface becomes comparable with the bulk phases.

For such case, the diffusive interface model (in Fig.1.13) is needed.

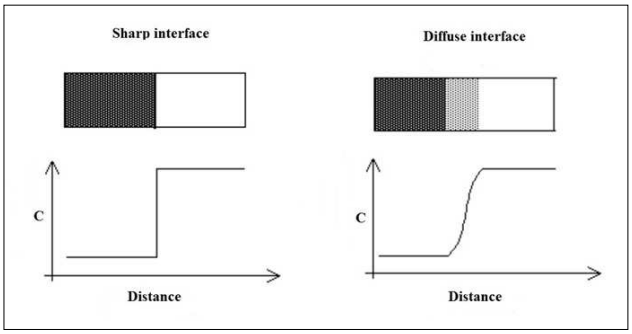

Fig. 1.13 The sharp interface model and the diffusive interface model [105].

Some popular approaches to trace the evaluation of an interface, e.g. the volume of fluid (VOF) method and the level set method [106–108], describe the interface by a characteristic function, which can be shown by the following expression:

$$C = \begin{cases} C_1, & liquid1; \\ C(C_1,C_2), & interface; \\ C_2, & liquid2. \end{cases}$$

Here, C_1 and C_2 are the concentration of the liquid 1 and the liquid 2. $C(C_1,C_2)$ is the characteristic function for the interface. The function $C(C_1,C_2)$ is expressed to describe the transition in the concentration field between two phases. It can be defined as a constant if the liquids are immiscible. When the liquids are miscible or there is a phase change (evaporation or condensation) between two liquids, the characteristic function is modified to include the effect of the surface tension and species transport [104]. However, the interface is still described by the sharp interface model because the concentration profile is defined to be discontinuous at the liquid/liquid boundaries. Besides, the problem exists when two interface moves and meet (one of the interfaces will disappear).

The diffusive interface model is build on the basis of the thermodynamic description. Such description defines a variable to represent different phases during a process of the phase transformation. This variable is called the order parameter of the phase transition [105]. The function of thermodynamic potential is expressed as a function of the order parameter, pressure and temperature. Pressure and temperature are used to define the state of a system and they enter into the equation as constant. For a set of given pressure and temperature, the thermal equilibrium is obtained by the minimum point of the thermodynamic potential function.

This approach is called the phase-field approach. The advantage of this approach is that

the model is based on the physics-based description of the system. According to the review [109], this model was developed to introduce the diffuse interface in multi-phase systems. The first diffuse interface model is proposed by Van der Waals [110]. Then, Korteweg [57] suggested that the surface tension should be modelled through the concentration gradients. Cahn and Hilliard [111, 112] developed the phase-field theory for binary mixtures. The full set of equations for the thermal- and hydrodynamic evolution of liquid/liquid binary mixtures was derived by Lowengrub and Truskinovskii [113].

1.6 Phase-field approach

In this section, we will introduce more details about the phase-field approach. The phase-field approach has been extensively used as a numerical tool for microstructure evolution of phase transition [105, 114–116]. There are two types of phase transition. One is called the phase transition of the first kind, and another is called the phase transition of the second kind. Depending on the type of the phase-transition, the variable for tracking phases in the phase-field method needs to be selected differently [117]. According to book [56], the phase transition of the first kind refers to the phase transition that occurs in a continuous manner. During the phase transition, different phases only changed in the intensity of molecular interaction. The typical examples are gases and liquids. The variable that defines the degree of phase transition can be density or concentration [56, 118]. The phase transition of the second kind refers the phase transition that cannot occur in a continuous manner. The changes of substances in different phases are qualitative changes instead of quantitative changes. In one word, the old substance is replaced by the new substance as a whole. The typical example is crystal. The substance changes between the ordering state and disordering state. A new variable, the degree of ordering (order parameter), is introduced to characterise the degree of phase transition.

Diffusion in liquid/liquid mixture belongs to the phase transition of the first kind and we use the concentration as the phase-field variable. The free energy of a system is expressed as a function of the phase-field variables, and then the dynamics of phase transition is evaluated on the basis of the kinetic equation.

Cahn and Hilliard [111, 112] developed a phase-field mode for general two phases system, which is primarily used by them to model the interfaces during phase transitions in solids [105, 114]. The free energy function in the Cahn-Hilliard model [111, 112] reads as,

$$f(C) = f_0(C) + \frac{\varepsilon}{2}\nabla^2 C. \tag{1.37}$$

Here, ε is capillary coefficient depends on the inter-molecular potentials. f_0 is the classical part of free energy, Landau and Ginzburg [56] gave an expression of the free energy function when describe the problem of the superfluidity and superconductivity,

$$f_0(P,T,C) = A(P,T)C^2 + B(P,T)C^4. \tag{1.38}$$

They [56] assumed that P is a constant and T is near the critical point T_c the coefficients, and the expression of the coefficient A and B can be written as,

$$A(T) = k(T - T_c), \tag{1.39}$$

$$B(T) = B(T_c) = constant. \tag{1.40}$$

There are two kinds of the kinetic equations for different phase transitions. One is called the Landau-Ginzburg equation and another one is the Cahn-Hilliard equation [119].

The Landau-Ginzburg equation defines that the time change of the order parameter is proportional to the chemical potential [56]:

$$\frac{\partial C}{\partial t} = -\Gamma \frac{\partial f}{\partial C}. \tag{1.41}$$

Here, C is the order parameter, Γ is a positive coefficient and the chemical potential is given by the derivation of the free energy $\frac{\partial f}{\partial C}$. The Landau theory was originally developed to describe superconductivity [56].

Another kinetic equation was derived by Cahn and Hilliard [111, 112]. In the Cahn-Hilliard equation, the phase-transition is driven by the gradient of the chemical potential, which can be expressed as:

$$\frac{\partial C}{\partial t} = \Gamma \nabla^2 \frac{\partial f}{\partial C}. \tag{1.42}$$

Here, similar with Eq.(1.41), C is the order parameter, and the chemical potential is expressed by $\frac{\partial f}{\partial C}$.

Although Eq.(1.41) and Eq.(1.42) are different, Refs.[119–121] show that these two equations can be obtained from the same Markovian master equation. The procedure of the derivation was reported in paper [120]. It was shown that Eq.(1.41) is derived under the assumption that there are no constraints for the variation of order parameter at its location. While Eq.(1.42) is obtained with condition that the variation of order parameter is constrained. The application of Eq.(1.42) can be to the binary liquid mixtures and binary alloys [120, 121]. The Landau-Ginzburg equation is applicable to the problems of condensation in

gases and bio-polymers [120, 121].

We want to use this approach to provide the accurate thermal- and hydrodynamic evaluation of multi-phase binary mixture, taking into account the effect of barodiffusion [122] and the surface tension effects existent at miscible boundaries. For a liquid/liquid mixture, it can be written as,

$$\nabla \cdot \vec{v} = 0, \tag{1.43}$$

$$\rho_0 \frac{\partial \vec{v}}{\partial t} + \rho_0 \vec{v} \cdot \nabla \vec{v} = -\nabla P - \nabla \cdot (\varepsilon \nabla C \otimes \nabla C) + \nabla \cdot \varsigma, \tag{1.44}$$

$$\frac{\partial C}{\partial t} + \vec{v} \cdot \nabla C = \nabla \cdot \nabla \mu, \tag{1.45}$$

$$\mu = \mu_0 - \varepsilon \nabla C. \tag{1.46}$$

The above equations are not feasible for the liquid/liquid mixture with strong density difference because the vector field of velocity cannot be assumed to be solenoidal $\nabla \cdot \vec{v} \neq 0$. Lowengrub and Truskinovskii [113] derived out the Cahn-Hilliard-Navier-Stokes equations with quasi-compressibility effects. The governing equations read as,

$$\frac{\partial \rho}{\partial t} + \nabla \cdot (\rho \vec{v}) = 0, \tag{1.47}$$

$$\rho \left(\frac{\partial \vec{v}}{\partial t} + \vec{v} \cdot \nabla \vec{v} \right) = -\nabla P - \nabla \cdot (\varepsilon_l \rho \nabla C \otimes \nabla C) + \nabla \cdot \varsigma, \tag{1.48}$$

$$\rho \left(\frac{\partial C}{\partial t} + \vec{v} \cdot \nabla C \right) = \nabla \cdot \nabla \mu, \tag{1.49}$$

$$\mu = \mu_0 - \frac{P}{\rho^2} \frac{d\rho}{dC} - \varepsilon_l \nabla \cdot (\nabla C). \tag{1.50}$$

Here, ε_l is defined as $\frac{\varepsilon}{\rho}$. Lowengrub and Truskinovsky's model is still hardly feasible for the numerical treatment due to the necessity to use the full continuity equation because of the concentration dependence of the mixture density. To filtered out the quasi-compressible effects, the Boussinesq approximation of the full equations was obtained by Vorobev [122]. The details of Vorobev's model will be discussed in the following because it is the model used in this work.

Chapter 2

Mathematical model

In last chapter, we introduced several mathematical models that were frequently used to describe the kinetics of diffusion. It is known that the understanding of diffusion should be built up based on the non-equilibrium thermodynamics, which can be the classical Fick's law or the Cahn-Hilliard model. The Fick's is the classical approach to describe diffusion, but the Cahn-Hilliard model provides a better description of the process of the dissolution if compared with the description given by the classical Fick's law due to the fact that different phases are explicitly distinguished in this approach. The Cahn-Hilliard model was not developed for diffusion in a liquid/liquid mixture. But the feasible model (Cahn-Hilliard-Navier-Stokes equations) has already been developed by Vorobev [122] and this model will be used in this work to explain the kinetics of diffusion of two miscible liquids reported in paper [62].

This chapter will introduce the mathematical model of the dissolution process. Firstly, we started with the usage of the classical Fick's law, and even supplementing this approach with some additional properties of the liquid/liquid boundaries. After that, the phase-field model based on the Cahn-Hilliard theory is introduced. Within this approach, the effect of the surface tension and the barodiffusion can be directly added. Furthermore, the coupling model between the equation of species transports model and the Navier-Stokes equation is built up, in which, the hydrodynamics is added to assess the influences of flows on the overall mass transfer.

2.1 Fick's law

We firstly examined the classical Fick's law with its diffusion coefficient strongly depends on concentration. Paper [62] gives an expression of the mutual diffusion coefficient in glycerol/water mixture at $20^{\circ}C$, which is $D = 1.6 \cdot 10^{-10}(1 - 8.95 \cdot 10^{-1}C)m^2 \cdot s^{-1}$. This

expression will be used in our work. Since the diffusion coefficient strongly depends on the concentration, the Fick's second law can be written as:

$$\frac{dC}{dt} = \nabla \left(D\left(C\right) \nabla C \right). \tag{2.1}$$

To conduct the numerical simulation, the non-dimensional scales need to be introduced. The length scale is denoted by L_*. In this work, we define the length of the capillary tube as the unit length scale $L = 1$. Since diffusion is described by the classical Fick's law, the time scale is defined by $\tau_* = \frac{L_*^2}{D_0}$, where D_0 is the typical value of the diffusion coefficient, e.g. the diffusion coefficient in water.

2.1.1 Fickian diffusion with hydrodynamics

To make an accurate evaluation of the dissolution, the effect of the hydrodynamics on the mass transfer is taken into consideration. The flow is driven by the gravity and by the dependence of the mixture density on concentration. The density of the liquid/liquid mixture can be approximately defined by:

$$\rho = \rho_1(1+\phi C), \quad \phi \equiv \frac{\rho_2 - \rho_1}{\rho_1}. \tag{2.2}$$

Here, ρ_1 and ρ_2 are the densities of the pure mixture components and ϕ is the density contrast between two liquids.

Taken into account of the condition of the incompressible fluids, the governing equations (reflect the conservation of mass, momentum and species) can be written as:

$$\nabla \cdot \vec{v} = 0, \tag{2.3}$$

$$\frac{\partial \vec{v}}{\partial t} + (\vec{v}\cdot\nabla)\vec{v} = -\nabla p + \frac{1}{Re}\nabla^2\vec{v} + GrC\vec{\gamma}, \tag{2.4}$$

$$\frac{\partial C}{\partial t} + (\vec{v}\cdot\nabla)C = \nabla \cdot \left(D(C)\nabla C \right). \tag{2.5}$$

Here, $\vec{\gamma}$ is the unit vector directed upwards. For numerical analysis, the governing equations need to be non-dimensionalised. The length scale L_* and the time scale $\tau_* = \frac{L_*^2}{D_0}$ are same with the last section. The model requires new non-dimensional scales for velocity and pressure, which are $v_* = \frac{L_*}{\tau}_*$ and $p_* = \rho_1(\frac{L_*}{\tau_*})^2$. Eq.(2.5) contains some non-dimensional parameters, whose definitions are as follow: the Reynolds number,

$$Re = \frac{\rho_1 L_*^2}{\eta_* \tau_*} = \frac{\rho_1 D_0}{\eta_*}; \tag{2.6}$$

and the Grashoff number,

$$Gr = \phi \frac{g\tau_*^2}{L_*} = \phi \frac{gL_*^3}{D_0^2}. \tag{2.7}$$

Here, η_* is the typical value of the viscosity coefficient and g is the gravity acceleration.

The above model can be improved by adding an additional term describes the surface tension effects. The effect of the surface tension is known to affect the shape of solvent/solute boundary and generate the concentration-driven flows along the interface (the Marangoni effect). This force is known as the Korteweg force. The Korteweg force is the force that appears in the phase-field approach after adoption of the additional term in the free energy. This term defines the additional interfacial stresses induced by the concentration gradients, which represents the fact that the non-uniformity of the surface tension is caused by variations of the field of concentration [57].

We use the formulation of the Korteweg term derived from the phase-field model for a two liquids systems [122]. The amplitude of the force is defined by the capillary constant, and thus this term is negligible everywhere expect for the interfaces. The governing equations with the addition of the Korteweg force can be written as,

$$\nabla \cdot \vec{v} = 0, \tag{2.8}$$

$$\frac{\partial \vec{v}}{\partial t} + (\vec{v} \cdot \nabla)\vec{v} = -\nabla p + \frac{1}{Re}\nabla^2 \vec{v} - Ca\nabla^2 C \nabla C + GrC\vec{\gamma}, \tag{2.9}$$

$$\frac{\partial C}{\partial t} + (\vec{v} \cdot \nabla)C = \nabla \cdot (D(C)\nabla C). \tag{2.10}$$

Here, Ca is capillary number, which is defined as $\frac{\varepsilon_*}{(v_* L_*)^2}$ (ε_* is the typical value of the capillary constant).

2.1.2 Non-Fickian diffusion

Diffusion in the liquid/liquid mixture was reported to exhibit a non-Fickian behaviour [2]. In chapter 1, it was mentioned that the miscible displacement experiment has also been extended to the diffusion between the polymer and its monomer [71]. For such a mixture, the effect of polymerization is a new factor that affects diffusion. In paper [71], it was found that the polymerization affects the concentration and hence the viscosity in two liquids. In other experiments [123, 124] where polymerization is the dominating reaction, the polymerization front was observed at the interface and moves toward to unreacted polymers.

Miller-Chou and Koening [125] summaries the dissolution behaviours between solvent and polymer and discuss the possible factors that affect the dissolution. They mentioned

that the dissolution behaviours in polymer system are quite diverse. In general, when the solvent gets into contact with a glass polymer, a gel layer is formed between two phases, and two interfaces (the solvent/gel and gel/polymers boundaries) can be observed among the solvent, the gel layer and the polymer. The stricter of such surface layer can be even classified to be: the pure polymer, the infiltration layer, the solid swollen layers, the gel layer, the liquid layer, the pure solvent layer [124, 125]. The work [125] also mentions there are some cases when the gel layer is not formed. In such case, instead of forming a gel layer, the polymer cracks when it is in contact with the solvent [125]. The mathematical models of diffusion in the solvent/polymer system are reported in Refs.[126–130].

A polymer is a long-chain molecule that is composed of a series of small molecules (monomers) via various polymerization methods, e.g. condensation, free radical, ionic, emulsion, and co-polymer (with different monomers) [131]. The most special property of polymer material is viscoelasticity, which is the reason for the complex non-Newtonian rheology. The viscoelastcity of polymers strongly depends on the molecular weight of the polymer molecules, that is discussed in particular in the work [131]. It is generally known that such behaviour is stronger when the molecular weight is greater. In the most experiments that study the effect of diffusion in polymers, the light molecular weight polymers are frequently used due to the fact that the high molecular weight polymers usually have a relatively low diffusion coefficients [1].

The solubility of a solvent/polymer system or polymer/polymer system is described by an energy-based theory provided by Flory and Huggins [131]. In their theory, the free energy of mixing is expressed as:

$$f_{mix} = kTN\left(\frac{\phi_1}{r_1}\ln\phi_1 + \frac{\phi_2}{r_2}\ln\phi_2 + \phi_1\phi_2\chi\right). \tag{2.11}$$

Here, f_{mix} is the free energy of mixing, k is the Boltzmann constant, T is the temperature, N is the number density of molecules, ϕ_1 and ϕ_2 are the volume fractions of solvent and polymer, r is the chain length of solvent and polymer, and χ is the interaction parameter between solvent and polymer. In this equation, $\ln\phi_1$ and $\ln\phi_2$ imply that the first two terms are negative in all conditions. The terms $\frac{1}{r_1}$ and $\frac{1}{r_2}$ also show that the significance of the first two terms tend to be small when the chain length is higher. Thus the solubility is primarily determined by χ. The effects of above-mentioned factors (such as molecular weight, chain length, solubility, etc.) are summarised in the work [125].

In the model of diffusion for a solvent/polymer system, diffusion is described by the classical Fick's law and the Non-Fickian features are explained by the swelling behaviour (structural changes) caused by the penetrant [132]. The polymers have two different states,

which are the rubbery state and glass state. The variation of the polymer's states depends on the temperature and concentration of the penetrant. Once the value of the glass transition concentration or temperature is reached, the phase transformation between the rubbery state and the glass state occurs [132]. In general, diffusion was reported to obey the classical Fick's law when the polymers are at rubbery state (the so-called case 1 diffusion). When a phase transformation from rubbery state to glass state occurs, the process becomes non-Fickian diffusion or anomalous diffusion (this is also known as the case 2 diffusion or the super case 2 diffusion). The rate of mass transfer of the case 2 and the super case 2 diffusion were also reported to be time dependent, but with different time-dependencies. For the case 2 diffusion, the time-dependence was reported to be between $\frac{1}{2}$ and 1 [128]. For the super case 2, the time-dependence was above 1 [128]. In the papers [128–130], the mathematical model of the diffusion in the solvent/polymer system were developed.

The kinetic equation for diffusion in polymer system is based on the Fick's law, however, with addition of the viscoelastic effects. In paper [133], one expression is written as:

$$\frac{\partial C}{\partial t} = \nabla \left(D\left(C\right) \nabla C \right) + \nabla \left(E\left(C\right) \nabla \sigma \right). \tag{2.12}$$

Here, $D_v\left(C\right)$ is the viscoelastic diffusion coefficient. In paper [133], $D\left(C\right)$ is defined as an exponential function of concentration and $E\left(C\right)$ is defined to be proportion to concentration. The stress σ is evaluated through a complex function of both the polymer-penetrating concentration and the Young modulus of a polymer.

Here, $D(C)$ is the diffusion coefficient and $E(C)$ is the viscoelastic coefficient. Both coefficients depend on concentration. The stress σ is traditionally described by the Maxwell model,

$$\frac{\partial \sigma}{\partial t} + \frac{\beta}{\eta}\sigma = \frac{\partial \varepsilon}{\partial t}, \tag{2.13}$$

or the Vogit model,

$$\frac{\partial \sigma}{\partial t} = \eta \frac{\partial \varepsilon}{\partial t} + \beta \varepsilon. \tag{2.14}$$

Here, β is a coefficient related to the relaxation time, η is the viscosity, ε is the strain.

In paper [128], a new expression was written through the inclusion of both the Maxwell model and the Vogit model,

$$\eta \frac{\partial \sigma}{\partial t} + \left(\beta_1 + \beta_2\right) \sigma = \beta_2 \left(\eta \frac{\partial \varepsilon}{\partial t} + \beta_1 \varepsilon \right), \tag{2.15}$$

Eq.(2.15) are not sufficient for the computational modelling because it contains three unknown variables, namely, concentration C, stress σ and strain ε. A relationship between

these three variables needs to be found to eliminate the number of unknowns. In paper [128], it assumes that the variation in strain ε is proportional to the concentration and Eq.(2.15) is replaced by the following expression,

$$\frac{\partial \sigma}{\partial t} + \beta \sigma = f(C, C_t) = \rho C. \tag{2.16}$$

The polymers may be transformed to be two separate regions (glass and rubbery) or three regions (glassy, transition, and rubbery) and the relaxation time is different in the different region. To describe this behaviour, the parameter β was evaluated through the following expression,

$$\beta = \beta(C) = \frac{\beta_G + \beta_R}{2} + \frac{\beta_R - \beta_G}{2} \tanh\left(\frac{C - C_*}{\delta}\right). \tag{2.17}$$

Here, β_G and β_R denote the value in the glassy state and rubbery state. C_* is the concentration when glass transition occurs. $D(C)$ is also changing during the transition between glass and rubber. In Cohen's model [128], D and E are taken as constant.

The dimensionless form of the model used in paper [128–130] introduces the following non-dimensional scale: the length scale, x; the time scale, $\tau = \frac{\rho E}{D} t$; the scale for concentration, C; the scale for the stress, S; and the scale for coefficient β. The equations governing the process read as,

$$\frac{\partial C}{\partial t} = d(\nabla C + \nabla S) \tag{2.18}$$

$$\frac{\partial S}{\partial t} = C - \lambda \beta S. \tag{2.19}$$

Here, the dimensionless parameter d and λ are defined as $d = \frac{D^2}{\rho E x^2}$ and $\lambda = \frac{\beta_R D}{\rho E}$. The variable β is evaluated from Eq.(2.17)). In paper [128], the values of parameters used in above equations are taken from experimental data and are selected as: $\lambda = 1$, $\beta_G = 0.1$, $\beta_R = 1.0$, $C_* = 0.5$ and $\delta = 0.1$.

2.2 Phase-field approach

The phase-field approach uses a so-called extended Fick's law for the description of diffusion by setting that the diffusive flux is proportional to the gradient of the chemical potential. In equilibrium, the chemical potentials of the adjoining phases are equal,

$$\mu_1 = \mu_2. \tag{2.20}$$

At the non-equilibrium state, the chemical potential in each phase is different and the difference in the chemical potential from its equilibrium value [3] can be used to determine the rate of a system towards its equilibrium [56, 67].

There are two kinetic models available in the phase-field approach to describe the phase transformation. One is the Landau-Ginzburg model and another one is the Cahn-Hilliard model. In Chapter 1, the details of these two models have been discussed and the Cahn-Hilliard model is used to describe diffusion within the liquid/liquid mixture.

2.2.1 Free energy function

To describe the experimental settings of the work [2], we restrict our analysis to isothermal system. The specific free energy function of the binary mixture is defined as follows [56],

$$f = f_0 + \frac{\varepsilon}{2}(\nabla C)^2. \tag{2.21}$$

Here, the first term at the right-hand side is the classical part of the free energy and the second term accounts for the surface tension effects. The capillary coefficient ε is assumed to be so small that the additional term can be neglected everywhere except for the places of larger concentration gradients, i.e. except interfaces.

The classical part of free energy f_0 defines the states of the mixture. We are interested in multi-phase systems where the phase transformations occur. A convenient description for such a system is given by the function proposed by Landau for the near-critical systems [56],

$$f_0 = a\,(C - C_{cr})^2 + b\,(C - C_{cr})^4. \tag{2.22}$$

Here, C_{cr} is the concentration at the critical point, a and b are two phenomenological parameters. In the near critical region, parameter a is proportional to temperature difference from the critical point, $(T \to T_{cr})$, and thus can be negative or positive. The second parameter b is always positive in the vicinity to the critical point.

For the convenience, the reference point of concentration is shifted from $(C - C_{cr})$ to C, and the Landau expression becomes [56]:

$$f_0 = AC^2 + C^4. \tag{2.23}$$

[3] The expression of the chemical potential used in the phase-field model is derived as follows. Firstly, the expression of the thermodynamic identity [67] for a liquid/liquid mixture reads as $de = Tds - pdV + \left(\frac{\mu_1}{m_1} - \frac{\mu_2}{m_2}\right) dC$ (here, e is the internal energy, T is the temperature, s is the entropy, p is the pressure, V is the volume, μ_1 and μ_2 are the chemical potential of each liquid, m_1 and m_2 are the molar mass of each liquid, C is the concentration). The chemical potential μ that used in our model is related with the chemical potential of each phase through the following expression $\mu = \frac{\mu_1}{m_1} - \frac{\mu_2}{m_2}$.

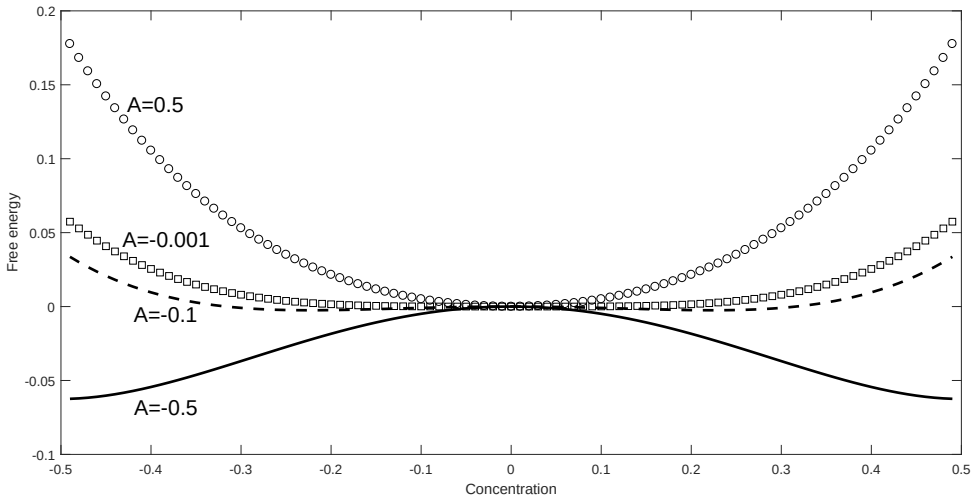

Fig. 2.1 A sketch of the Landau free energy function.

Here, the parameter $A = \frac{a}{b}$. If A is positive then the system is above the critical temperature and the equilibrium state of the mixture is homogeneous, and if A is negative then and system is below the critical temperature and the equilibrium state can be heterogeneous.

The relation between A and the free energy function is illustrated by a sketch in Fig.2.1, where four curves are drawn for $A = -0.5, -0.1, -0.001$, and 0.5. When $A = -0.5$, the free energy corresponding to the value of the concentration of the pure solvent/solute phase is lower than the free energy at centre (the mixture). When A increased but still be kept negative (we then plot the curve for $A = -0.1$ and -0.001, the curve is already closed to the curve for $A = 0$), there are two minimum points between the centre and the side of curve. This means the solvent and solute can mix but would stop once the concentration of solvent/solute reaches the minimum point. The value of the concentration at the minimum point is the value of the average concentration of the mixture. When A is positive ($A = 0.5$), the curve changes to be a down-hill shaped curve and it means the liquid can be mixed in any ratios.

Eq.(2.23) are written in the non-dimensional form and the scale of the specific free energy will be taken as $\mu_* = b$ and μ is the chemical potential derived from the free energy function ($\mu = \frac{df}{dC}$). The expression of the chemical potential μ, that includes both the classical and non-classical parts, is written as [122]:

$$\mu = Gry + \mu_0 - \varepsilon\nabla^2 C,\ \mu_0 = \frac{df_0}{dC} \tag{2.24}$$

At the right-hand side of the equation, the first term is the effect of barodiffusion (y is

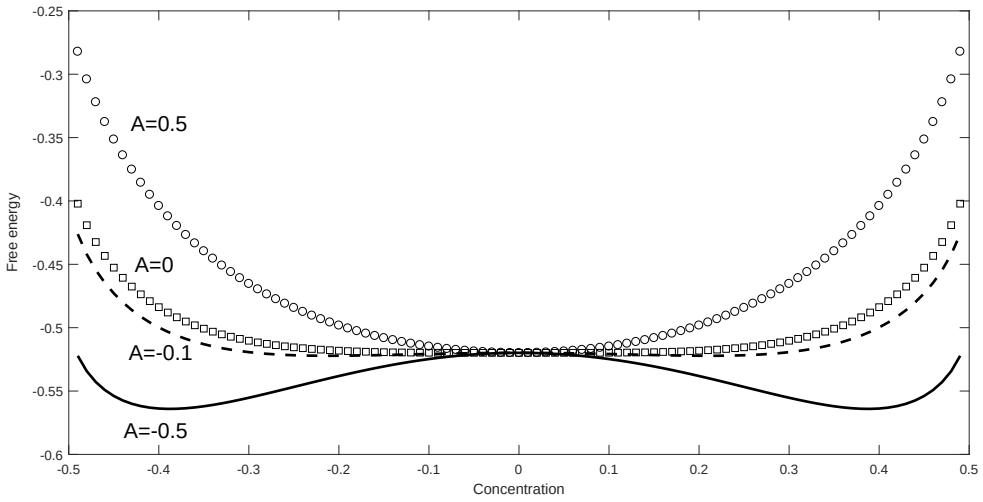

Fig. 2.2 A sketch of Eq.(2.25).

the vertical coordinate (y-axis)). The last term means that the surface tension defines the interface.

This expression works quite well near the critical point, but it will produce non-physical values of concentration if the system is far from the critical point. To get rid of the non-physical values for the concentration, we used the another function given by Cahn and Hilliard [112],

$$f_0 = \left(A - \frac{3}{2}\right) C^2 + \frac{3}{4}\left[\left(\frac{1}{2}+C\right)\ln\left(\frac{1}{2}+C\right) + \left(\frac{1}{2}-C\right)\ln\left(\frac{1}{2}-C\right)\right]. \tag{2.25}$$

The latter function coincides with the Landau expression near the critical point if the phase diagram is symmetric and $C_{cr} = 1/2$ [4]. Similarly, we also draw the sketch of this expression for $A = -0.5, -0.1, 0$, and 0.5 (in Fig.2.2). The curve for $A = -0.5$ is slightly shifted to be a "W" shaped curve, which suggests that diffusion will occur spontaneously but stopped when the average concentration reached 0.388.

Expression.(2.25) is known as the regular-solution expression [111]. Within this expres-

[4] Firstly, we change the reference points for the concentration: $C_{new} = C_{old} - \frac{1}{2}$ and the expression of the regular solution used in paper [112] can be written as: $f_0 = \omega\left(\frac{1}{4} - C^2\right) + kT\left[\left(\frac{1}{2}+C\right)\ln\left(\frac{1}{2}+C\right) + \left(\frac{1}{2}-C\right)\ln\left(\frac{1}{2}-C\right)\right]$. The Taylor series expansion of the above the expression near $C = 0$ generates $f_0 = -kT\ln 2 + \frac{1}{4}\omega + (2kT - \omega)C^2 + \frac{4}{3}kTC^4 + ...$ Compared with the Landau expression, the expression of the regular solution can be related by introducing the following substitutions: $f_0 = -kT\ln 2 + \frac{1}{4}\omega$, $a = 2kT - \omega$, $b = \frac{4}{3}kT$, $A = \frac{a}{b}$.

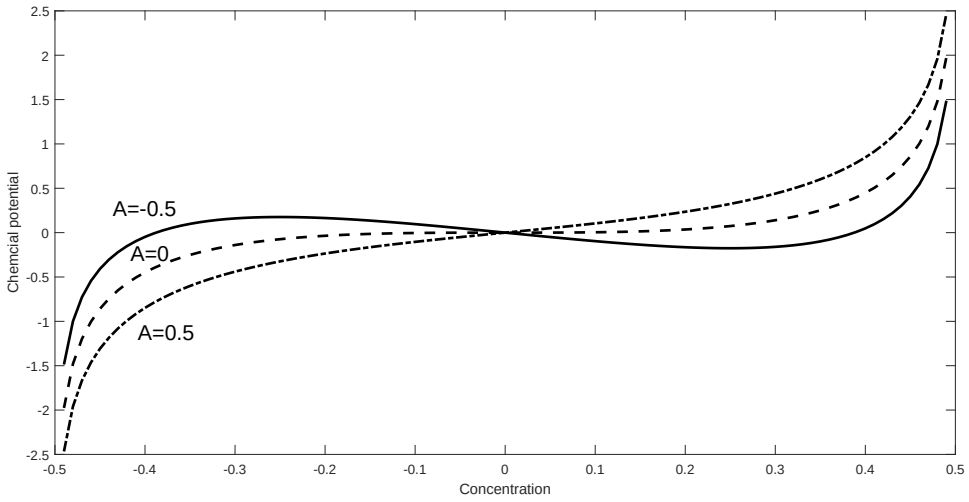

Fig. 2.3 A sketch of the function of the chemical potential (Eq.(2.26)).

sion, the classical part of the chemical potential needs to be rewritten as [111]:

$$\mu_0 = 2(A - \frac{3}{2})C + \frac{3}{4}\ln\frac{\frac{1}{2}+C}{\frac{1}{2}-C}. \tag{2.26}$$

The profile of chemical potential defined by Eq.(2.26) are drawn in Fig.2.3. The value of average concentration of mixtures can be found when $\mu = 0$.

2.2.2 Cahn-Hilliard model and Cahn-Hilliard-Navier-Stokes model

The governing equations need to be written in non-dimensional form, and the following non-dimensional scales are introduced: L_* is the typical length; $\tau_* = \frac{L_*}{v_*}$ is the time scale; $v_* = \mu_*^{1/2}$ is the velocity scale; ρ_* is the typical density; $p_* = \rho_*\mu_*$ is the typical pressure; and also $\mu_* = b$ is the typical value of the chemical potential.

The expression of chemical potential includes the classical part (Eq.(2.26)) and the non-classical part (Eq.(2.24)),

$$\mu = \mu_0 - Ca\nabla^2 C. \tag{2.27}$$

The non-dimensional parameters used in this equation are defined as: The capillary number,

$$Ca = \frac{\varepsilon}{\mu_* L_*^2}. \tag{2.28}$$

The thermal parameter A,

$$A = \frac{a}{b}. \tag{2.29}$$

The Cahn-Hilliard equation reads as:

$$\frac{\partial C}{\partial t} = \nabla^2 \mu. \tag{2.30}$$

If the hydrodynamics is included, the Cahn-Hilliard-Navier-Stokes equation is used to describe the conservations of mass, momentum, and species. As it has been introduced in Chapter 1, the equation is firstly derived by Lowengrub and Truskinovskii [113]. Their model [113] includes the quasi-compressibility effect and this limits the uses of the model. In paper [122], this problem was solved and the Boussinesq approximation of the Cahn-Hilliard-Navier-Stokes equations was derived. The full set of the governing equations reported in paper [122] are written as:

$$\begin{aligned} \nabla \cdot \vec{v} &= 0, \\ \frac{\partial \vec{v}}{\partial t} + (\vec{v} \cdot \nabla)\vec{v} &= -\nabla p + \frac{1}{Re}\nabla^2 \vec{v} - Ca\nabla^2 C \nabla C + GrC\vec{\gamma}, \\ \frac{\partial C}{\partial t} + (\vec{v} \cdot \nabla)C &= \frac{1}{Pe}\nabla^2 \mu. \end{aligned} \tag{2.31}$$

The equations include the following non-dimensional parameters: The Reynolds number,

$$Re = \frac{\rho_* \mu_*^{\frac{1}{2}} L_*}{\eta_*}. \tag{2.32}$$

The Peclet number,

$$Pe = \frac{\rho_* L_*}{\alpha \mu_*^{\frac{1}{2}}}. \tag{2.33}$$

Here, α is the coefficient of mobility. And the Grashof number,

$$Gr = \phi \frac{g L_*}{\mu_*}. \tag{2.34}$$

Here, g being the gravitational acceleration, and $\phi = \frac{\rho_2 - \rho_1}{\rho_1}$ being the density contrast of two liquids.

Diffusion coefficient in the phase-field approach

The results of the phase-field simulations could be correlated with the Fick's model, if the diffusion coefficient is introduced as follows,

$$D_{phase-field} = \frac{\alpha \mu_*}{\rho_*} \frac{\partial \mu_0}{\partial C} = \alpha \mu_* \left(\frac{3}{1 - 4C^2} - (3 - 2A) \right). \tag{2.35}$$

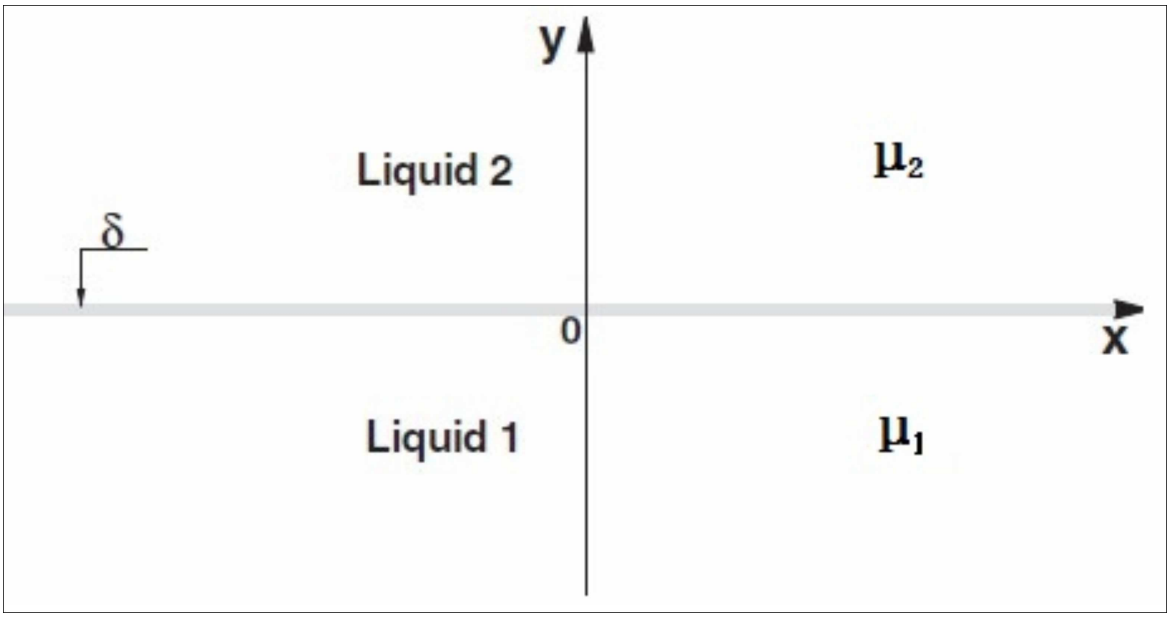

Fig. 2.4 A flat interface between two fluids. μ_1 is the chemical potential of fluid 1; μ_2 is the chemical potential of fluid 2; δ is the thickness of the interface.

This expression does not take into account of the Cahn-Hilliard addition to the chemical potential, and thus it is negative at $C \to 0$ (within interfaces) if $A < 0$. That is the reason why the Cahn-Hilliard addition is needed, as it makes the overall diffusion coefficient positive within the interface zones. Far from interfaces, $D_{phase-field}$ can be used as the diffusion coefficient in either solute or solvent phases. The coefficient is concentration-dependent growing when $|C| \to \frac{1}{2}$. The expression (Eq.(2.35)) produces greater values for the diffusion coefficients in the solvent and solute phases (in comparison with the diffusion coefficient in Fick's law for diffusion). This means that the dissolution simulated by the phase-field simulations should be faster than the classical Fickian model.

A flat interface

In this section, we want to illustrate the equations written in the previous section by considering a simple horizontal flat interface separating two liquids (In Fig.2.4). For simplicity, we assume that there are no hydrodynamic flows and the effect of the gravity is also negligible.

At the state of equilibrium, the chemical potential is constant. Since the value of the chemical potential is defined with an accuracy of an arbitrary constant, we may assume $\mu = 0$ in equilibrium. Hence, we have:

$$2AC + 4C^3 - Ca\frac{\partial^2 C}{\partial x^2} = 0. \tag{2.36}$$

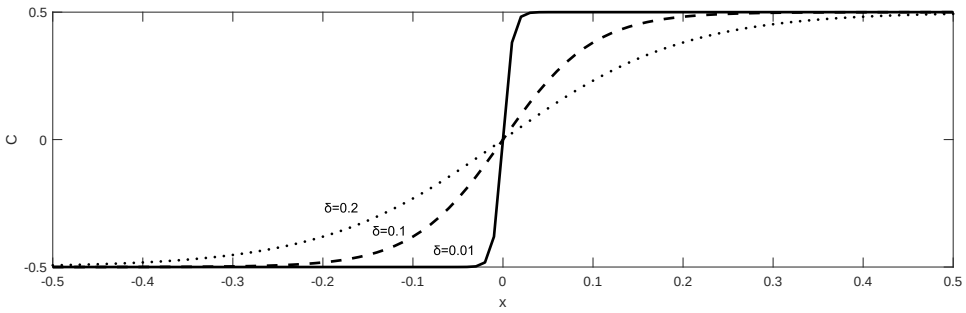

Fig. 2.5 A sketch of Eq.(2.37)($C_0 = 0.5$).

To solve this equation, we seek a solution in the following form:

$$C = C_0 \tanh \frac{x}{\delta}. \tag{2.37}$$

Such solution (Eq.(2.37)) gives a continuous profile of the diffused interface, which is schematically shown in the Fig.2.5. C_0 is the amplitude and δ denoted the thickness of the interface. In Fig.2.5, three curves were plotted for cases of $\delta = 0.2$, $\delta = 0.1$ and $\delta = 0.01$. It can be seen that the interfaces tend to sharp when the interface is thicker.

By substitution of the assumed solution into Eq.(2.36), the equation reads as,

$$\left(A + \frac{Ca}{\delta^2}\right) + \left(2C_0^2 - \frac{Ca}{\delta^2}\right) \tanh^2 \frac{x}{\delta} = 0. \tag{2.38}$$

From Eq.(2.38), we can get two equations $A + \frac{Ca}{\delta^2} = 0$ and $2C_0^2 - \frac{Ca}{\delta^2} = 0$, which gives us the following expression of δ and A:

$$\delta = \sqrt{-\frac{Ca}{A}}, \tag{2.39}$$

$$C_0 = \pm\sqrt{-\frac{A}{2}}. \tag{2.40}$$

This shows the thickness of the interface depends on both capillary number and parameter A. It needs to be noticed that these equations only valid when A is negative due to the condition of $-A > 0$. This also implies that the solution (Eq.(2.37)) to Eq.(2.36) is only valid for negative A.

The surface tension read as,

$$\sigma = Ca \int_{-\infty}^{+\infty} \left(\frac{\partial C}{\partial x}\right)^2 dx. \tag{2.41}$$

Substituting the first derivative of the concentration of Eq.(2.37) into Eq.(2.41), the following relationship can be obtained

$$\sigma = \frac{2}{3} A^2 \delta. \tag{2.42}$$

If we substitute Eq.(2.39) into Eq.(2.42), it can be seen that the surface tension of the interface also depends on the values of Ca number and A.

Chapter 3

Numerical procedure

In chapter 2, the governing equations that can produce the observations in the diffusion experiments of solvent/solute mixture are introduced. The analytical solution to the full set of the governing equation can only be found with extremely limited boundary conditions. Thus, to reproduce the experiment observations, the governing equation need to be solved numerically through the finite difference approach. The idea of the method is to solve the governing equations in a domain of solution of (x(space),t(time)). It discretizes the computational space domain and the duration of the process by various spatial steps (Δx) and time intervals (Δt). Then the derivatives in the governing equations are replaced by their finite difference analogues with Δx and Δt. In this chapter, we introduce the numerical procedures to solve the governing equations.

3.1 The model geometry and imposed boundary conditions

In this section, we introduced the model geometry, the boundary condition and initial conditions that reproduce the experimental configuration in paper [2]. Firstly, we test the capability of the Fick's law with 1D model. The 1D formulation of the experiment configuration in paper [2] is as follows: a tube at position from $x = 0$ to $x = l$ (here, l is the tube length) is initially filled with the solute. Mathematically, this initial condition of the problem can be expressed as: for all x,

$$C_{initial} = 1 \tag{3.1}$$

and the boundary conditions are (at $x = 0$ and $x = l$),

$$C_{initial} = 0. \tag{3.2}$$

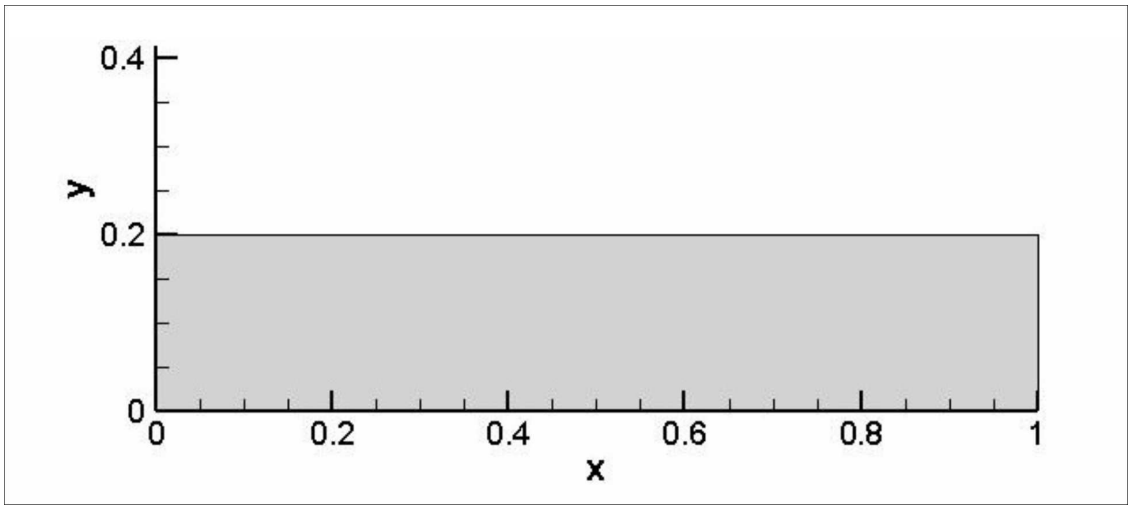

Fig. 3.1 The geometry of a single capillary tube.

Then the model is extended to the 2D Cartesian coordinates (x,y) . At the beginning, the geometry of a rectangular tube (in Fig.3.1) is used to model the capillary tube in the experiment [2]. To mimic the experimental settings, it is assumed that the capillary is initially saturated with the solute and then the solvent penetrates from two open ends at left and right sides of the tube. Thus, the initial condition of the model is to set $C = 1$ inside the tube and also $C = 0$ at the left and right boundaries. At the lower and upper plates, boundary conditions are set assuming no diffusion flux through the walls (zero normal derivatives of concentration at the walls),

$$\frac{\partial C}{\partial y} = 0. \tag{3.3}$$

Next, we repeated these simulations for the more sophisticated geometry (in Fig.3.2), that includes two blocks initially filled with the solvent connected with the open sides of the tube (filled by the solute). Such a geometry should be a closer reproduction of the experiment [62] because it allows to accurately describe the hydrodynamics of the solvent outside the tube. The boundary conditions need to be redefined. The initial condition is: at the left and right blocks, the area is filled with solvent and numerically represented by,

$$C = 0; \tag{3.4}$$

Similarly, the capillary tube part is filled with solute,

$$C = 1. \tag{3.5}$$

At the connection section between the block and the tube, a set of matching conditions

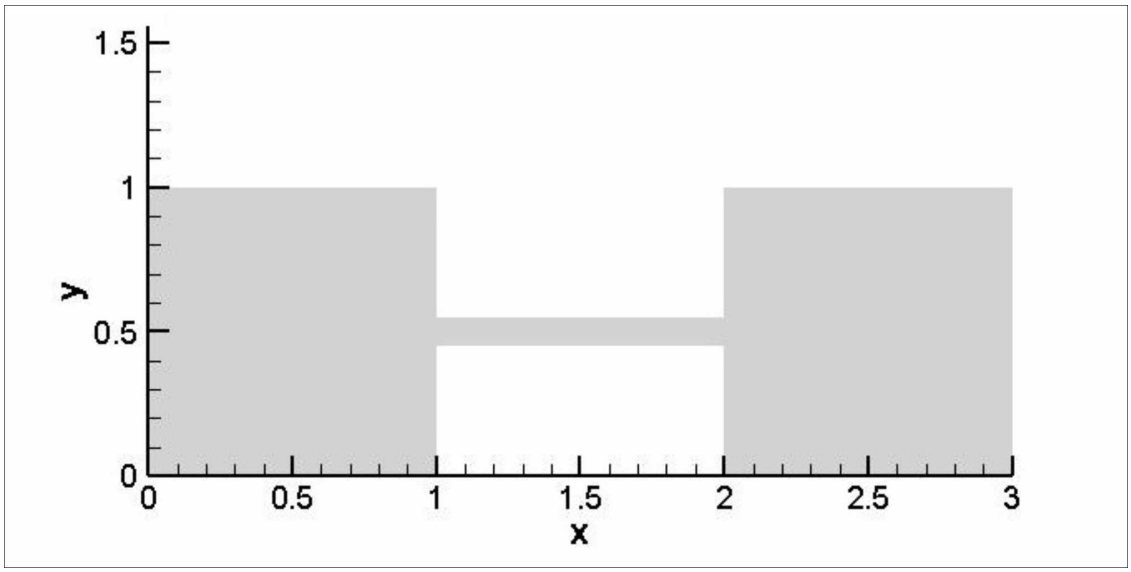

Fig. 3.2 The geometry of a single capillary tube with two blocks at both open ends.

is required,

$$C_{tube} = C_{block}, \tag{3.6}$$

$$\omega_{tube} = \omega_{block}. \tag{3.7}$$

Here, C_{block} and ω_{block} are calculated from the classical Fick's law and Naiver-Stokes equations.

For the boundary conditions at the walls of the tube and blocks, zero derivatives of concentration are imposed, which states the absence of diffusion flux through the walls,

$$\frac{\partial C}{\partial n} = 0. \tag{3.8}$$

With this geometry, we were also able to study the effect of the solutal convective flows. If hydrodynamics is included, the boundary conditions for the velocity field are required. In this case, it is assumed that the block geometry is enclosed by rigid walls and hence the no-slip boundary conditions are imposed for walls,

$$\vec{v} = 0. \tag{3.9}$$

We also develop a new model for diffusion on the basis of the phase-field approach. The governing equations for the phase field model for this case are written in Chapter 2. The calculations are fulfilled for the same geometries of a single capillary as in Fig.3.1 and for the configuration with two blocks, as shown in Fig.3.2.

The governing equations need to be supplemented with the new boundary conditions. The initial conditions are same as for the Fickian case. In the Landau free energy function, the value of the concentration is defined by the double-wall potential (see Fig.2.1), and thus the range of concentration variation is shifted from $(0;1)$ to $(-0.5;0.5)$. Thus, the new initial and boundary conditions are stated as below: At the open sides of the tube (in the Fig.3.2), it is at the solvent blocks),

$$C_{initial} = -0.5; \tag{3.10}$$

Inside the capillary tube,

$$C_{initial} = 0.5. \tag{3.11}$$

At the connection section between the block and the tube,

$$C_{tube} = C_{block}, \tag{3.12}$$

$$\mu_{tube} = \mu_{block}, \tag{3.13}$$

$$\omega_{tube} = \omega_{block}. \tag{3.14}$$

Here, C_{block}, μ_{block} and ω_{block} are calculated from the Cahn-Hilliard-Navier-Stokes equations.

The initial condition in the field of the velocity is unchanged, which is written as:

$$\vec{v} = 0. \tag{3.15}$$

The rest of boundary conditions need to be redefined because the phenomenological relation is different. The absence of the diffusive flux through the walls is mathematically defined by zero normal derivatives of the chemical potential at the boundaries,

$$\frac{\partial \mu}{\partial n} = 0. \tag{3.16}$$

Furthermore, since the governing equations of the phase-field approach are of the fourth order in terms of the concentration, the additional conditions are required for the field of concentration, which define the wetting conditions at the wall. As it has been discussed in the Chapter 2, two extreme cases are considered in this work. Firstly, it is assumed that the wall is neutral to the components of the mixture, so the contact line is orthogonal to the

wall. This can be defined by imposing zero normal derivatives of concentration at the wall.

$$\frac{\partial C}{\partial y} = 0. \tag{3.17}$$

Secondly, another set of boundary conditions is based on the assumption that the molecules of the solute that initially saturates the tube remain attached to the wall. This boundary condition is mathematically defined by imposing the concentration level at the wall equal to the concentration of the solute,

$$C = 0.5. \tag{3.18}$$

3.2 The vorticity-stream-function formulation

The formulated mathematical model will be solved numerically for the $1D$ and $2D$ plane layer and for the $2D$ block geometries discussed in the above section. The governing equations introduced in Chapter 2 are a set of the partial differential equations. The partial differential equations (PDE) are classified by three types, namely, hyperbolic, parabolic, and elliptic. Different types of the partial differential equation describe different behaviours for a particular system and the methods to solve problem are different. The classification of PDEs (hyperbolic, parabolic, or elliptic) is determined by the coefficients of the highest-order derivatives in the equation [134]. In this section, we only discuss the governing equations used in this work, i.e. the classical Fick's law, the Cahn-Hilliard equation, the Navier-Stokes equation and the equation of continuity. The classical Fick's law (Eq.(2.1)) and the Cahn-Hilliard equation (Eq.(2.30)) are the parabolic partial differential equations. The Navier-Stokes equation (Eq.(2.5) or Eq.(2.31)) is the partial differential equation of the mixed types of the hyperbolic part (convective terms), the parabolic part(viscous terms), and the elliptic part (pressure and incompressibility). The main model of this work will be two-dimensional. This means that the model (Eq.(2.5) or Eq.(2.31)) can be simplified by adopting the vorticity-stream-function formulation. The derivation of this simplification will be introduced in this section.

To start with, we write the full set of the Cahn-Hilliard-Navier-Stokes equations,

$$\nabla \cdot \vec{v} = 0, \tag{3.19}$$

$$\frac{\partial \vec{v}}{\partial t} + (\vec{v} \cdot \nabla)\vec{v} = -\nabla p + \frac{1}{Re}\nabla^2 \vec{v} - C\nabla\mu + 2GrC\vec{y}, \tag{3.20}$$

$$\frac{\partial C}{\partial t} + (\vec{v} \cdot \nabla) C = \frac{1}{Pe} \nabla^2 \mu, \tag{3.21}$$

$$\mu = Gry + 2(A - \frac{3}{2})C + \frac{3}{4} \ln \frac{\frac{1}{2} + C}{\frac{1}{2} - C} - Ca \nabla^2 C. \tag{3.22}$$

The above governing equations are supplemented with the following boundary conditions for the rigid walls,

$$\frac{\partial \mu}{\partial n} = 0, \frac{\partial C}{\partial n} = 0, \vec{v} = 0. \tag{3.23}$$

In a 2D Cartesian coordinates (x,y), the governing equations are written as:

$$\frac{\partial v_x}{\partial x} + \frac{\partial v_y}{\partial y} = 0, \tag{3.24}$$

$$\frac{\partial v_x}{\partial t} + v_x \frac{\partial v_x}{\partial x} + v_y \frac{\partial v_x}{\partial y} = -\frac{\partial p}{\partial x} + \frac{1}{Re} \nabla^2 v_x - C \frac{\partial \mu}{\partial x}, \tag{3.25}$$

$$\frac{\partial v_y}{\partial t} + v_x \frac{\partial v_y}{\partial x} + v_y \frac{\partial v_y}{\partial y} = -\frac{\partial p}{\partial y} + \frac{1}{Re} \nabla^2 v_y - C \frac{\partial \mu}{\partial y} + 2GrC, \tag{3.26}$$

$$\frac{\partial C}{\partial t} + v_x \frac{\partial C}{\partial x} + v_y \frac{\partial C}{\partial y} = \frac{1}{Pe} \left(\frac{\partial^2 \mu}{\partial x^2} + \frac{\partial^2 \mu}{\partial y^2} \right), \tag{3.27}$$

$$\mu = Gry + 2(A - \frac{3}{2})C + \frac{3}{4} \ln \frac{\frac{1}{2} + C}{\frac{1}{2} - C} - Ca \left(\frac{\partial^2 \mu}{\partial x^2} + \frac{\partial^2 \mu}{\partial y^2} \right). \tag{3.28}$$

And the rigid wall boundary conditions are written as,

$$\frac{\partial \mu}{\partial x} = 0, \frac{\partial \mu}{\partial y} = 0; \tag{3.29}$$

$$\frac{\partial C}{\partial x} = 0, \frac{\partial C}{\partial y} = 0; \tag{3.30}$$

$$v_x = 0, v_y = 0. \tag{3.31}$$

The pressure term can be eliminated through $\frac{\partial Eq.(3.25)_x}{\partial y} - \frac{\partial Eq.(3.26)_y}{\partial x}$, which gives,

$$\frac{\partial}{\partial t}\left(\frac{\partial v_x}{\partial y}-\frac{\partial v_y}{\partial x}\right)+\frac{\partial}{\partial y}\left(v_x\frac{\partial v_x}{\partial x}\right)+\frac{\partial}{\partial y}\left(v_y\frac{\partial v_x}{\partial y}\right)-\frac{\partial}{\partial x}\left(v_x\frac{\partial v_y}{\partial x}\right)-\frac{\partial}{\partial x}\left(v_y\frac{\partial v_y}{\partial y}\right)$$
$$=\frac{1}{Re}\Delta\left(\frac{\partial v_x}{\partial y}-\frac{\partial v_y}{\partial x}\right)-\frac{\partial}{\partial y}\left(C\frac{\partial \mu}{\partial x}\right)+\frac{\partial}{\partial x}\left(C\frac{\partial \mu}{\partial y}\right)-2Gr\frac{\partial C}{\partial x} \quad (3.32)$$

The stream-function ψ is introduced as:

$$v_x=\frac{\partial \psi}{\partial y}, v_y=-\frac{\partial \psi}{\partial x}. \quad (3.33)$$

This satisfied the equation of continuity,

$$\frac{\partial}{\partial x}\left(\frac{\partial \psi}{\partial y}\right)+\frac{\partial}{\partial y}\left(-\frac{\partial \psi}{\partial x}\right)=0. \quad (3.34)$$

The vorticity is defined as

$$\omega=\frac{\partial v_y}{\partial x}-\frac{\partial v_x}{\partial y}. \quad (3.35)$$

The Poisson equation that describes relation between the vorticity and the stream-function reads as,

$$\omega=-\nabla^2\psi. \quad (3.36)$$

Substituting these changes into the Navier-Stokes equation, and the equation of motion can be written as,

$$\frac{\partial \omega}{\partial t}+\frac{\partial \psi}{\partial y}\frac{\partial \omega}{\partial x}-\frac{\partial \psi}{\partial x}\frac{\partial \omega}{\partial y}=\frac{1}{Re}\nabla^2\omega+\frac{\partial \mu}{\partial x}\frac{\partial C}{\partial y}-\frac{\partial \mu}{\partial y}\frac{\partial C}{\partial x}+2Gr\frac{\partial C}{\partial x}. \quad (3.37)$$

Now we could write the full set of governing equation with the vorticity-stream formulations as,

$$\omega=-\frac{\partial^2\psi}{\partial x^2}-\frac{\partial^2\psi}{\partial y^2}, \quad (3.38)$$

$$\frac{\partial \omega}{\partial t}+\frac{\partial \psi}{\partial y}\frac{\partial \omega}{\partial x}-\frac{\partial \psi}{\partial x}\frac{\partial \omega}{\partial y}=\frac{1}{Re}\nabla^2\omega+\frac{\partial \mu}{\partial x}\frac{\partial C}{\partial y}-\frac{\partial \mu}{\partial y}\frac{\partial C}{\partial x}+2Gr\frac{\partial C}{\partial x}, \quad (3.39)$$

$$\frac{\partial C}{\partial t}+\frac{\partial \psi}{\partial y}\frac{\partial C}{\partial x}-\frac{\partial \psi}{\partial x}\frac{\partial C}{\partial y}=\frac{1}{Pe}\left(\frac{\partial^2\mu}{\partial x^2}+\frac{\partial^2\mu}{\partial y^2}\right), \quad (3.40)$$

$$\mu = Gry + 2(A - \frac{3}{2})C + \frac{3}{4}\ln\frac{\frac{1}{2}+C}{\frac{1}{2}-C} - Ca\left(\frac{\partial^2 C}{\partial x^2} + \frac{\partial^2 C}{\partial y^2}\right). \tag{3.41}$$

The new set of governing equations requires additional boundary conditions for the stream function ψ and vorticity ω. The boundary conditions of these calculations for ψ are derived from the velocity field. In the original form of the governing equations (Eq.(3.19-3.22)), the boundary conditions for velocity are $v_x = 0$ and $v_y = 0$. Thus, the boundary conditions of stream function at all walls of the tube and blocks can be written as,

$$\frac{\partial \psi}{\partial y} = 0, \frac{\partial \psi}{\partial x} = 0; \tag{3.42}$$

Thus, the formulations (Eq.(3.42)) suggest that ψ can be defined to be constant along the tube wall, and any constant added to the stream-function ψ does not change the velocity field (v_x and v_y). It should be noticed that the stream-function is just an intermediate variable defined to solve the Poisson equation and it has no physical meanings. Thus, the reference point for ψ can be selected arbitrarily in this model. We take the point (0,0) as the reference point and set the value of ψ to be zero. Then, because of the setting of the boundary condition for ψ (Eq.(3.42)), the values of ψ at boundaries will be just 0. Hence, the final setting of boundary condition for the stream-function ψ can be written as,

$$\psi = 0. \tag{3.43}$$

The governing equations also requires boundary condition for the voticity ω, which is obtained by using Eq.(3.38). Because of the fact that the values of ψ take values of zero along the tube wall, the derivatives of ψ along the wall boundaries should be zero. Thus, at the tube walls, we will have,

$$\omega = -\frac{\partial^2 \psi}{\partial x^2} - \frac{\partial^2 \psi}{\partial y^2} = 0 - \frac{\partial^2 \psi}{\partial y^2}. \tag{3.44}$$

The above condition is applied for the upper and lower plate of the capillary tube. In the model with the added solvent blocks, the boundary conditions of ω are required in both both x-axis and y-axis, so the boundary conditions for ω should be written as,

$$\omega = -\frac{\partial^2 \psi}{\partial y^2}, \omega = -\frac{\partial^2 \psi}{\partial x^2}. \tag{3.45}$$

The boundary conditions for the field of the chemical potentialμ and the concentration C remains the same (Eqs.(3.29) and (3.30)).

The solution to the Poisson equation

The Poisson equation (vorticity field) is solved by the Gauss-Seidel method [134]. This method is considered to be faster than the Jacobi iteration method of the five-point discretization formula of a steady problem described by the Poisson equation [134]. The 2D formulation of the Gauss-Seidel approach reads as,

$$\psi_{qx,qy}^{k+1} = \frac{1}{\frac{2}{(\Delta x)^2}+\frac{2}{(\Delta y)^2}}[-\omega_{qx,qy} + \frac{\left(\psi_{qx-1,qy}^{k+1}+\psi_{qx+1,qy}^{k}\right)}{(\Delta x)^2} + \frac{\left(\psi_{qx,qy-1}^{k+1}+\psi_{qx,qy+1}^{k}\right)}{(\Delta y)^2}]. \quad (3.46)$$

Here, The index k is the number of iteration. The value of vorticity ω is obtained from the Cahn-Hilliard-Navier-Stokes equations. The accurate approximation of ψ is obtained through the iteration comparing the difference between approximate solution ψ of two consequent iterations. A schematic diagram of this procedure is shown in the schematic diagram (3.3). This criterion rule of these calculations is expressed as,

$$e^k = \left|\psi^k - \psi^{k-1}\right|. \quad (3.47)$$

This method needs an initial approximated value for ψ to start, and the iteration finished when the convergence criterion is reached [134]. In this work, we set this initial value to be $\psi = 0$, and the value of the criterion of convergence is set as $e \leq 10^{-5}$.

3.2.1 The finite-difference approach

In this work, the governing equation is solved by the finite-difference method. There are various finite difference schemes available for the computational simulations. The advantages and disadvantages are analysed in book [134]. Fick's equation or Cahn-Hilliard equation is of the first order in time and second order in space. In this work, we selected the 2nd order central difference scheme for space derivatives and the explicit, forward difference scheme for for time derivatives. The finite-difference analogue of the Fick's law can be written as:

$$\frac{\left(C_q^{n+1}-C_q^n\right)}{\tau} = \frac{(C_{q+1}^n - 2C_q^n + C_{q-1}^n)}{h^2}. \quad (3.48)$$

Here, the expression at left-hand side is the first order finite-difference formula and the expression at right-hand side is of the second order. Indexes n and q are used to characterise the step number of variable in the iteration. τ is the step size of time and h is the step size of distance.

For the Cahn-Hilliard model, the finite difference form of the species transport equation

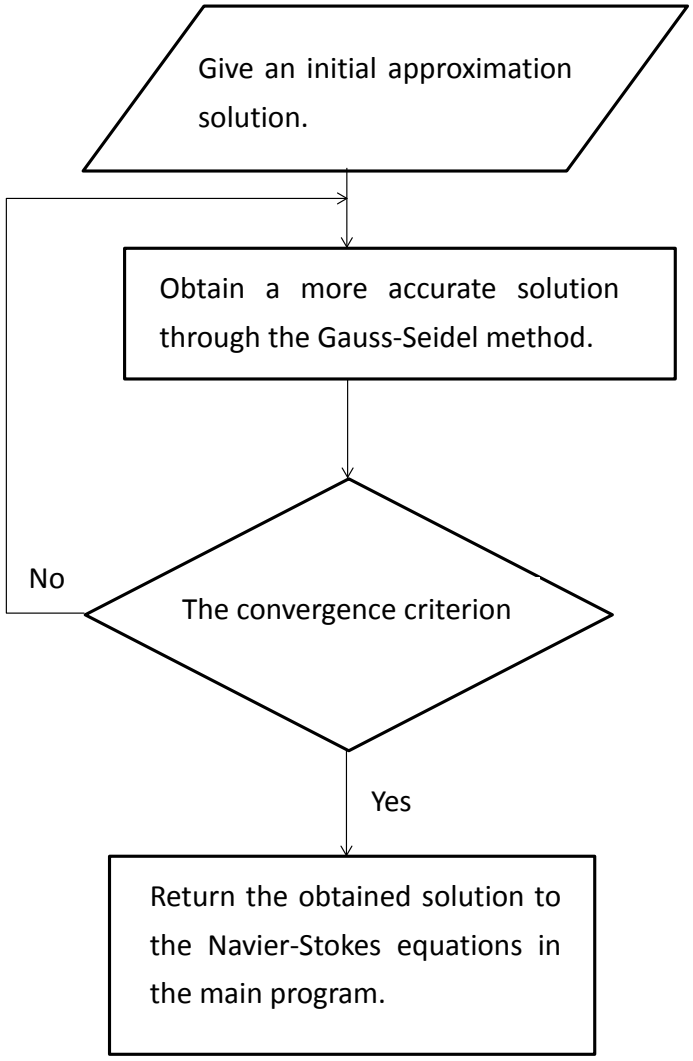

Fig. 3.3 The schematic diagram of the iteration procedure to solve the vorticity field.

reads,

$$\frac{C_q^{n+1}-C_q^n}{\tau}=\frac{\mu_{q+1}^n-2\mu_q^n+\mu_{q-1}^n}{h^2}. \tag{3.49}$$

This equation needs to be coupled with the equation for the chemical potential. This can be either defined by the Landau expression [56],

$$\mu_q^n=2AC_q^n+4\left(C_q^n\right)^3-Ca\frac{C_{q+1}^n-2C_q^n+C_{q-1}^n}{h^2}; \tag{3.50}$$

or the "regular solution" function [111],

$$\mu_q^n=2(A-\frac{3}{2})C_q^n+\frac{3}{4}\ln\frac{\frac{1}{2}+C_q^n}{\frac{1}{2}-C_q^n}-Ca\frac{C_{q+1}^n-2C_q^n+C_{q-1}^n}{h^2}. \tag{3.51}$$

The Fickian model, the phase-field approach need to be coupled with the Navier-Stokes equations if the hydrodynamics is included. We also need to write the finite difference form for the full set of the Cahn-Hilliard-Navier-Stokes model. Since the hydrodynamics is introduced in a 2D geometry, we will write the 2D finite difference form of the governing equation. In the 2D Cartesian coordinates (x,y), we define h_x as the spatial differences in x-axis and h_y as the spatial differences in y-axis. New notations q_x and q_y are also needed to characterise the number of the spatial steps of variable. The numerical form of the full set of the Cahn-Hilliard-Navier-Stokes equation will be written as,

$$\begin{aligned}
&\frac{\omega_{qx,qy}^{n+1}-\omega_{qx,qy}^n}{\tau}+\frac{1}{4}\frac{\psi_{qx,qy+1}^n-\psi_{qx,qy-1}^n}{h_y}\frac{\omega_{qx+1,qy}^n-\omega_{qx-1,qy}^n}{h_x}-\\
&\qquad\frac{1}{4}\frac{\psi_{qx+1,qy}^n-\psi_{qx-1,qy}^n}{h_x}\frac{\omega_{qx,qy+1}^n-\omega_{qx,qy-1}^n}{hy}=\\
&\qquad\frac{1}{Re}\left(\frac{\omega_{qx+1,qy}^n-2\omega_{qx,qy}^n+\omega_{qx-1,qy}^n}{h_x^2}+\frac{\omega_{qx,qy+1}^n-2\omega_{qx,qy}^n+\omega_{qx,qy-1}^n}{h_y^2}\right)+\\
&\qquad\frac{1}{4}\frac{\mu_{qx+1,qy}^n-\mu_{qx-1,qy}^n}{h_x}\frac{C_{qx,qy+1}^n-C_{qx,qy-1}^n}{h_y}-\\
&\qquad\frac{1}{4}\frac{\mu_{qx,qy+1}^n-\mu_{qx,qy-1}^n}{h_y}\frac{C_{qx+1,qy}^n-C_{qx-1,qy}^n}{h_x}+\frac{Gr}{2}\frac{C_{qx+1,qy}^n-C_{qx-1,qy}^n}{h_x},
\end{aligned} \tag{3.52}$$

$$\frac{C^{n+1}_{qx,qy}-C^{n}_{qx,qy}}{\tau}+\frac{1}{4}\frac{\psi^{n}_{qx,qy+1}-\psi^{n}_{qx,qy-1}}{hy}\frac{C^{n}_{qx+1,qy}-C^{n}_{qx-1,qy}}{h_x}-$$
$$\frac{1}{4}\frac{\psi^{n}_{qx+1,qy}-\psi^{n}_{qx-1,qy}}{hx}\frac{C^{n}_{qx,qy+1}-C^{n}_{qx,qy-1}}{h_y}=$$
$$\frac{1}{Pe}\left(\frac{\mu^{n}_{qx+1,qy}-2\mu^{n}_{qx,qy}+\mu^{n}_{qx-1,qy}}{h_x^2}+\frac{\mu^{n}_{qx,qy+1}-2\mu^{n}_{qx,qy}+\mu^{n}_{qx,qy-1}}{h_y^2}\right), \tag{3.53}$$

and the chemical potential is calculated by,

$$\mu^{n}_{qx,qy}=Grh_yq_y+2(A-\frac{3}{2})C^{n}_{qx,qy}+\frac{3}{4}\ln\frac{\frac{1}{2}+C^{n}_{qx,qy}}{\frac{1}{2}-C^{n}_{qx,qy}}-$$
$$Ca\left(\frac{C^{n}_{qx+1,qy}-2C^{n}_{qx,qy}+C^{n}_{qx-1,qy}}{h_x^2}+\frac{C^{n}_{qx,qy+1}-2C^{n}_{qx,qy}+C^{n}_{qx,qy-1}}{h_y^2}\right). \tag{3.54}$$

It should be noticed that the first term in Eq.(3.54) represents the effect of barodiffusion. This term is not appear in 1D model and that is a feature of 2D model. The Poisson equation for the vorticity-stream formulation is solved by Eq.(3.46) and the numerical procedure has already been introduced in the last section.

3.3 1D and 2D model

To conduct the simulation, the FORTRAN codes were written based on the above mathematical model and numerical form, with the supplement of the initial boundary conditions introduced in section 3.1. The simulations have been conducted in both 1D and 2D model. The 1D model just simply represents the concept that the solvent entering into a horizontal tube filled with solute from its left and right side. The 2D model of a single capillary tube is directly extended from the 1D concept, but it allows to model the incline shape of the interface, which is one important experimental observation in paper [2]. Thus, the diffusive evolution of miscible liquids cannot be classified as 1D. Besides, in a mixture with the strong density difference, the barodiffusion should be taken into account and the modelling of the barodiffusion need to be built in 2D geometry.

The geometry of the direct extended 2D model (from the 1D concept) is just a single capillary. Within 2D model, we could modify geometry with the side-added blocks of solvent, which is a better representation of the experimental configuration. With the help of this new geometry, it allows us predict the pattern of solvent flows entering into the capillary tube filled with solute. In the subsequent chapter, it will be introduced that the geometry of

the side-added blocks affects the time-dependence of the diffusion rate. The 3D model gives the full features of the geometry of the tube and blocks. It would provide more details about the motion of the fluids. Thus, we want to perform the 3D simulations to check if there are other potential factors affect the diffusion kinetics.

3.4 3D model

The 3D model is extended with help of the commercial CFD software ANSYS Fluent. This software solves the PDEs through the finite element method, which takes the surface integral of the values inside a cell divided by the computational grids. In Fluent, diffusion is evaluated via the species transport equation. For a mixture of different phases, the governing equations are same with the previous Fickian diffusion model (Eq.(2.5)). In the Fluent solver, the pressure field is solved by the pressure-velocity approach [134].

The glycerine/water mixture is selected for the numerical model because this mixture has been examined in experiments [2]. For the glycerine/water mixture, the concentration dependence of the diffusion coefficient is expressed as $D = 1.6 \times 10^{-10}(1 - 0.895C)\,\frac{m^2}{s}$ [62]. Fluent does not provide this specific expression of the diffusion coefficient, but it allows to modify the coefficient in the species transport equation by imposing a user defined functions file (UDF) of the expression of diffusion coefficient. The density of the mixture is calculated through the volume-weighted-mixing-law, and the viscosity of the mixture is calculated through the mass-weighted-mixing-law.

Fig.3.4 shows the configurations of the model that are implemented in the Fluent solver. Similar to the previous simulations, it is set that the capillary tube is initially filled with the solute and the solvent enters into the tube from two open sides. The aspect ratio (the length of the tube over the tube diameter) is kept to be 10:1. The simulations started with cases that the tube diameter equals to 0.4mm (as in the experiments [2]). The tube length is set to 4mm and then is increased to 5cm for further simulations.

To conduct a simulation of the diffusion between two liquids, the species transport model in Fluent and filled the properties of the mixture with the information of glycerol and water. We created two model geometries. In single tube model, the upper and lower plate were imposed with the rigid wall boundary condition. The right and left tube ends were imposed with inlet boundary condition and the inlet diffusion is enabled. All cell zones are defined as mixture. We set the mass fraction of pure glycerol phase is 1 and the water phase is 0. Initially, the tube is filled with glycerol and then the water phase flows into the tube form tube's open sides. Thus, the initial condition are the mass fraction is set as 1 inside the tube and 0 at the left and right boundaries of the tube. In block model, the inlet boundary

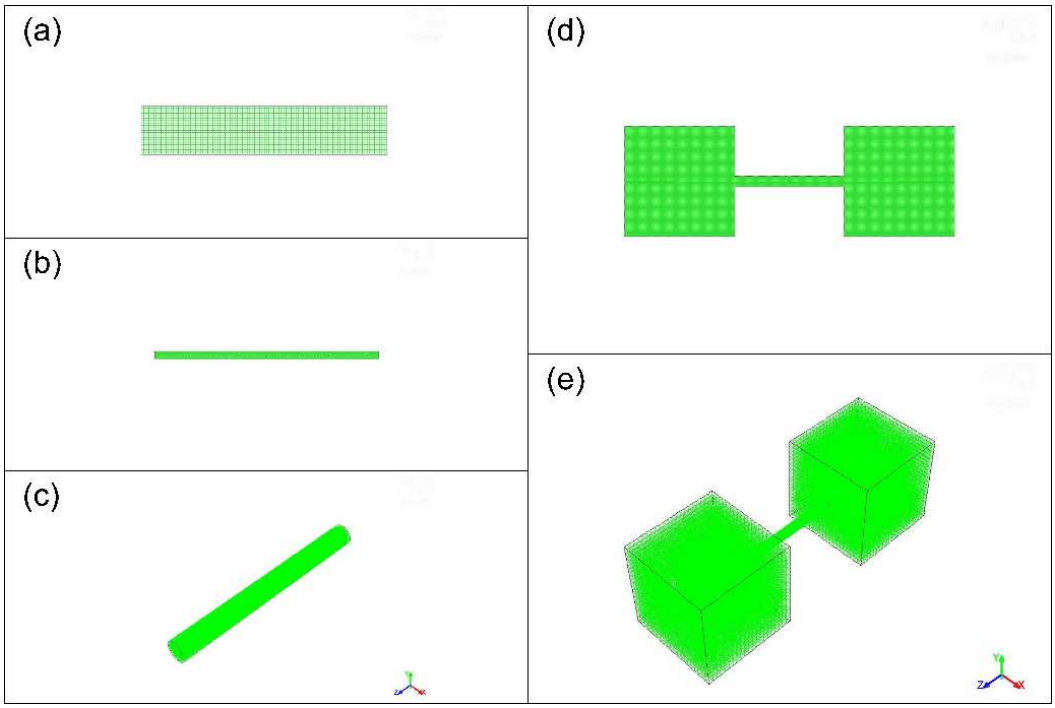

Fig. 3.4 The geometry of the model.

conditions at tube's open sides are replaced by blocks. The mass fraction of glycerol is set as 1 in the tube and 0 in the blocks to represent the experimental configuration. Then the pressure-based solver is used for calculation. The evaluation of gradients is solved by least squares cell-based method. The rest of quantities are solved through the second order upwind scheme.

3.5 Numerical accuracy of the model

The finite difference method gives the approximated solutions. To illustrate this, we write the Taylor series expansion of the concentration in the finite difference procedure as:

$$\frac{\partial C_q^n}{\partial x} = \frac{C_q^{n+1} - C_q^n}{\delta x} - \frac{\partial^2 C_q^n}{\partial x^2}\frac{\delta x}{2!} - \frac{\partial^3 C_q^n}{\partial x^3}\frac{(\delta x)^2}{3!} - \ldots \tag{3.55}$$

It can be seen that the error of the solution is generated by the terms with higher order of δx. The computational errors are produced unavoidably during the simulations, and these errors will be accumulated through the iterations. These round-off errors affect the accuracy of the simulation and can even make the simulation unstable. In this work, the finite difference

scheme of Fick's equation or Cahn-Hilliard equation can be written as,

$$\frac{\left(\mu_q^{n+1}-\mu_q^n\right)}{\Delta t}+O\left(\Delta t\right)=\frac{\left(\mu_{q+1}^n-2\mu_q^n+\mu_{q-1}^n\right)}{h^2}+O\left(h^2\right). \tag{3.56}$$

Here, $O\left(\Delta t\right)$ and $O\left(h^2\right)$ are the truncation errors produced from the time and spacial derivatives. The scheme of the finite difference method can improved to increase the accuracy and stability but the computational time also increases. In book [134], different finite difference schemes are introduced and the numerical error was analysed by the Neumann method (on the basis of the Fourier expansions) or the matrix method.

To control the round-off errors, the proper size of each time step was determined empirically under the balance of the stability problem and the reasonable computational time. Besides, the basic requirement for the accuracy of the computational mesh in this work is to capture all the typical length scales, including the liquid/liquid boundaries. This means the size of a step between two computational nodes must be smaller than the thickness of the interface and should also allow for a good approximated calculation for the higher order scheme of the Cahn-Hilliard equation. Thus a basic requirement can be,

$$\delta \geq 4\Delta h. \tag{3.57}$$

Here, δ is the interface thickness and h is the size of a computational mesh cell.

The quality of the computational mesh is ensured by using the uniform computational grid, which avoid the variations between the neighbouring grid steps. To show the accuracy of our selections, we ran one phase-field simulation as an example. The parameters used in the simulation are $A=-0.5$ and $Ca=2.5\cdot 10^{-5}$, which are limited by the computational resources available for us. The simulation was repeated within same geometry and with different computational mesh. The evaluations of the rate of mass transferring are depicted in Fig.3.5. From Fig.3.5, a good agreement between cases with two different resolutions can be observed. This means the resolution with 100×20 is already capable of providing accurate results for the current work.

The accuracy and stability of the model is also affected by the size of the time interval of discretization. The optimized size of the each time step changes with the variation of the parameters used in the model. Thus the most optimized time step needs to be determined for each simulation. The procedure to find the time step used in the work is shown in the schematic diagram (3.6).

About 3D simulations based on the specie transport model in ANSYS Fluent, the size of the computational mesh is 2×10^{-5}m, which is in the same ratio as in the previous

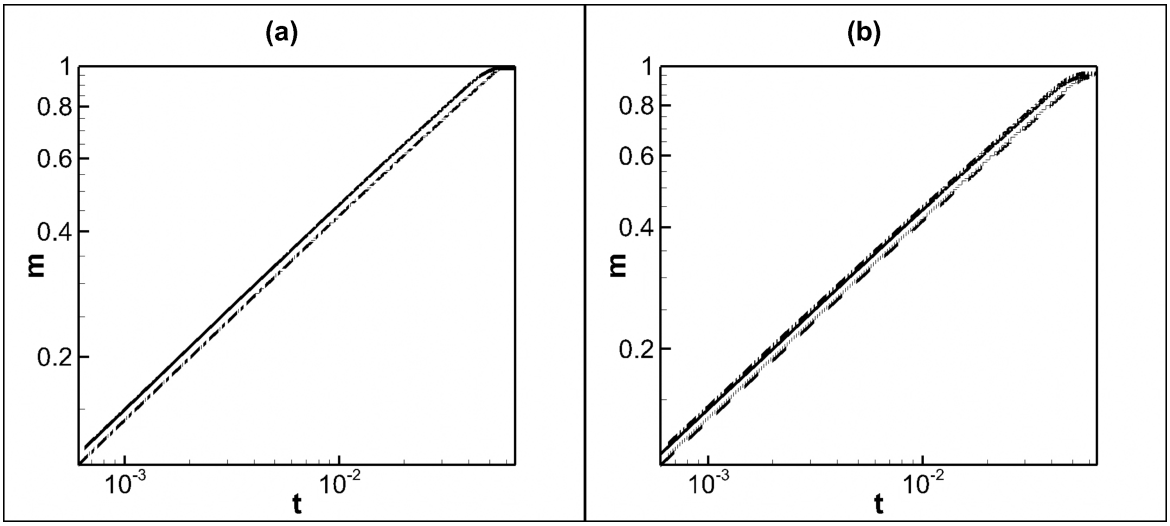

Fig. 3.5 The comparison of the calculated mass of solvent within the tube with two different resolutions (100×20 and 150×30). The parameter used for these calculation are $A = -0.5$ and $Ca = 2.5 \times 10^{-5}$, and $Gr = 1$. (a) For the cases of the neutral walls. For smaller tube ($d = 0.1$), the resolution$= 100 \times 20$, dash-dot line, the resolution$= 150 \times 30$, dotted line; For larger tube ($d = 0.8$): the resolution$= 100 \times 20$, solid line, the resolution$= 150 \times 30$, dash-dot-dot line; (b) For the case of the solute-philic walls condition. For smaller tube ($d = 0.1$), the resolution$= 100 \times 20$, dashed line, the resolution$= 150 \times 30$, dotted line; For larger tube ($d = 0.8$): the resolution$= 100 \times 20$, solid line, resolution$= 150 \times 30$, dash-dot-dot line.

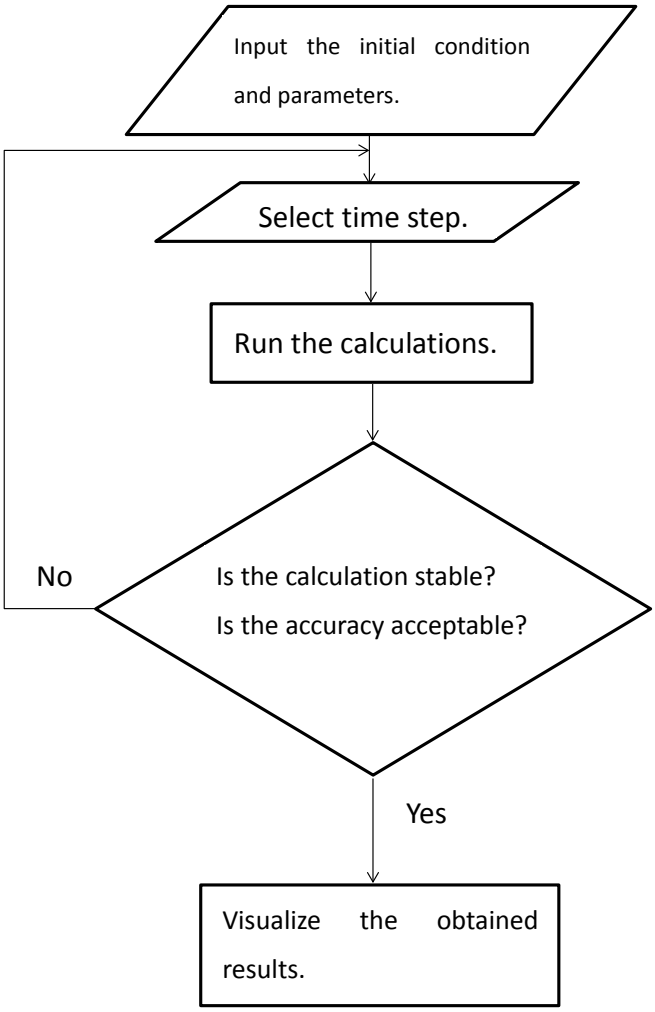

Fig. 3.6 The schematic diagram of the procedure to determine the size of the time step.

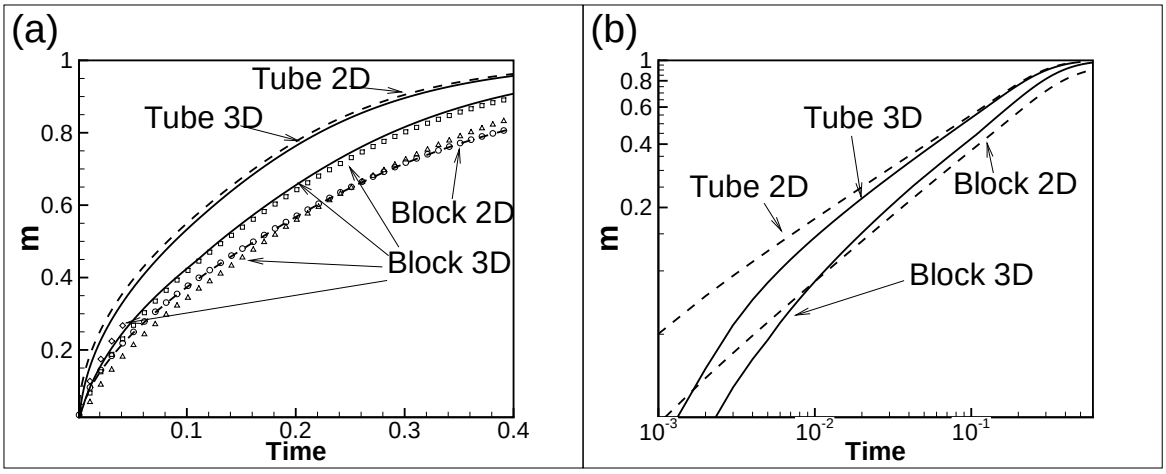

Fig. 3.7 The mass of solvent penetrating into the tube as a function of time. (a) shows the data plotted in normal scale; and the curves in (b) are same data in logarithmic scale. In both (a) and (b), the sold lines are for 2D data and the dashed lines are for 3D data. In (a), the circle symbols is for 2D block data with a mesh size of 4×10^{-5}m, the delta symbols is for 3D block data with a mesh size of 1×10^{-5}m, the square symbols is for 3D block data with a mesh size of 1.5×10^{-5}m, the diamond symbols is for 3D block data with a mesh size of 4×10^{-5}m.

simulations. To test that the results are mesh-independent, the comparison of the different sizes of the computational mesh were changed from 4×10^{-5}m to 1×10^{-4} as shown in Fig.3.7(a). It can also be seen that the 3D data coincide with the 2D data. Despite small differences, a good convergence can be observed among these curves. Hence it is possible to conclude that 2×10^{-5}m is sufficient to produce accurate results.

Chapter 4

Results and discussion

4.1 Experimental results

This chapter will display the numerical results. This work aims to reproduce the observations of the interfacial diffusion of the liquid/liquid mixture reported in the paper [2]. The configuration of the experiments [2] is simple: a long capillary tube is saturated with one liquid (solute) and then the tube was immersed into a thermostatic solvent-filled bath. The tube and solvent block are made of fused quatz and borosilicate glass. The tube wall material is considered to be perfectly wettable for both water and glycerol. Both ends of the capillary tube remain open. The capillary tube was placed horizontally into the bath and no pressure gradients were applied between the tube ends (see Fig.(4.1)).

The experiments were conducted with different liquid/liquid mixtures, in particular, with the glycerol/water mixture and the soybean oil/hexane mixture. In contrast with the common expectations that could be derived on the basis of the Fick's law, two interfaces between two

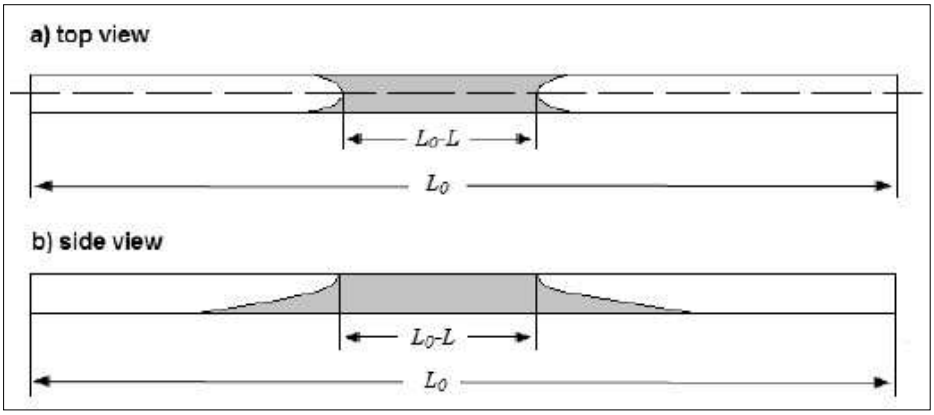

Fig. 4.1 A sketch of the experimental configuration reported in the paper [2].

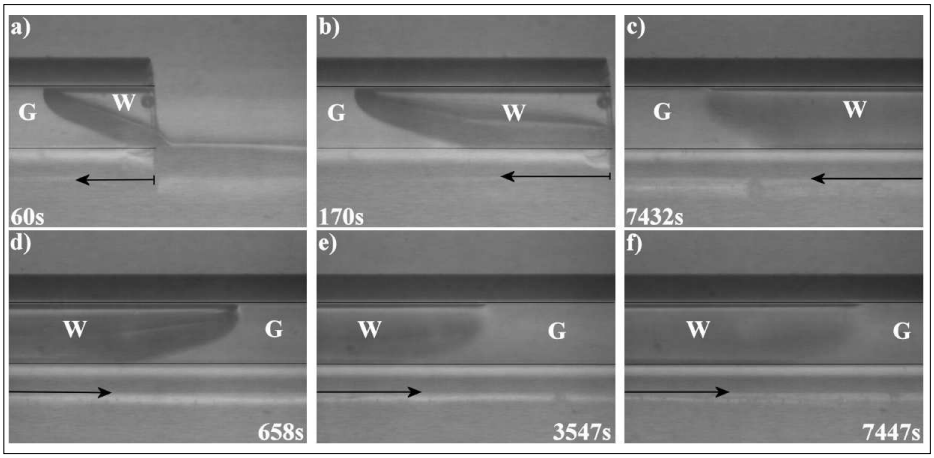

Fig. 4.2 The observations of the shape of the glycerol(G)/water(W) interface reported in the experimental work [2]. The upper row and lower row show the interfaces entering into the tube from different sides of the capillary tube.

liquids were formed at two sides of the tubes, and then were observed moving towards the middle of the tube. The speed of the interface propagation was considerably faster than the speed of the interface smearing, and thus the interfaces remained visible for very long time periods (see Fig.(4.2)).

The experiment [2] aim to study the rate of the dissolution between solute and solvent and they characterised it as the length of the capillary tube occupied by solvent, which can represent the amount the solvent entering the tube and the amount of solute getting out of the tube. It is reported that the rate of dissolution was found to time dependent, with $t^{\frac{2}{3}}$ time dependence in the beginning and $t^{\frac{1}{3}}$ time dependence at later time moments (In Fig.4.3). In addition, it was observed that the interface should be endowed with the surface tension because the inclined shape of the interface could only be described by the balance of the capillary and gravity forces. The hydrodynamic flows were found negligible, and the evolution of the dissolution was diffusion-driven. The experiments were done in tubes with different diameters and the rate of dissolution depends on the tube's diameter. In general, the dissolution occurs slower in the tubes of smaller diameter and the dependence of the dissolution rate on the tube's diameter is quadratic. Besides, the $\frac{2}{3}$ time dependence maintained for a longer time for the larger tube. In this work, we aim to develop a theoretical model capable of producing similar observations, and in this way, to develop the theory for the miscible liquid/liquid mixtures.

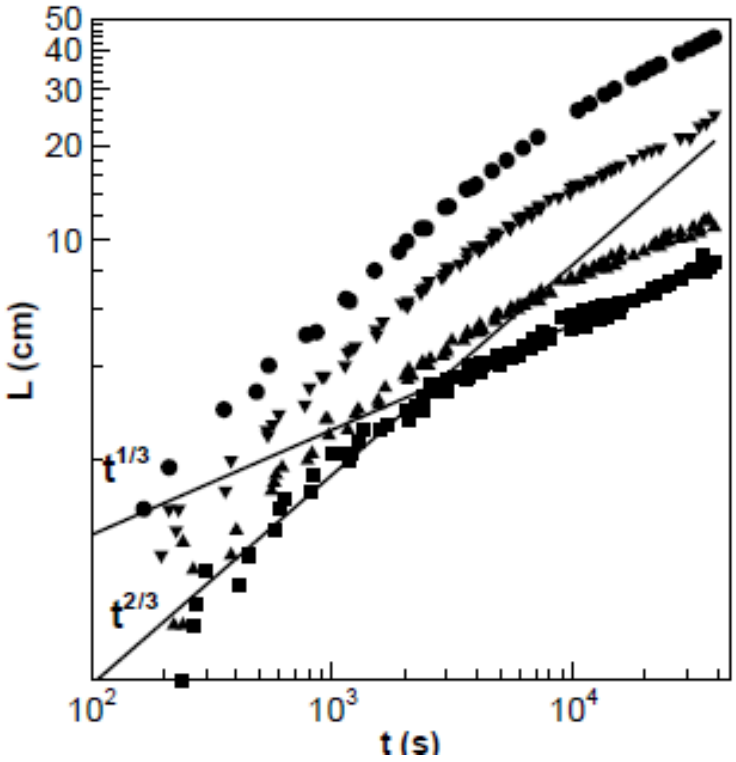

Fig. 4.3 The rate of diffusion in glycerol/water reported in paper [2]. This figure shows the data measured under $20°C$. The figure also compares data under different tube diameters, namely, 0.6mm (the square symbols), 0.8mm (the orthodox triangles symbols), 1.2mm (the reversed triangles symbols), 1.6mm (the circle symbols).

4.2 Results for the Fickian model

4.2.1 1D model

We start the simulations by examining the classical Fick's law. The calculation was initially done within the geometry of a single capillary tube (see Fig.(3.1)). The process is governed by the classical Fick's law (see Eq.(2.1)), with a concentration-dependent diffusion coefficient which is measured in the glycerol/water mixture. The expression for this diffusion coefficient is $D = 1.6 \cdot 10^{-10}(1 - 0.895C)m^2 \cdot s^{-1}$.

The calculations conducted for the one dimensional case are depicted in Fig.(4.4). From Fig.(4.4), one can see that the concentration inside the capillary tube changes over time, indicating the solvent phase penetrating into the tube. The rate of diffusion was evaluated through the rate of mass transfer ($\int_0^1 (1-C)dx$). The amount of mass transfer was plotted in Fig.(4.5) as a function of time. As it can be seen from Fig.(4.5), the rate of mass transfer ($\frac{dm}{dt}$) was time-dependent and exhibits the classical Fickian time-dependence ($t^{\frac{1}{2}}$). After $t = 0.1$, the curve starts to disobey the $t^{\frac{1}{2}}$ law (In Fig.(4.5)). This should be explained by the Fickian behaviours at the later times of diffusion, which has been introduce in Chapter 1. The obtained behaviour is observed to be same with the published observations of diffusion at later times (in Fig.(1.9)). This later-times Fickian behaviour occurs after $t = 0.083$, which also agrees with the theoretical exception [1]. Thus, it can be concluded that the observed results just exhibit the Fickian behaviours.

4.2.2 2D model

Then the simulations were extended to 2D cases. The 2D model (in Fig.4.7(a)) provides more information about the solvent/solute boundaries. As it can be expected, the obtained results reproduce the feature of the classical Fickian diffusion (in Fig.4.7(a)), i.e. the solute/solvent boundaries smeared and eventually form a single homogeneous phase through diffusion. It should be noticed that the solvent/solute boundaries are found to remain stationary at the open sides of the tube. During the entire process, the solvent/solute boundaries are only getting thicker and wider through a slow smearing process (in Fig.4.7). This does not agree with the experimental observation of the movement of the visible interface in paper [2].

We also compares the kinetics of Fickian diffusion with the experiment data reported in paper [2]. In the experimental work [2], the rate of diffusion was evaluated through the observations of the speed of interface propagation. However, the solute/solvent boundaries produced from the classical Fickian approach are relatively diffusive, which makes it im-

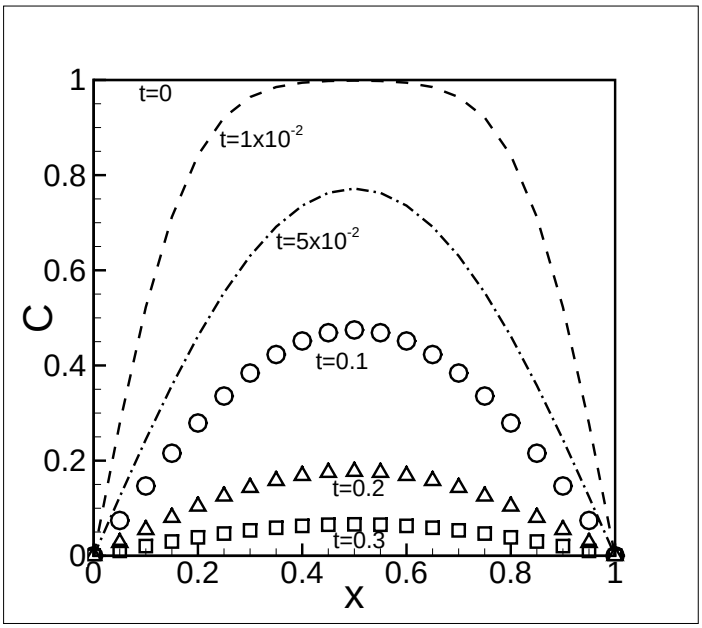

Fig. 4.4 The numerical result for the 1D model, with the assumption that the diffusion process is determined by the Fick's law. The diffusion coefficient used for calculations is defined as $D = 1.6 \cdot 10^{-10}(1 - 0.895C)m^2 \cdot s^{-1}$.

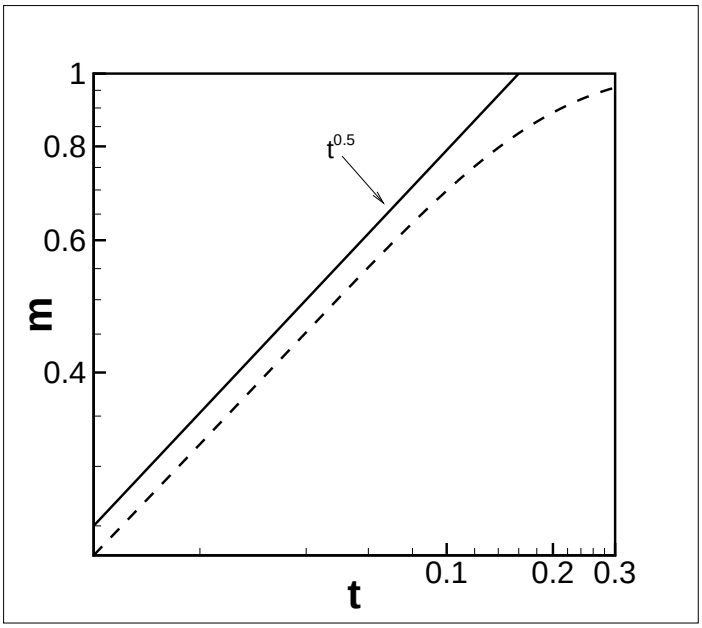

Fig. 4.5 The mass of solvent penetrating into the tube for the one dimensional case of Fickian diffusion in logarithmical scale. The result is depicted by the dashed line and the solid line is defined as $m \propto t^{0.5}$ and is used as a reference line.

possible to track the position of the interface. Hence, instead of tracking the solute/solvent interface, the rate of diffusion is characterised by the amount of the mass of the solvent penetrating into the tube. Mathematically this is defined as $m = \frac{1}{Ly}\int_0^1 (1-C)dV$ (L_y is the height of the rectangular domain and V is the volume of the domain.). The result from both the one dimensional and the two dimensional cases were observed similarly (in Fig.(4.5) and Fig.(4.8)), with the rate of mass transfer ($\frac{dm}{dt}$) proportional to $t^{\frac{1}{2}}$.

The effect of the solvent-filled blocks

In above cases, the effect of hydrodynamics was not included. Through paper [2] examined a diffusion-dominated problem, flows should be existed and we try to introduce hydrodynamics into the model to check whether the kinetics of diffusion can be affected by this addition. This addition requires new boundary condition for the velocity field and the condition at two open sides of tube is unknown because it is unclear how solvent flows into the capillary tube. Thus, we build the second geometry where two solvent-filled blocks are added at the sides of the tube. The addition of the solvent-filled blocks simulates the experimental configuration of the solvent-filled bath that the solute-filled tube is immersed inside.

With the help of side-added solvent blocks, the pattern of flows can be evaluated correctly. Otherwise, for the geometry with just a solute-filled tube, the artificial velocity field must be used. We firstly examined the Fickain diffusion without flows in this new geometry. The concentration field of this case is shown in Fig.4.7(b). The observation of the interface remains similar with the previous simulation. However, the rate of diffusion was observed to follow the 0.6 time-dependence. This difference can be explained by the variation in the concentration field at the connecting part between the tube and blocks (in Fig.4.7(b)). In the single capillary model, the values of concentration at the left and right entries of the tube is defined as a constant value that refers to the pure solvent phase. In the block model, the open ends of the tube are connected to two blocks filled with the solvent. Through the addition of these solvent blocks, the values of concentration at the tube's open ends are no longer constant. A clear description can be made through recording the average concentrations of the phases (in Fig.4.6). In both phases, the concentration field is changed by the action of diffusion and eventually reaches an equilibrium value when diffusion ends. The variation in the average concentration of the solvent phase is small because the amount of solvent in the blocks is much higher than the amount of the solute in the tube.

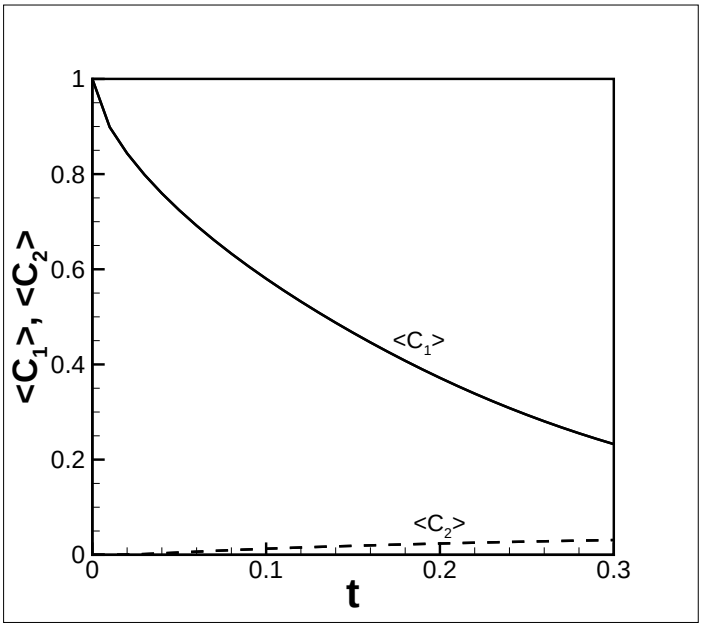

Fig. 4.6 The average concentrations of the solute ($< C_1 >$) and solvent ($< C_2 >$) phases in the entire domain as the function of time. The diffusion coefficient used for calculations is defined as $D = 1.6 \cdot 10^{-10}(1 - 8.95 \cdot 10^{-1}C)m^2 \cdot s^{-1}$.

The role of hydrodynamics

Then we studied the effects hydrodynamic flows on the dissolution process. The effect of hydrodynamics was deemed to be negligible in the experimental work [2], and we wanted to assess this conclusion through the numerical study. The governing equations have already been shown in Chapter 2 (Eq.2.5). The governing equations (Eq.2.5) contain the non-dimensional parameters and the estimations of these non-dimensional parameters (*Gr* and *Re*) for the glycerol/water mixture gives very small Reynolds numbers, 10^{-4} and very large Grashoff numbers, 10^{17} [5]. In addition, we were able to obtain the results for the Grashoff numbers up to 10^9. At higher numbers, the induced hydrodynamic flows and the gravity stratification becomes so strong that the concentration values become non-physical, i.e. below 0 and above 1.

The snapshots of concentration and velocity fields are depicted in Fig.4.7(c). The diffusion fronts remain diffusive. With the help of the gravity, the curved shaped diffusive zones were observed, which indicates that the hydrodynamic flow could partially remove

[5] *Re* number is defined as $Re = \frac{\rho_1 D_0}{\eta} = \frac{D_0}{\eta_k}$, here η_k is kinematic viscosity. For the glycerol/water mixture, the value of D_0 is at level of $10^{-10}\frac{m^2}{s}$ and η_k is at level of $10^{-6}\frac{m^2}{s}$. Thus the corresponding *Re* number is about 10^{-4}. *Gr* number is defined $Gr = \phi\frac{gL_*^3}{D_0^2}$. We take g as $10\frac{m}{s^2}$, L as $0.1m$ and ϕ is about 0.2. Then the value of *Gr* number is about 10^{17}.

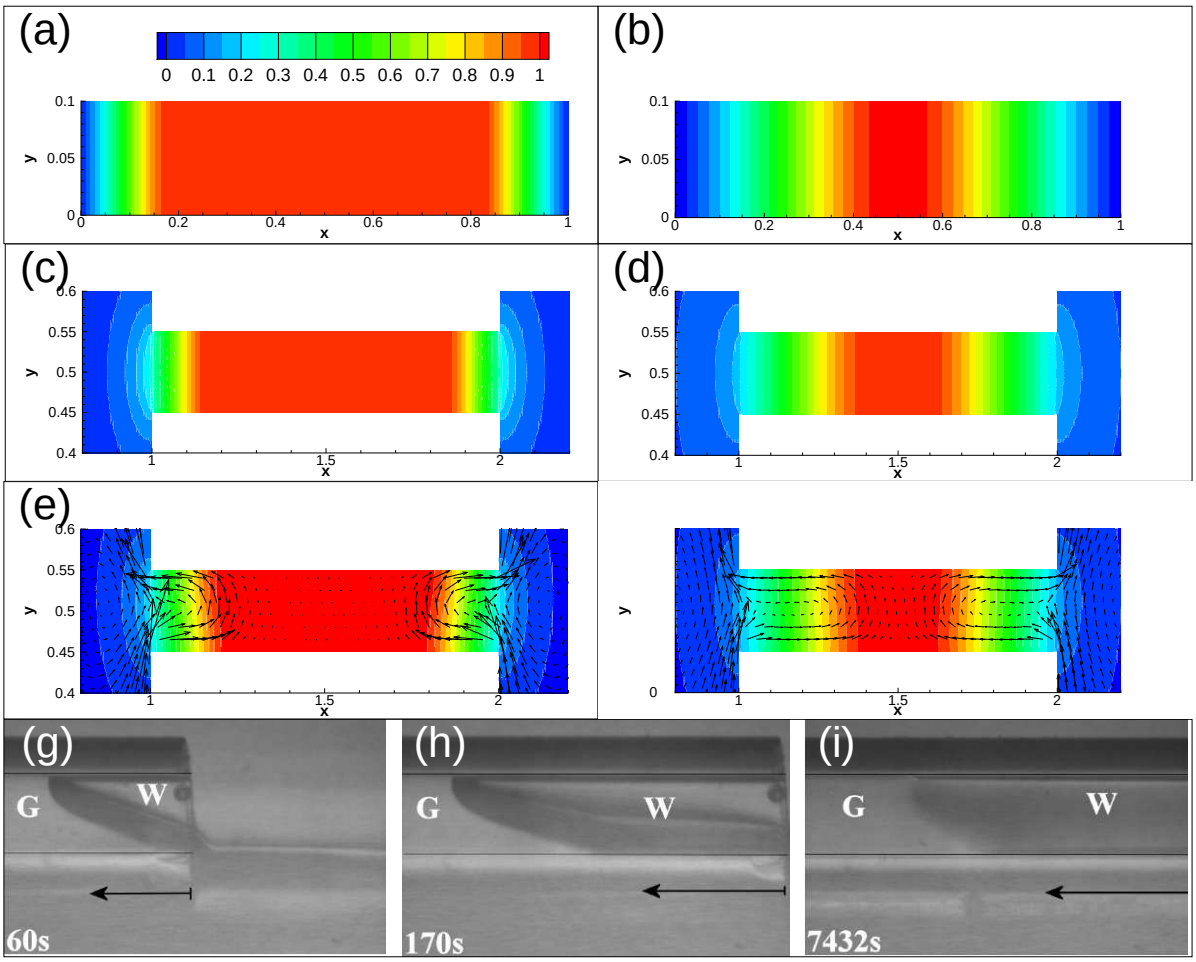

Fig. 4.7 The Fickian evolution in the solute/solvent mixture. (a,c,e) show the snapshots of the concentration and velocity fields at $t = 0.005$; (b,d,f) show the snapshots of same cases at $t = 0.03$; (g,h,i) show the shape of the glycerol/water interface observed in paper [2]('G' represents the glycerol phase and 'W' represents the water phase). (a,b) the results are obtained for the single capillary tube; (c,d) the block geometry without hydrodynamic effects ($Gr = 0$); and (e,f) the block geometry with account of the solutal convection ($Gr = 10^9$ and $Re = 10^{-4}$).

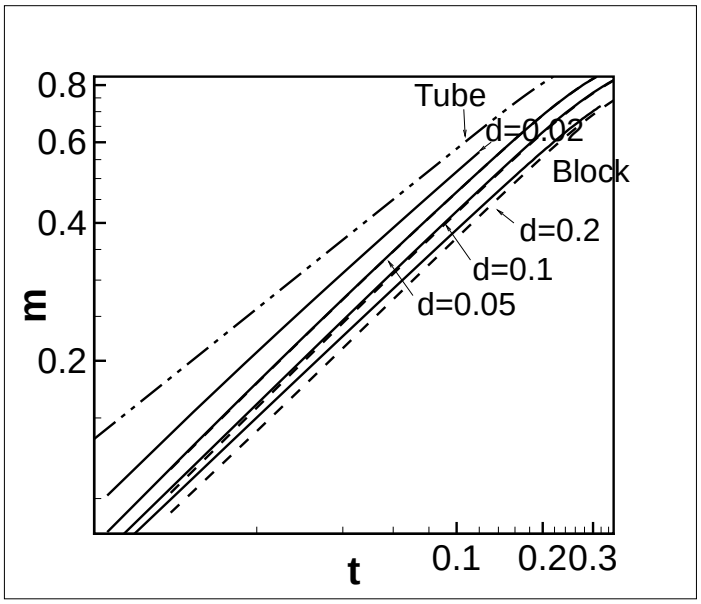

Fig. 4.8 The mass of the solvent that penetrates into the tube as a function of time in logarithmical scale. The dash-dot-dot line depicts the results for the single tube, the dashed lines show the data obtained for the block geometry without convection, and the solid lines with convection. The data for the block geometry is obtained for different tube diameters as depicted in the figure. The data for cases with hydrodynamic flows were obtained for $Re = 10^{-4}$ and $Gr = 10^{9}$.

the solute from the tube ends transporting it either to the top or bottom of the containers (depending on the density difference between liquids). Nevertheless, it is difficult to position the solute/solvent boundary as it remains too diffusive.

The rate of diffusion calculated from the model with two side-added blocks is depicted in Fig.4.8. It can be seen that the process of the mass transport occurs slower and the time-dependencies is different from the expectations from the single capillary tube model. The new time dependence is closer to $t^{0.6}$ (in Fig.4.8). Such a difference, as compared with the single tube results, could be explained by the accumulation of the solute near the tube ends, blocking the access of the fresh solvent.

The results from the experimental work [2] also show that the rate of dissolution is proportional to the square of the tube's diameter. From the numerical simulations, we only observed the weak dependence on the tube diameter in the results for the block geometry. It seems that the bigger tubes mean higher solute concentrations accumulating near the tube's ends, and thus have a stronger effect in reducing the rate of solvent penetration into the tube. This can be seen in figure 4.8, where the dissolution from smaller tubes happens faster. This, in particular, can be seen for the curve obtained for the tube with $d = 0.2$.

The effect of convection was found to be very small for smaller tubes, making the curves

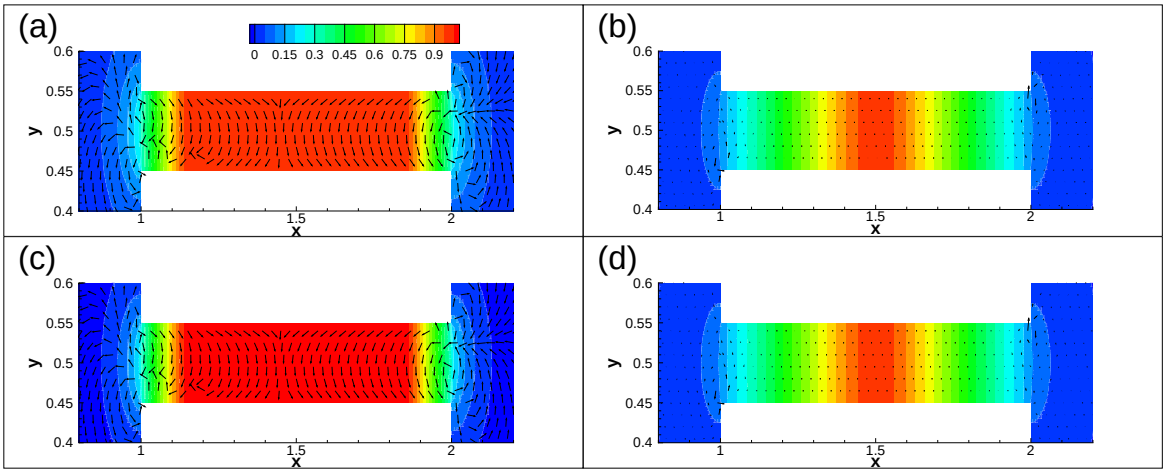

Fig. 4.9 The snapshots of the concentration field and vector field for the Fickian diffusion with the Korteweg force. (a) $Ca = 10^{-4}$ and $t = 10^4$; (b) $Ca = 10^{-4}$ and $t = 10^5$; (c) $Ca = 4 \times 10^{-4}$ and $t = 10^4$; (d) $Ca = 4 \times 10^{-4}$ $t = 10^5$. Other parameters used for these calculation are same, $Re = 10^{-4}$ and $Gr = 10^9$.

indistinguishable from those obtained from the purely diffusive calculations with $Gr = 0$. The results for higher Grashof numbers when the convective effect may be important were impossible to obtain with the current model, as then the concentration levels turn out to be non-physical. The limiting curve for a tube of very small diameter seems to be given by the calculations for the single tube, which also gives wrong time dependence for the propagation of the solvent/solute interface.

The Korteweg force

We also studied the effect the Korteweg force (surface tension) on the classical Fickian diffusion. Fig.4.9 shows the concentration fields for the obtained cases. Even with the Korteweg term, the experimental observations of the distinguishable interfaces cannot be reproduced. The hydrodynamic flows at the interface can be observed (see Fig.4.9). The observed profile of the hydrodynamic flows and the concentration field is still similar to the observations in Fickian diffusion. The liquid/liquid boundaries constantly stay at the sides of the tube and slowly smear (see Fig.4.9), which has no significant difference as compared with the features of the classical Fickian diffusion. This is predictable because the kinetics of diffusion is still determined by the classical Fick's law.

The strength of surface tension is determined by the Ca number and the typical value of this parameter is 10^{-4} [60]. The simulations are done under $Ca = 10^{-4}$ and $Ca = 4 \times 10^{-4}$ and the results are similar (In Fig.4.9).

Even with the Korteweg term, the accurate description of the shape of the interface was

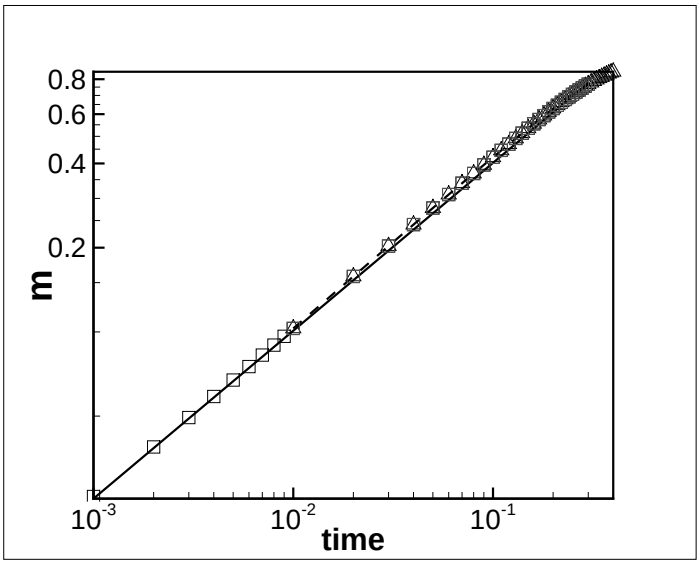

Fig. 4.10 The mass of solvent that enters into the tube as a function of time.

still not obtained. It is expected that this may change the rate of mass transfer. In Fig.4.10, a comparison is made with the previous Fickian diffusion case. The curves almost coincide and this means the hydrodynamic flows are still weak to affect the mass transfer due to diffusion. The comparison is also made between $Ca = 10^{-4}$ and $Ca = 4 \times 10^{-4}$ and almost no differences is observed.

4.2.3 3D model

In the previous sections, the simulations have been carried for one-dimensional and two-dimensional geometries. In 2D model, with the geometry of the added blocks, the rate of mass transfer of solvent was found to be different from the results of one-dimensional model. It is interesting to extend the model to a three-dimensional case to check whether the result would be different again. As it has been mentioned in Chapter 3, the CFD software ANSYS Fluent was used for these calculations.

Results of the 3D simulations

The simulations were conducted with both single capillary tube model (in Fig.3.1) and the model with two side-added blocks (in Fig.3.2). We start the simulation in 2D model and then 3D model. Firstly, the simulation was conducted without gravity ($Gr = 0$). The snapshots in Fig.4.11 show the concentration field of the obtained case. As expected, the diffusive zone is observed to be similar to the previous Fickian simulation. This is because the diffusion is still described by the classical Fick's law in the Fluent solver.

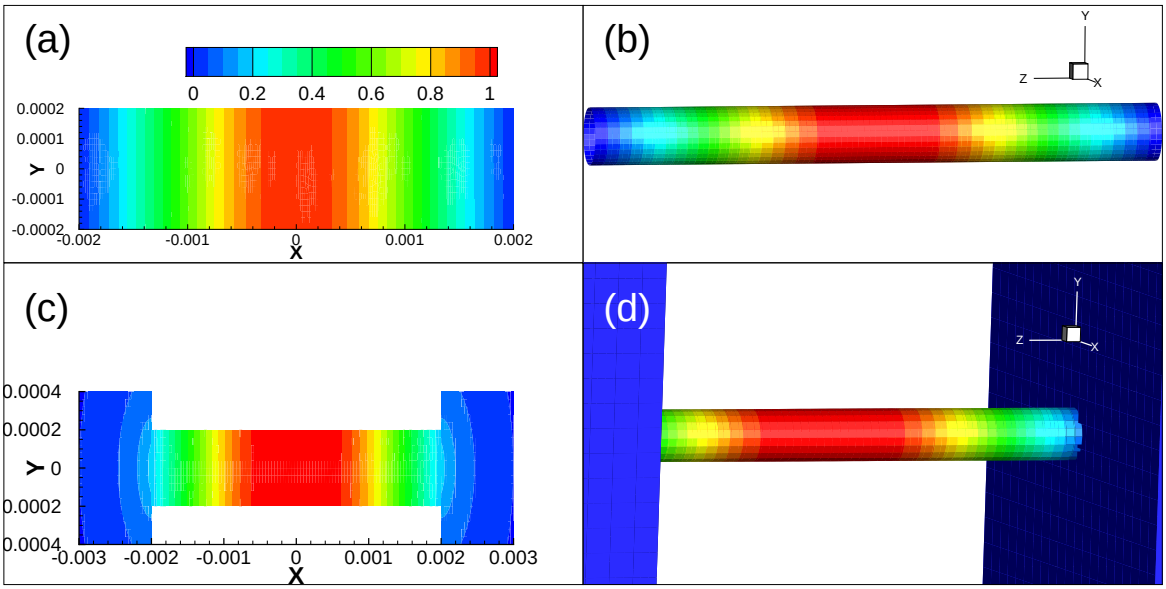

Fig. 4.11 The snapshot of the concentration field at 6000s (the gravity is neglected).

The mass transfer of the solvent phase is also plotted as a function of time. The axis of time is re-scaled by using the diffusive time scale $\tau = \frac{L^2}{D_0}$ (here L is the tube's length and $D_0 = 1.6 \times 10^{-10} \frac{m^2}{s}$ is the classical value of the diffusivity). The comparison between 2D and 3D results has already been shown in the last chapter (Fig.3.7). In the single tube model, the 2D and 3D data coincide and the rate of transfer is about 0.5 time-dependence. In the block model, for both 2D and 3D data, the dissolution rate is around 0.6 time-dependence.

Fig.4.12 compares the obtained data with the previous simulations. Since the governing equation in both model are same, a comparison can be used to validate the obtained data. Despite a small difference that may be caused by round-off errors, it can be concluded that both methods give very similar predictions.

The role of the hydrodynamic flows in dissolution

In previous sections, the simulations for the parameters that would be sufficiently close to the conditions of the experiment [2] were not possible, because the non-physical values (below 0 (which corresponds to a pure solvent) and above 1 (a pure solute)) appeared in the concentration field. As it has been discussed in Chapter 3, the viscosity coefficient in software Fluent is defined as a function of concentration, and thus an advantage of a very large viscosity of the glycerine phase can be used. The viscosity of water is $0.001 \frac{kg}{ms}$ and the viscosity of glycerine is $0.799 \frac{kg}{ms}$. With help of the software Fluent, it is possible to run the simulations for the Grashoff numbers that would correspond to the normal gravity

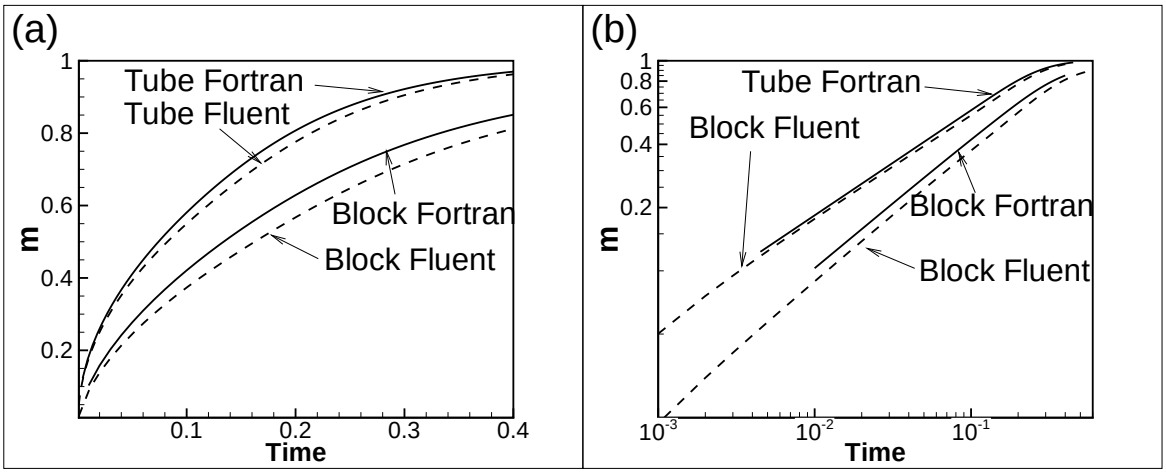

Fig. 4.12 The mass of solvent penetrating into the tube evaluated from the Fluent solver. (a) The mass of solvent penetrating into the tube as a function of time in normal scale; (b) The mass of solvent penetrating into the tube as a function of time in logarithmic scale. The solid lines are for results calculated from Fotran codes and the dashed lines are for results calculated from Fluent solver.

acceleration, i.e. $9.8\frac{m}{s^2}$.

Fig.4.13 shows the snapshots of the concentration field during the dissolution. The diffusive solvent/solute boundaries were observed to be inclined under the effect of the gravity. Dissolution occurred faster compared with the case without gravity (In Fig.4.14) and the time dependence of the rate of mass transfer was recorded to be about 0.4.

At the very early stage of the process (around $1000s$), it is found that the solute is being displaced by solvent from only the top part of tube (in Fig.4.13 and Fig.4.15). Such behaviour is similar to the pattern of the half-depth flow pointing to the fluid with lower density from a corner of a tube [3, 135]. A direct look of the pattern of the lock-exchange flow within a horizontal tube (which is closed to our configurations) can be seen in Fig.4.16. Such flows are driven by gravity and they are observed in any two fluids system with the strong density difference. However, in our simulations, this phenomenon was only observed for about $1000s$, which is relatively short compared with prolong duration of the process. After $1000s$, the diffusive layers are well established and it attaches to both upper and lower tube wall (see Fig.4.15). Such behaviour is obviously different from Fig.4.16 and is just similar to the previous simulations produced by the FORTRAN code based on Eq.2.5. Thus, the process is dominated by diffusion rather than the gravity-driven flows.

Then the simulation was repeated in the larger geometries. The length of the tube was increased to 5cm. The smaller diameters (to 0.2mm) were also examined. Such settings are considered to be more relevant to the experiment configuration. The obtained results are

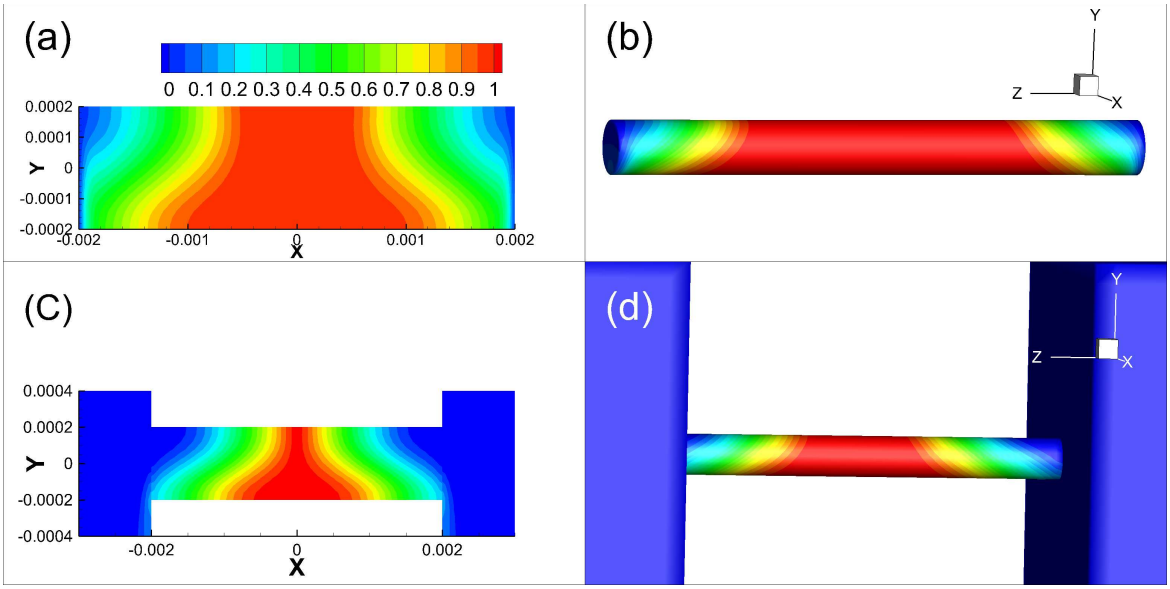

Fig. 4.13 The snapshot of the concentration field for the dissolution under normal gravity ($t = 1000s$).

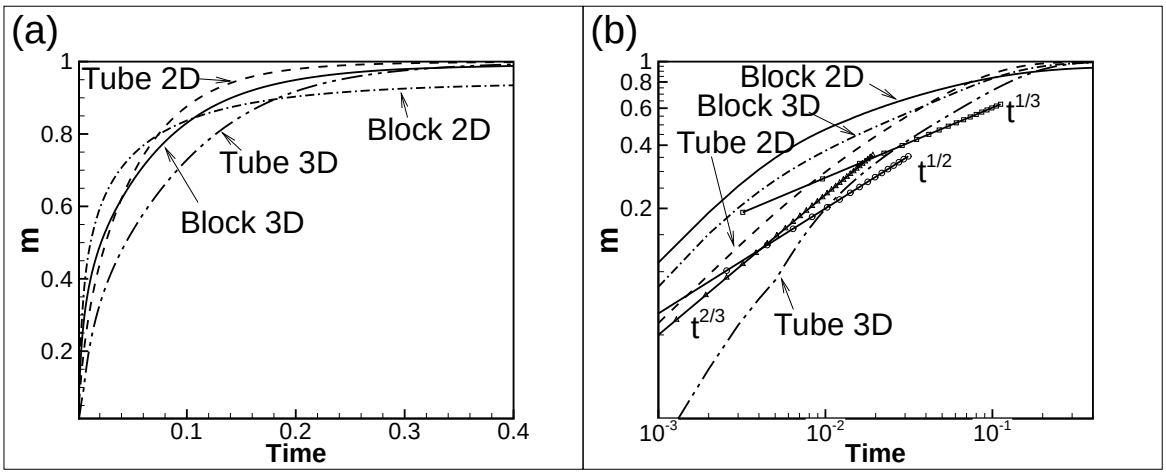

Fig. 4.14 The evaluation of the mass transfer under gravity. (a) The mass of solvent penetrating into the tube as a function of time in normal scale; (b) The mass of solvent penetrating into the tube as a function of time in logarithmic scale. In both (a) and (b), dashed line is for 2D tube, dash-dot-dot line is for 3D tube, solid line is for 2D block, dash-dot line is for 3D. In (b), three reference lines are added to identify the time dependencies and their information are as follows: the solid line with square symbols is for $m \propto t^{1/3}$, the solid line with delta symbols is for $m \propto t^{2/3}$, the solid line with circle symbols is for $m \propto t^{1/2}$.

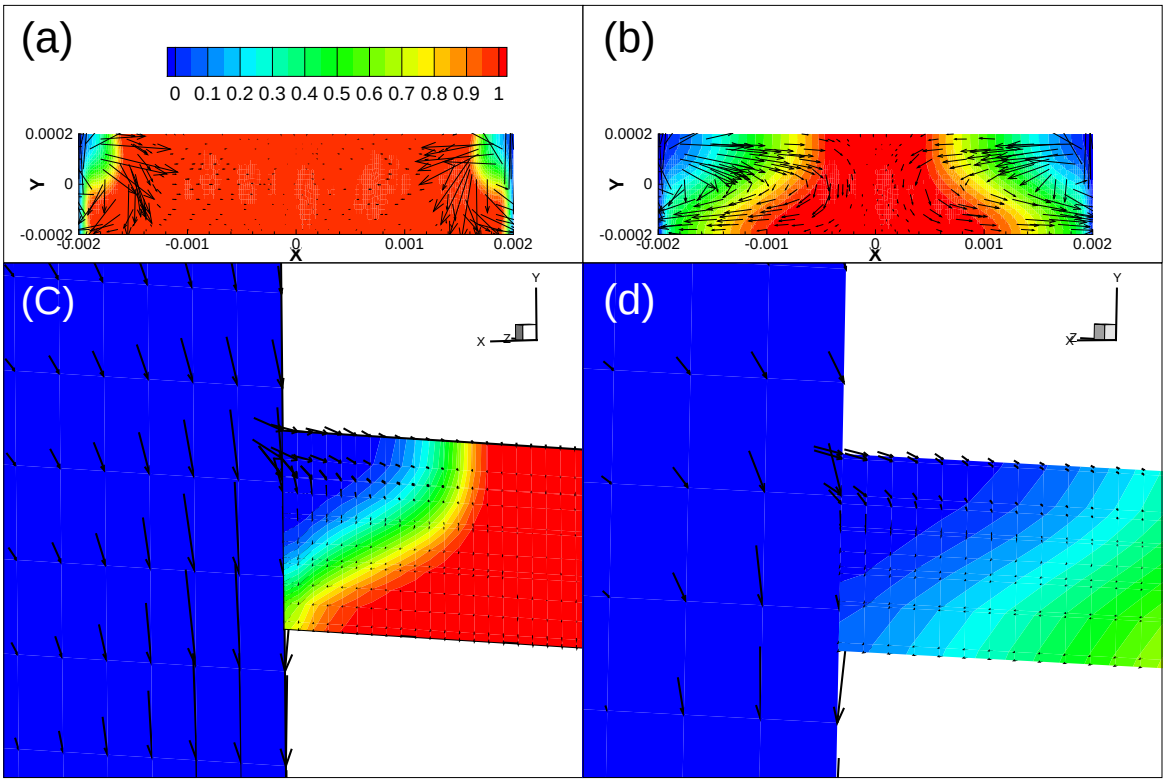

Fig. 4.15 The snapshot of the concentration and velocity fields at the initial ((a) and (c), $t = 100s$) and later ((c) and (d), $t = 1000s$) time movements ($g = 9.8\frac{m}{s^2}$). The initial fields are similar to the profile of the lock-exchange flow.

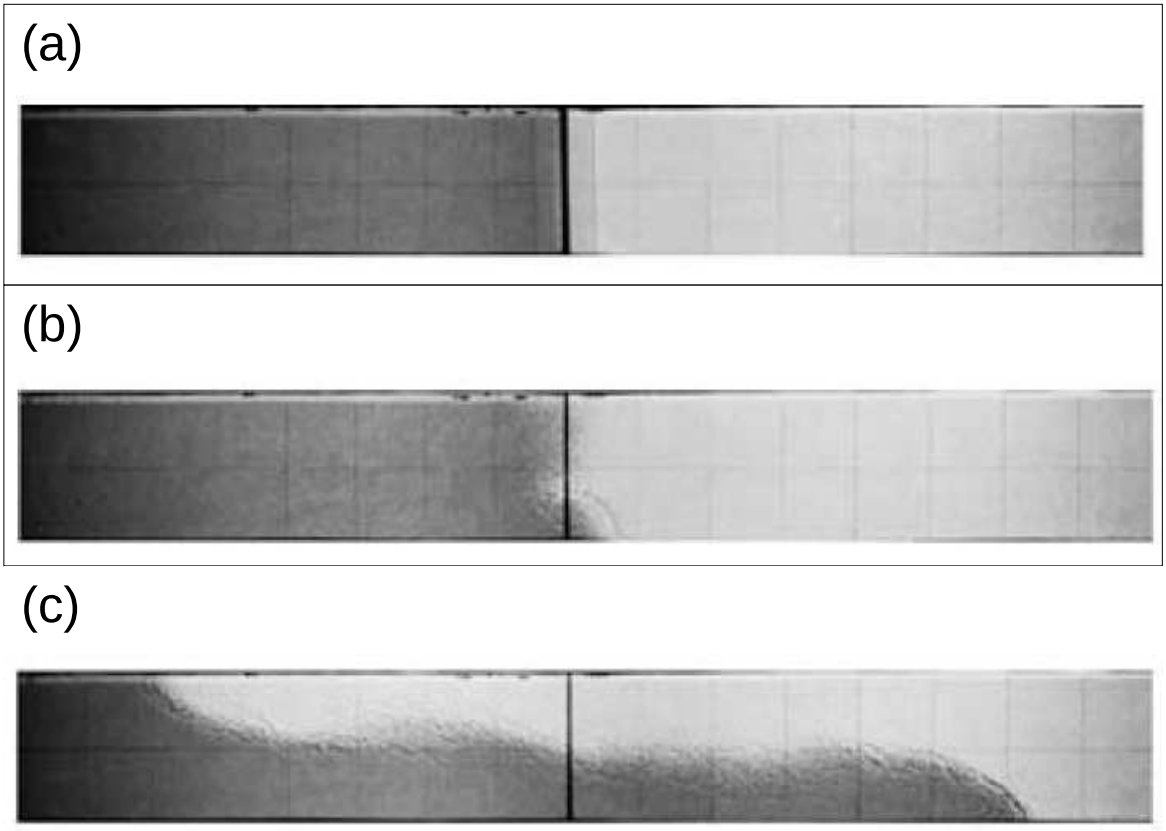

Fig. 4.16 The snapshots of the pattern of the lock-exchange flow reported in paper [3]. (a) the initial state; (b) the onset of the lock-exchange flow; (c) the pattern of lock-exchange flow at longer time period.

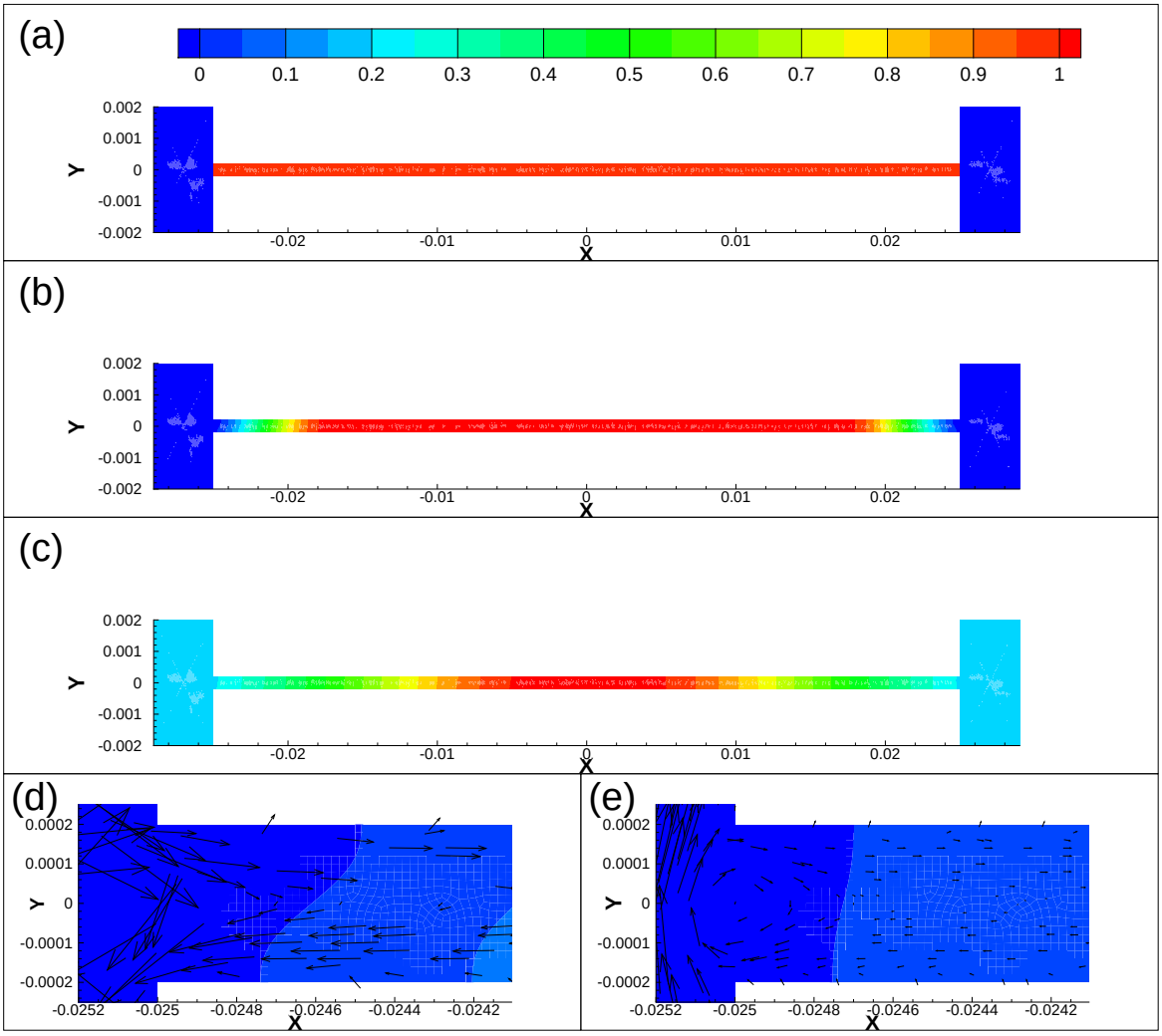

Fig. 4.17 Dissolution in a 5 cm tube (normal gravity).(a) $t = 0s$, (b) $t = 10^5 s$, (c) $t = 10^6 s$, (d) $t = 10^5 s$ and (e) $t = 10^6 s$.

shown in Fig.4.17. It can be observed that the diffusive zone becomes less inclined. Fig.4.18 shows the curve of mass transfer as a function of time. The time dependence of the curve is near 0.4. In the tube with smaller diameter (0.2mm), the dissolution occurs slower and the rate of mass transfer changes to the dependencies with indexes of about $0.4 - 0.45$.

As a consequence, it could be concluded that the gravity has a strong effect on the dissolution process. The correct shape of the experimentally observed liquid/liquid interface [2] is not reproduced. During the simulation, the feature of the lock-exchange flow is observed at the beginning of the process. However, this phenomenon only lasts for a very short period and then change back to the similar images of the interfaces driven by the Fickian diffusion. The experimental relationship between dissolution rate and tube diameter reported in the

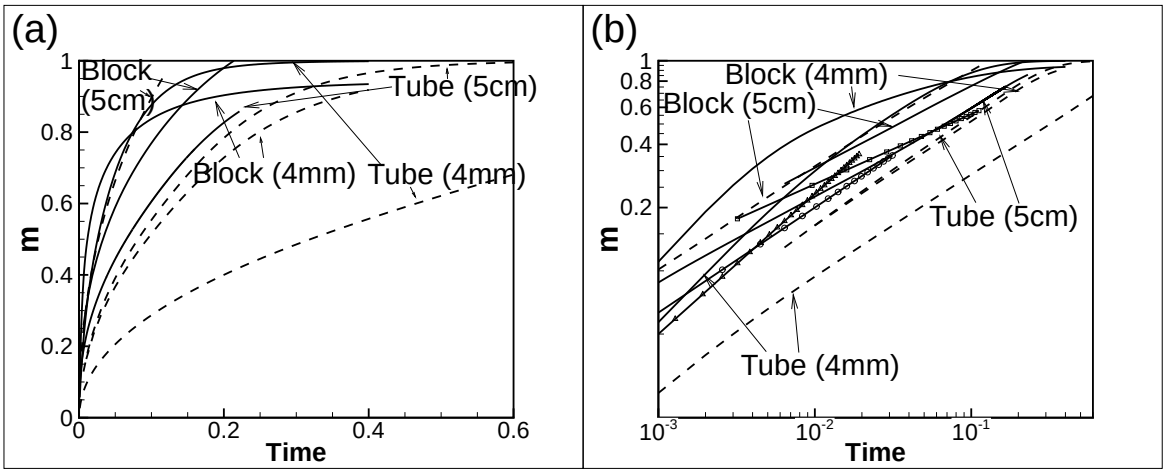

Fig. 4.18 The mass of solvent penetrating into the tube as a function of time. (a) The mass of solvent penetrating into the tube as a function of time in normal scale; (b) The mass of solvent penetrating into the tube as a function of time in logarithmic scale. In both (a) and (b), solid lines are for tube diameter equals to 0.4mm, dashed lines are for tube diameter equals to 0.2mm. In (b), three reference lines are added to help identifying the time dependencies and their information are as follows: the solid line with square symbols is $m \propto t^{1/3}$, the solid line with delta symbols is $m \propto t^{2/3}$, the solid line with circle symbols is $m \propto t^{1/2}$.

paper [2] is also not obtained. In cases with the smaller tube diameter (d=0.2mm), the time dependence of the dissolution rate is closer to 0.5, and this changes for the tube of larger diameters. Furthermore, the dissolution simulated above takes about 10^3 times longer than in experiments. This also proves that the dissolution in liquid/liquid mixtures cannot be explained by the classical Fick's law.

4.3 Non-Fickian diffusion in polymers

The diffusion in polymers is usually non-Fickian with the time dependencies that are frequently similar to the experimental observations that we were modelling. There are a few numerical works that develop the models for the mathematical description of the diffusion in polymer systems. We did not have the aim to study the dissolution in polymers, we merely wanted to apply the known models [128–130] to the configuration that we are interested, with a hope to reproduce the needed time dependencies. Although, we found that all models developed for polymers are formulated in such a way to describe the propagation of a single polymerization front. The particular feature of our configuration was that there are two solute/solvent fronts at two sides of the tube that are moving towards each other. In this

section, we show that the mathematical models developed for polymers cannot be applied to model the process in our configuration.

We attempt to use the known model of diffusion in polymer published in paper [128] to the binary liquid/liquid mixture. The governing equations (Eq.(2.18) and Eq.(2.19)) have already been introduced in chapter 2 and it both need to be supplemented with the initial condition and boundary condition. In paper [128], the model is built to describe the polymer slab of width L. The settings of the boundary conditions and initial conditions used in paper [128] are written at top of Fig.4.19(a). Fig.4.19(a) shows the obtained result from Cohen's model [128]. The shape of the sharp front agrees with the results in papers [128–130]. To understand the setting of C_0, we change the boundary condition at the left boundary to be $C(0,t) = 0$ (shown at the top of Fig.4.19(b)). The snapshots in the Fig.4.19(b) shows the distribution of concentration field. It is observed similar to Fig.4.19(a), except the position of the sharp front moves closer to the right boundary.

Then we attempt to modify the initial condition and boundary conditions to describe the solvent penetration in the capillary tube (shown at the top of Fig.4.19(c)). The obtained concentration field are shown in Fig.4.19(c). It is observed that there is the phenomenon of the mass uptake with unrealistic value occurred during the diffusion. This mass uptake was considered to have realistic meanings in Refs.[128–130] because the stress gradient may continue driving solvent after the diffusive process. We also exchange the value of solute concentration and solvent concentration (at the top of Fig.4.19(d)). The mass uptake is still observed (in Fig.4.19(d)). Hence, the model is incorrect for the liquid/liquid mixture.

The mass of solvent penetrates into the tube as a function of time is plotted in Fig.(4.20). The mass uptake of solvent into the polymers was observed. The intensity of this mass uptake is affected by parameters, such as, β, D and λ. The relations have been studied and it can be generally concluded that the amount of the mass uptake reduced with β and λ. Through controlling these parameters, the mass uptake can eventually be eliminated but the rate of mass transfer is getting closer to the classical Fickian time-dependence. Thus, we have conclude that we tried a known published model of dissolution in polymers [128] and the straight-forward use of this model will not describe our problems.

4.4 Phase-field approach

In this section, we start to show the result obtained from the phase-field model. Since the phase-field theory is of the fourth order in terms of the concentration field, this makes it impossible to use the commercial software packages (such as ANSYS Fluent), as all these packages assumes that the species transport is determined by the classical equations of the

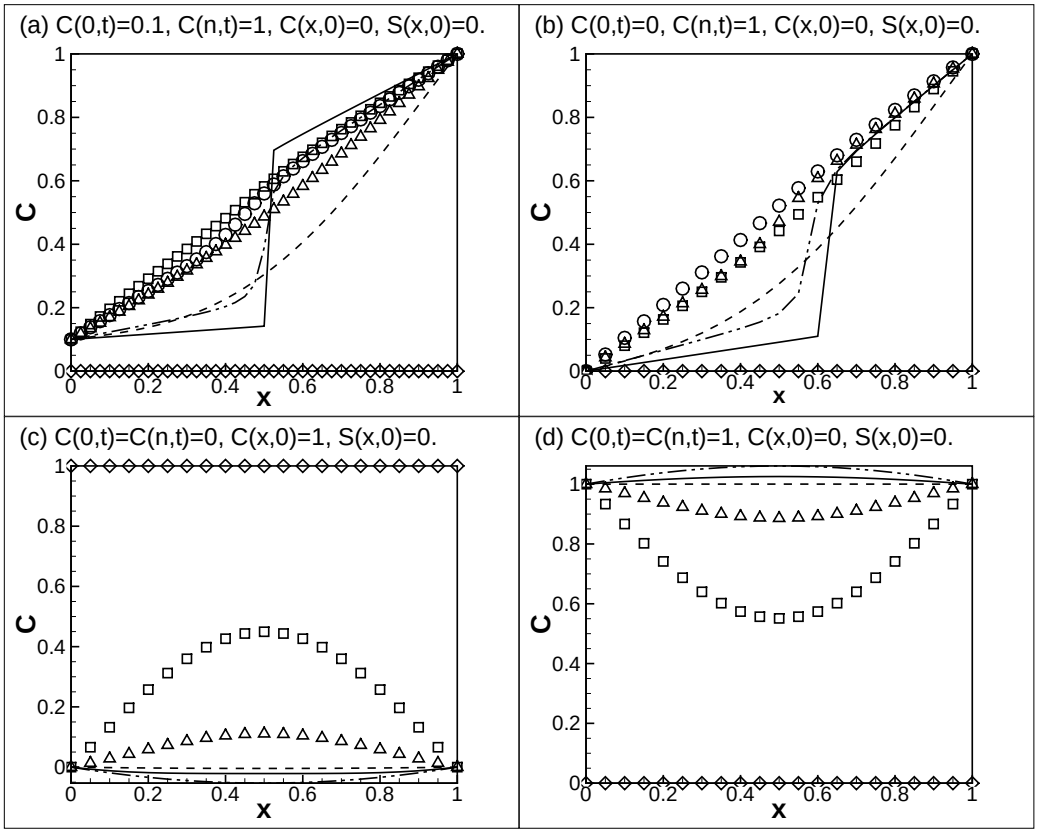

Fig. 4.19 Diffusion in the solvent/polymer mixture. In (a) and (b), $t = 0$, diamond symbols; $t = 0.1$, dashed line; $t = 0.2$, delta symbols; $t = 0.5$, square symbols; $t = 1$, circle symbols; $t = 3$, dash-dot-dot line; $t = 10$, solid line. In (c) and (d), $t = 0$, diamond symbols; $t = 0.1$, square symbols; $t = 0.2$, delta symbols; $t = 0.5$, dash-dot-dot line; $t = 1$, solid line; $t = 3$, dashed line. The settings of the boundary conditions and initial conditions are written at top of each figure. The meaning of C_0 and C_1 are not explained in paper [128]. It seems that C_1 is the value for the glass polymer and C_0 is the value for the penetration

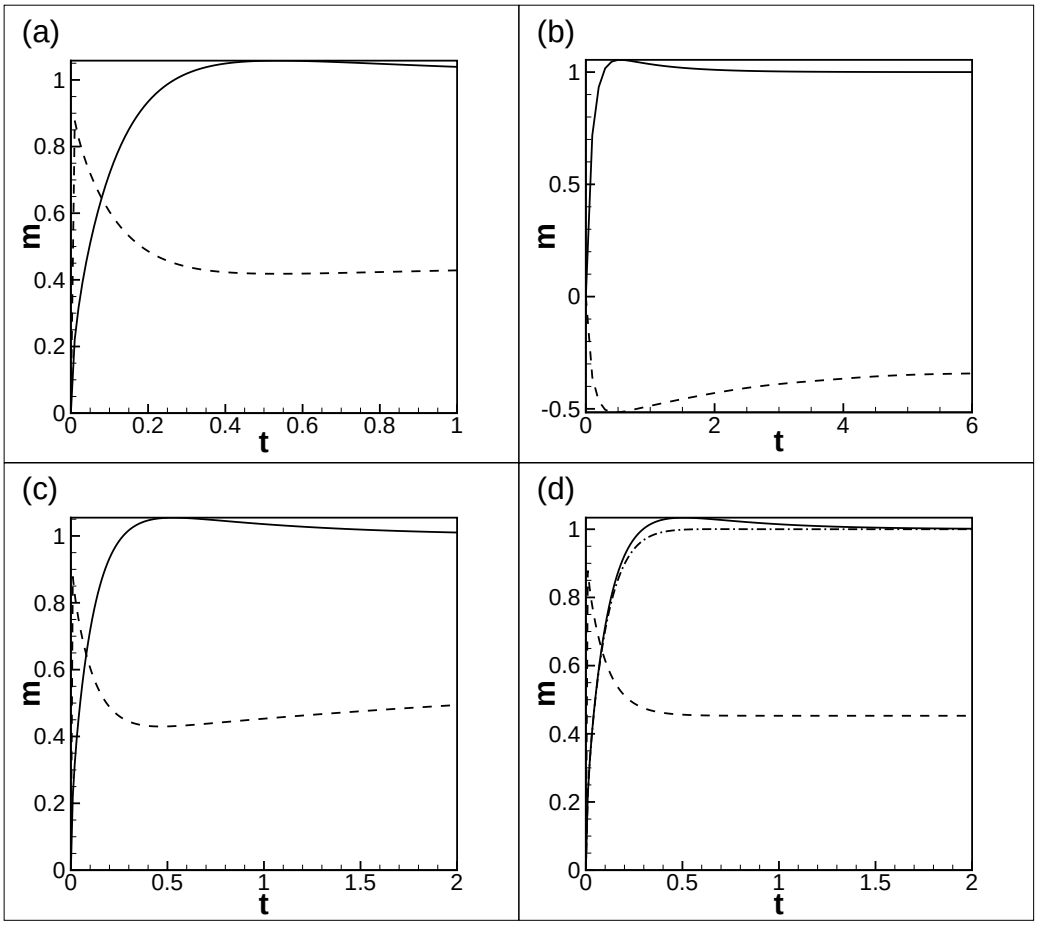

Fig. 4.20 The mass of solvent penetrated into the tube as a function of time. The results from model with both Cohen's boundary conditions [128] and our boundary condition used in 4.19(c) are plotted with dashed lines and solid lines respectively. (a) $\beta = 1$; (b) the solid line and dashed line represent different boundary condition used in Fig.4.19(c) and (d) respectively; (c) $D = 10$; (d)$\lambda = 10$, the dash-dot line is for $\lambda = 100$ with our boundary condition used in Fig.4.19(c).

second order and there are no options to change these settings. Hence the simulation is done by run the computational codes based on the phase-field theory.

4.4.1 Phase-field results

The simulations were conducted in a same sequence as the simulations that were based on the classical Fick's law. The snapshots of the concentration fields obtained within the phase-field approach are depicted in Fig.4.21 and 4.22. The snapshots in Fig.4.21 using the neutral wetting boundary conditions (in Eq.(3.17)), and the snapshots in Fig.(4.22) show the results for the case of the solute-philic walls (Eq.(3.18)). Within the phase-field approach, the solute/solvent interface can be clearly identified. By variation of the parameters (*Ca* and *Gr*), the shape of the interface can be made very similar to the observation in the experiment [2]. In the simulations, the interface was observed to have the same thickness during the entire duration. (e) and (f) in Fig.4.21 and 4.22 show the result obtained under the effect of hydrodynamics and it can be observed that the flow vortices attached to the solute/solvent boundaries are well localized i.e. the flow pattern is very different to the one observed in the Fickian-based results in Fig.4.7. The flow amplitude was found to be weak, and thus these vortices have almost no effect.

The rate of dissolution was also evaluated through the rate of mass transfer. In addition, since the liquid/liquid boundaries are distinguishable within the phase-field approach, it was possible to track the position of the interface to provide an alternative way for the evaluation of the rate of diffusion. The later method was used in the experimental observations [2]. The results are depicted in Fig.4.25. In both methods, the time dependencies of the rate of the dissolution were found to be similar. In single tube model, the rate of dissolution still follows the 0.5 time dependence. In the model with added blocks, the solvent penetration occurred slower, with the time dependence closer to $t^{0.6}$ for the most of the time and being only different during the initial stages. This is similar to the results of the Fickian model.

The average concentration of each phase was also recorded. In chapter 2, it has been discussed the average concentration of the mixture changes with A and the value of concentration for each phase at the equilibrium state is $C \approx \pm 0.388$ when $A = -0.5$. This is confirmed by the obtained results (in Fig.4.24). The average concentration in the solvent phase is obviously smaller. This is because the amount of solvent in blocks is much higher than the amount of solute in the capillary tube.

In Fig.2.2, it shows that the values of average concentration should change with the parameter A. The simulations were repeated for different value of the parameter A and the results are depicted in Fig.4.24(a). It can be seen that the average concentration in the solute phase varied when A increased. When $A = -0.5$, a very short period of the initial quench

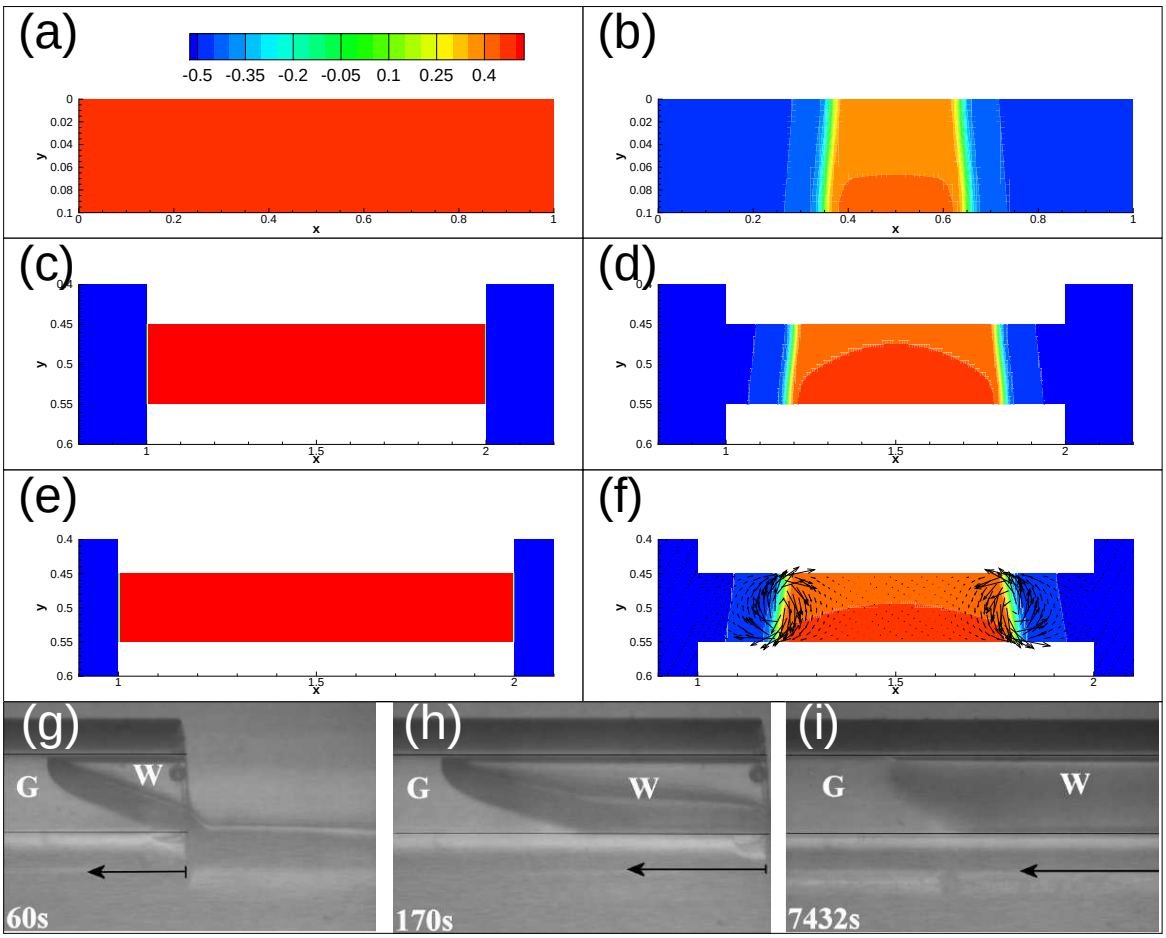

Fig. 4.21 The evolution of the solute/solvent mixture modeled by the phase-field approach. The results are obtained for the rigid wall boundary conditions for the tube walls. (a,c,e) show the snapshots of the concentration and velocity fields at initial condition $t = 0$ and (b,d,f) show the results at $t = 0.03$. The results are shown for the single tube (a,b), for the block geometry without hydrodynamics (c,d); and for the block geometry taking into account the hydrodynamic flows (e,f). The parameters used for above cases are $A = -0.5$, $Ca = 10^{-4}$, $Gr = 1$. For (e,f), the additional parameters are $Pe = 10^4$, and $Re = 100$. (g,h,i) are the snapshots of the experiment observations of the glycerol/water interface reported in paper [2] ('G' represents the glycerol phase and 'W' represents the water phase).

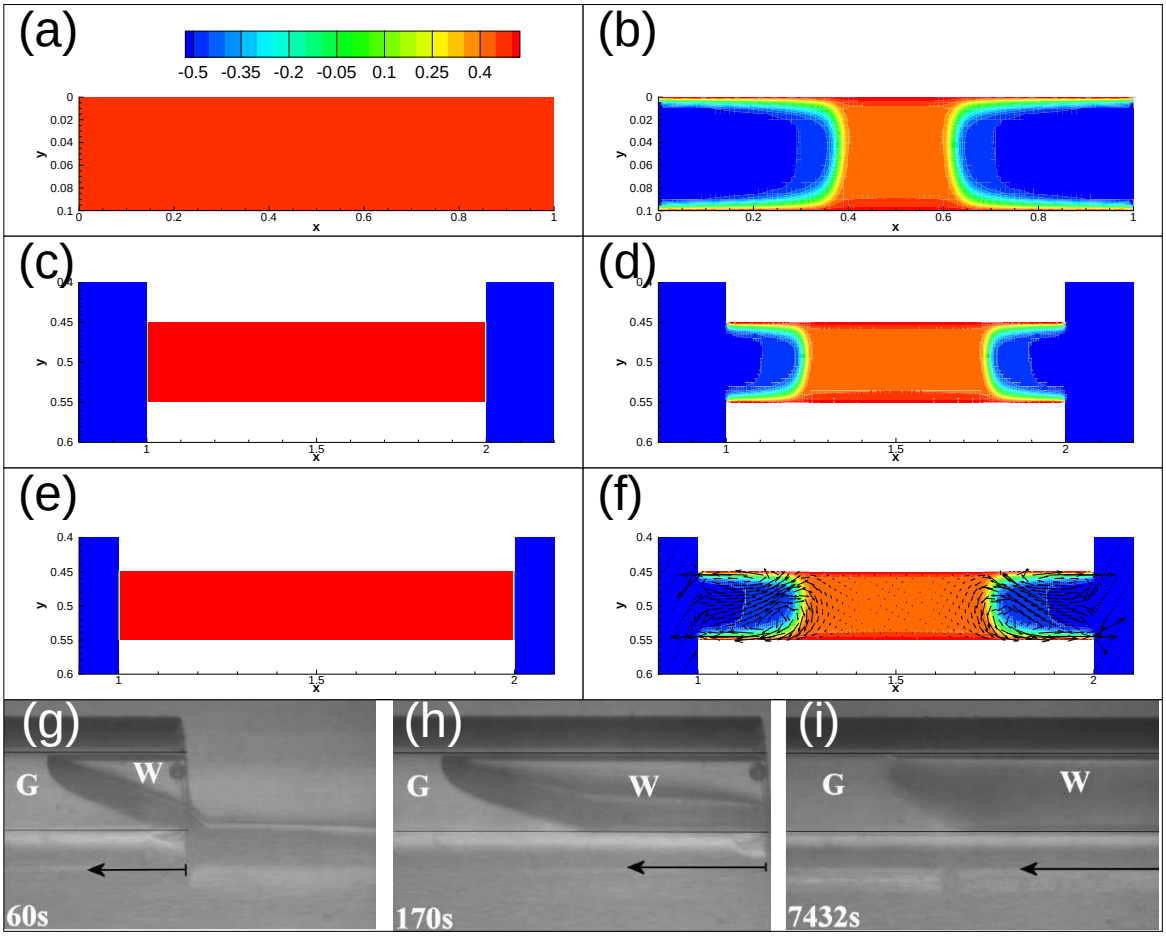

Fig. 4.22 The evolution of the solute/solvent mixture modeled by the phase-field approach. The results are obtained for the solute-philic boundary conditions for the tube walls. (a,c,e) show the snapshots of the concentration and velocity fields at initial condition $t = 0$ and (b,d,f) show the results at $t = 0.03$. The results are shown for the single tube (a,b), for the block geometry without hydrodynamics (c,d); and for the block geometry taking into account the hydrodynamic flows (e,f). The parameters used for above cases are $A = -0.5$, $Ca = 10^{-4}$, $Gr = 1$. For (e,f), the additional parameters are $Pe = 10^4$, and $Re = 100$. (g,h,i) are the snapshots of the experiment observations of the glycerol/water interface reported in paper [2] ('G' represents the glycerol phase and 'W' represents the water phase).

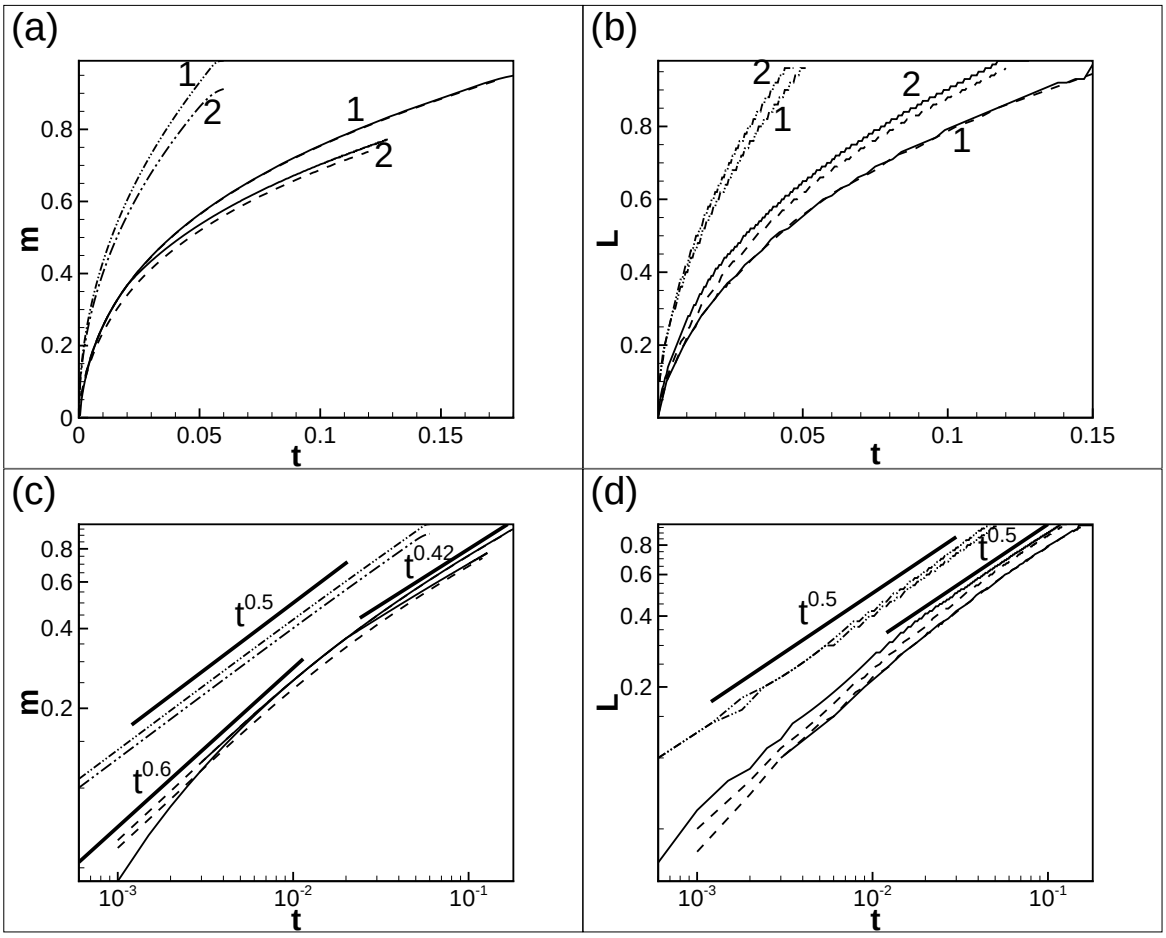

Fig. 4.23 The mass transfer evaluated in the phase-field model (a) The mass of the solvent penetrating into the tube as a function of time. (b) The position of the liquid/liquid interface as a function of time. The mark "1" and "2"correspond to the results obtained for the tubes with walls neutral to both liquids and the results with the solute-philic tube wall, respectively. The results are plotted for $d = 0.1$, $A = -0.5$, $Ca = 10^{-4}$, $Gr = 1$, $Pe = 10^4$, and $Re = 100$ (the curves obtained for the cases with the included effects of hydrodynamics). The dash–dot–dot lines depict the results for the single tubes; the dashed lines for the block geometry without hydrodynamics; and the solid lines for the block geometry with hydrodynamics. (c) and (d) show the same results but in logarithmic coordinates. The thicker solid lines show the reference dependencies.

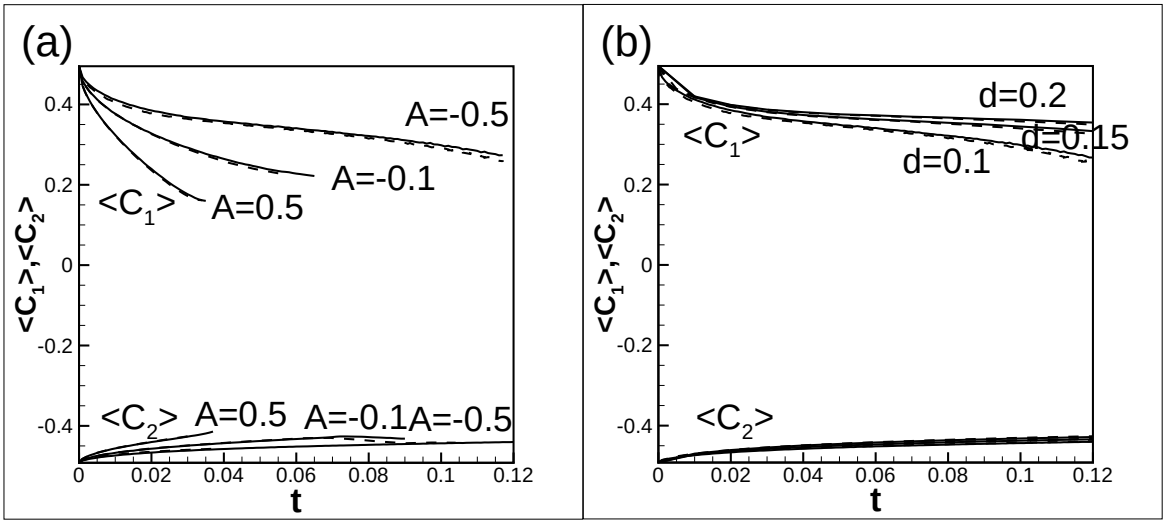

Fig. 4.24 The average concentrations within the solute ($< C_1 >$) and solvent ($< C_2 >$) phases as a function of the time. The data is obtained from the block geometry calculations for $Gr = 1$, $Ca = 10^{-4}$, $Pe = 10^4$ and (a) $A = -0.5$ and three different diameters of the tube (0.1, 0.15, and 0.2); (b) $d = 0.1$ and three different A (0.5, 0.1, and 0.5). In both figures, the dashed lines correspond to the results without the effect of hydrodynamics and the solid lines are for the results with the hydrodynamics.

is observed. In Fig.4.24(b), the results under different tube's diameter are shown and that initial period of the quench always exists. Such a behaviour is also reported in experimental work [66].

4.4.2 The parameter study of the phase-field model

The typical values of the parameters used in the phase-field approach are determined through the comparison of the experimental observations and the numerical results. Because this work aims to reproduce the observations in paper [2], it is natural to make a comparison with paper [2]. The main criterion of the comparison is the shape of the solvent/solute boundary (interface). In figures.4.21 and 4.22, the comparisons show that the distinguishable solvent/solute boundaries can be obtained under the $A = -0.5$, $Ca = 10^{-4}$, $Gr = 1$. For the cases induced by gravity-driven flow, the condition of weak flows are obtained with the additional settings of $Pe = 10^4$ and $Re = 100$. However, the apparent contact angle[6] of the interface is rather perpendicular to the horizontal axis. Thus, it is necessary to determine the typical values of the parameters that produce the contact angle of the solvent/solute boundaries observed in the experiment [2].

[6]The interface is inclined but the exact contact angle will remain 90 degrees (the neutral tube wall) or 180 degrees (solute-philic tube wall) due to our settings of boundary condition. Hence, we name it as the apparent

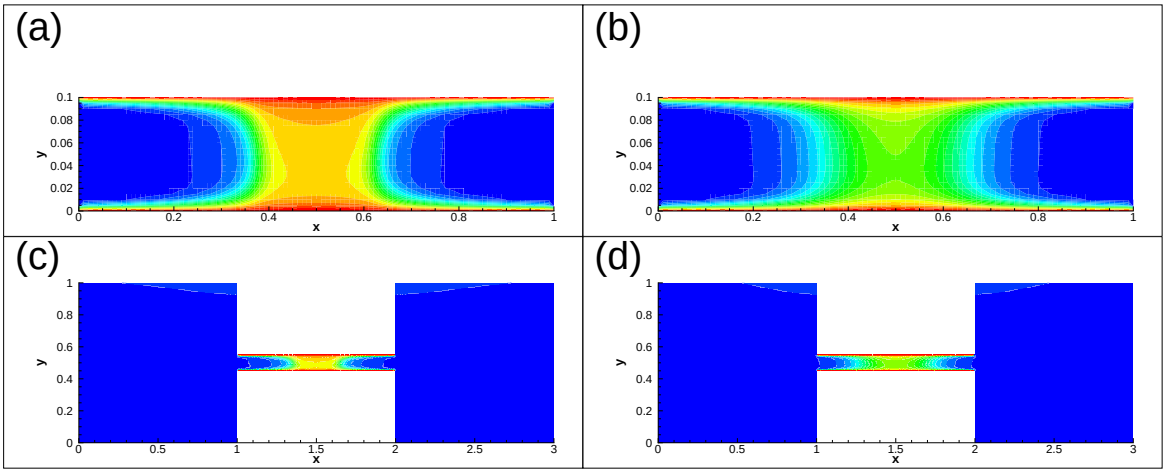

Fig. 4.25 The snapshots of the concentration fields for (a) $A = -0.1$, $Ca = 10^{-4}$, $Gr = 1$, and $t = 2.4^{-2}$ and (b) $A = 0.5$, $Ca = 10^{-4}$, $Gr = 1$, and $t = 2 \times 10^{-2}$ (c) $A = -0.1$, $Ca = 10^{-4}$, $Gr = 1$, $Re = 10^2$, $Pe = 10^4$ and $t = 6.24 \times 10^{-2}$, (d) $A = -0.1$, $Ca = 10^{-4}$, $Gr = 1$, $Re = 10^2$, $Pe = 10^4$ and $t = 3 \times 10^{-2}$.

We need to find out one set of phase-field parameters that can produce the correct apparent contact angle of the interface. In the experiment [2], the contact angle of the interface (to the lower plate of the tube) is about $20 - 30^\circ$. The shape of the interface is under the balance between gravity and the surface tension. In the phase-field model, these two factors are determined by the phase-field parameters Gr and Ca. Thus, the comparison is to find out the appropriate value of Gr and Ca for the numerical simulations. Ca also determines the thickness of the interface. For convenience, we keep $A = -0.5$ and $Ca = 10^{-4}$ and adjust Gr up to 10. In Fig.4.26, it is shown that the obtained apparent contact angles (to the lower plate of the tube) are about 60° ($Gr = 2$) and 30° ($Gr = 10$). This means the obtained shape of interface is a good representation of the experimental observations [2]. Since it is known that $Gr = 10$ and $Ca = 10^{-4}$ is a set of good values to reproduce the experimental observations [2], it is possible to estimate the chemical potential differences between two phases and the value of the capillary constant. If we take the diffusion experiment of the glycerol/water mixture in a 5cm horizontal capillary tube (conducted in paper [2]) as an example, the difference in the chemical potential between the glycerol phase and the water phase is about $10^{-1}\frac{m^2}{s^2}$ and the corresponding value of the capillary constant ε is approximately $10^{-8}\frac{m^4}{s^2}$. It should be noticed that the observed interface in paper [2] is extremely thin. This means the value of Ca number can be made smaller and the related value of the capillary constant ε should also be smaller.

However, the calculations under $Gr = 10$ are made for the single capillary tube. In the

contact angle.

model with two side-added solvent-filled blocks, we could only obtained the result within $Gr = 4$ due to the computational limitation, but it can be expected the experimental observations of the interfaces can be obtained within the phase-field model. In the subsequent section, we would discuss the effect of the above phase-field parameter to the dissolution.

The thickness and shape of the interface

In chapter 2, it was discussed that the interfacial properties at the liquid/liquid boundaries are determined by the capillary number Ca and the parameter A. Firstly, we studied how the thickness of the interface depends on these parameters. For a flat interface without gravity, the thickness of an interface at the equilibrium state is $\delta = \sqrt{-Ca/A}$ (which is valid for the negative values of parameter A). If A is positive, the interface occurs faster. The thickness of the interface is increased with A and the images are as diffusive as the Fickian results when A is positive (in Fig.1.4). The speed of the dissolution is also found to be much faster for higher values of A (In Fig.4.27).

The effect of Ca on the thickness of the interface is shown in Fig.4.28 and Fig.4.29. Fig.4.28 shows the result for the cases when the liquids are neutral to the tube's wall and Fig.4.29 shows the results for the cases of the solute-philic tube walls. In each figure, three groups of data for $Ca = 2.5 \times 10^{-5}$, $Ca = 10^{-4}$ and $Ca = 4 \times 10^{-4}$ are shown. It is easy to see that the interface becomes thinner when Ca is smaller.

Next, the effect on the shape of the interface was studied. It is known that the shape of the interface is determined by the balance between the surface tension and gravity. The effect of gravity is determined by the Grashof number, and the surface tension is determined by Ca. For convenience, we set the value of the parameter A as $A = -0.5$. From the discussion in chapter 2, it is known that the surface tension is proportional to $\sqrt{Ca}$.

Fig.4.28 and Fig.4.29 show three groups of data for $Ca = 2.5 \times 10^{-5}$, $Ca = 10^{-4}$ and $Ca = 4 \times 10^{-4}$ and two group of data for $Gr = 1$ and $Gr = 10$. Fig.4.28 shows the result obtained for the walls with neutral condition and Fig.4.29 shows the results for the solute-philic tube walls. In both models, the shape of the interface becomes more inclined when Gr and Ca are increased. In the results for the solute-philic tube walls, the shape of the interface is found to be closer to the experimental observation.

Fig.4.30 illustrates the effect of Ca on the rate of dissolution. The real interface should be of zero thickness for the macroscopic approach that is developed in the current work. Thus the limit of the small capillary numbers (when the interface thickness becomes smaller) is important to produce more realistic behaviour. In Fig.4.30, one sees that all curves converge if Ca tends to 0.

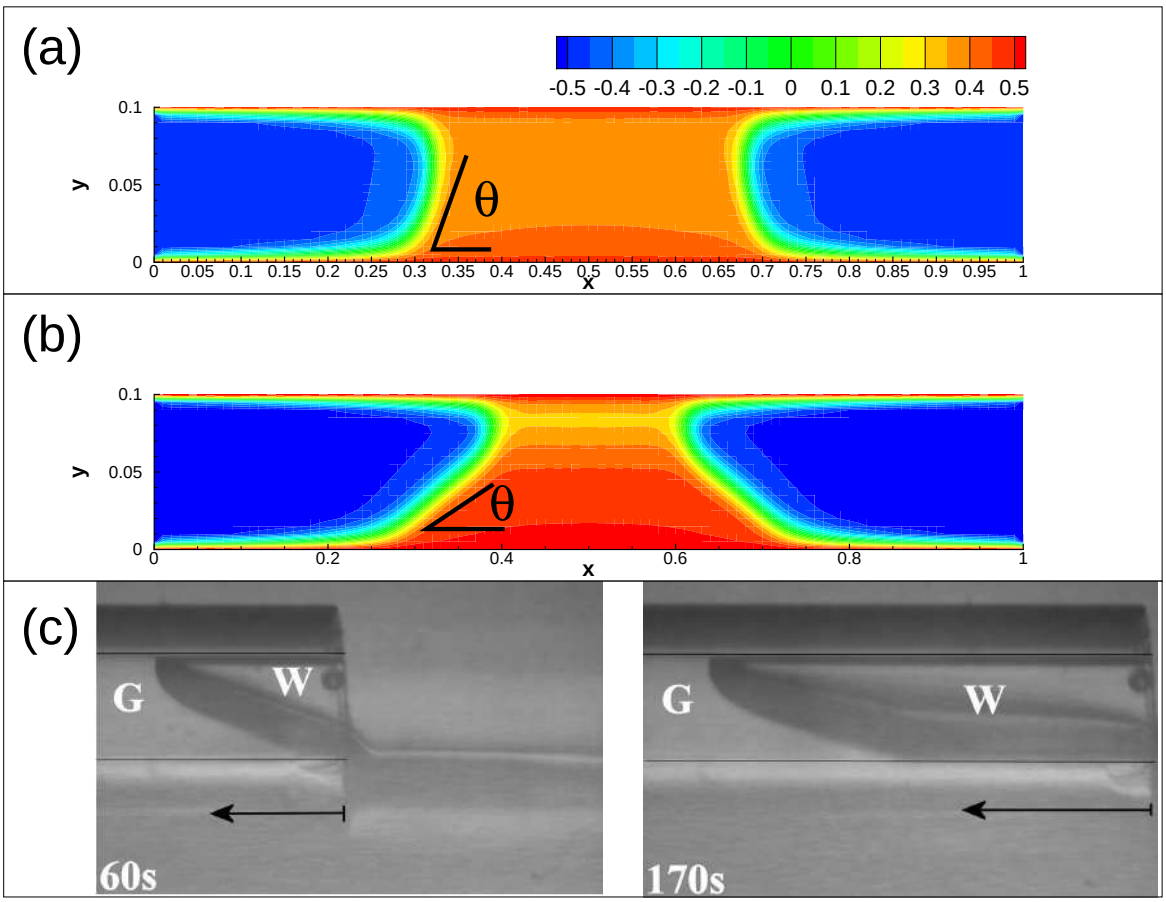

Fig. 4.26 The comparison between experimental and computational results ($A = -0.5$ and $Ca = 10^{-4}$). (a) shows the snapshot of the solvent/solute boundaries at $t = 0.02$ for case of $Gr = 2$. (b) shows the snapshot of the solvent/solute boundaries at $t = 0.02$ for case of $Gr = 10$. (c) shows the optical observations of the solvent/solute interfaces. is the apparent contact angle (to the lower tube wall). θ is measured to be 60° in (a) and 30° in (b). In (a) and (b) the x- and y-axes are shown in different scales, as otherwise either the length of tube does not fit the page, or the tube becomes to narrow, so the interfaces are hardly seen. As a result the visible wetting angles differ from 30° and 60°, but these angles are 30° and 60° if the axes are proportionally scaled.

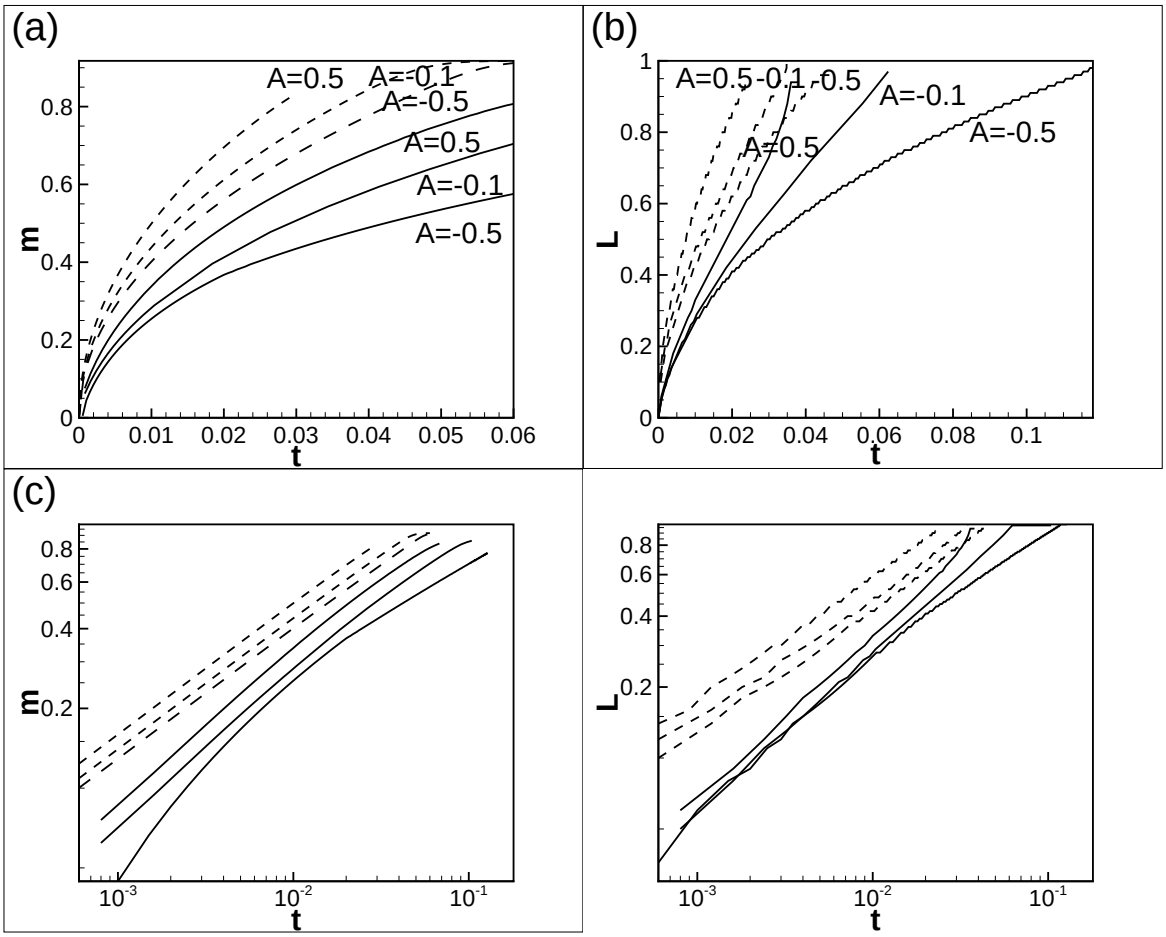

Fig. 4.27 For different values of the parameter A. (a) The amount of the mass of the solvent penetrating into the tube as a function of time. (b) The position of the solvent/solute interface as a function of time. The values of the parameter A are shown in the pictures. The dashed lines depict the data obtained in single tube model and the solid lines depict the data obtained from the model with the blocks. (c) and (d) show the same results but in logarithmic coordinates.

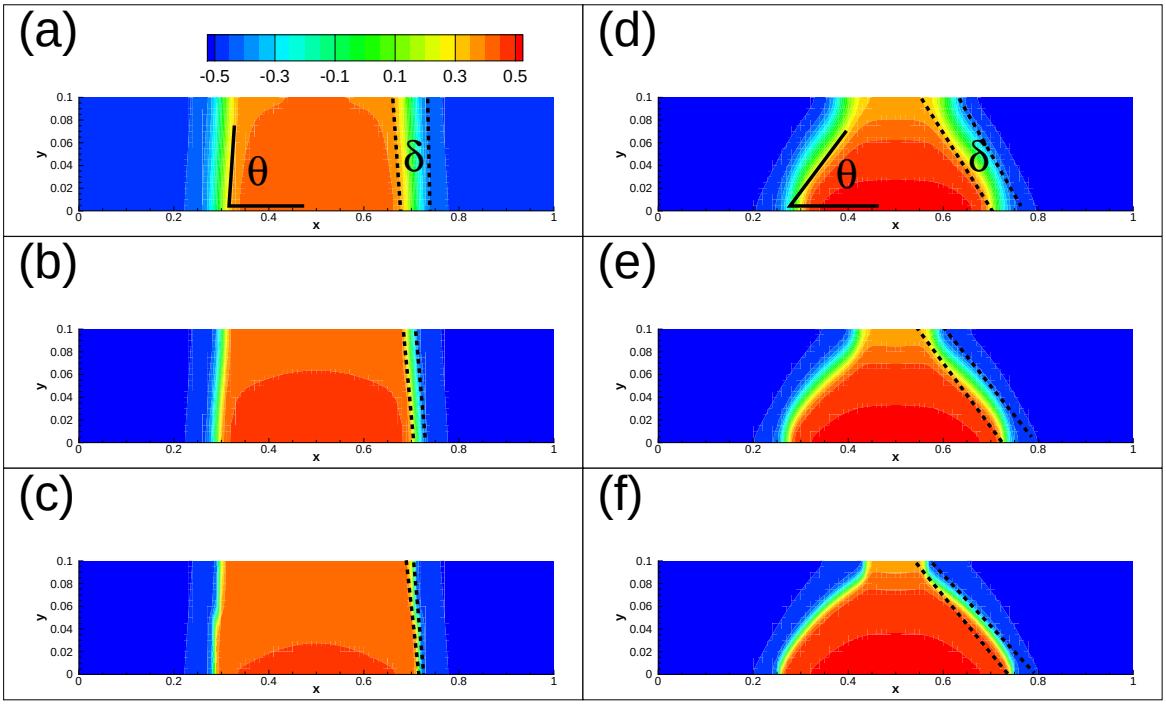

Fig. 4.28 The shape of the interface under the neutral walls ($t = 0.02$). In (a), (b), and (c), $Gr = 1$ and $Ca = 4 \times 10^4$, $Ca = 10^4$ and $Ca = 2.5 \times 10^5$. In (d), (e), and (f), $Gr = 10$ and $Ca = 4 \times 10^4$, $Ca = 10^4$ and $Ca = 2.5 \times 10^5$. θ and δ in this figure represent the apparent contact angle and thickness of the interface.

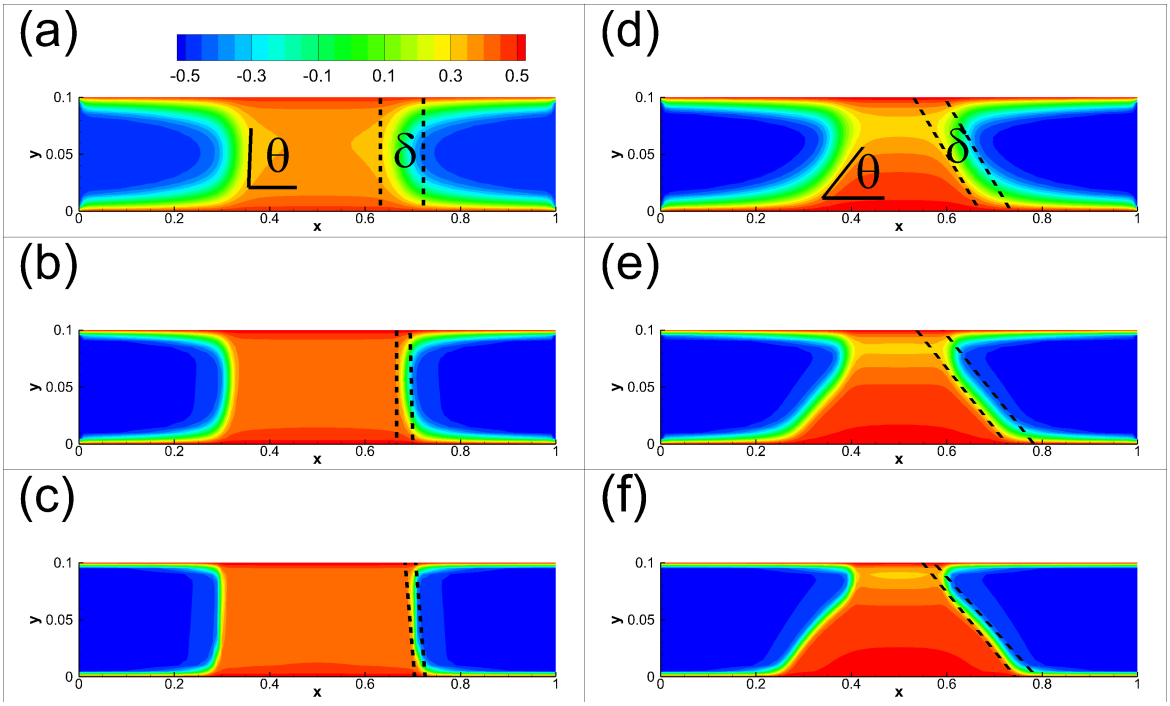

Fig. 4.29 The shape of the interface for the case of the solute-philic walls ($t = 0.02$). (a),(b) and (c) are for cases with $Gr = 1$ and different Ca number (From (a) to (c), $Ca = 4 \times 10^{-4}$, $Ca = 10^{-4}$ and $Ca = 2.5 \times 10^{-5}$). (d), (e) and (f) are for same cases but for $Gr = 10$. θ and δ in this figure represent the apparent contact angle and thickness of the interface.

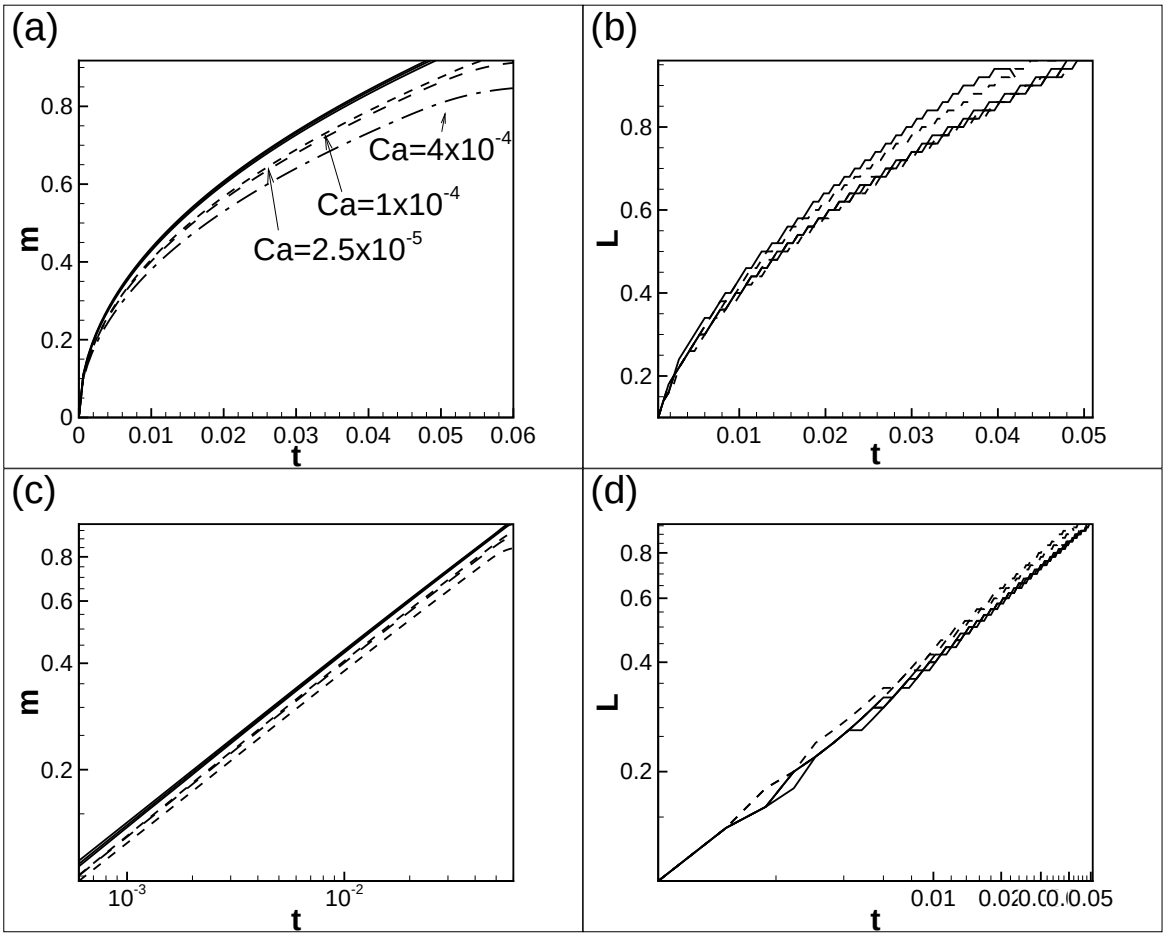

Fig. 4.30 The mass of solvent penetrating into the tube as a function of time for different values of the parameter *Ca*. (a) The mass of the solvent penetrating into the tube as a function of time. (b) The position of the solvent/solute interface as a function of time. The values of the capillary number *Ca* are shown in the picture. The solid lines depict the data obtained under the neutral walls condition and the dashed lines depict the data obtained from the model under the solute-philic walls condition. (c) and (d) show the same results but in logarithmic coordinates. The ticker solid lines show the reference dependencies ($t^{0.6}$).

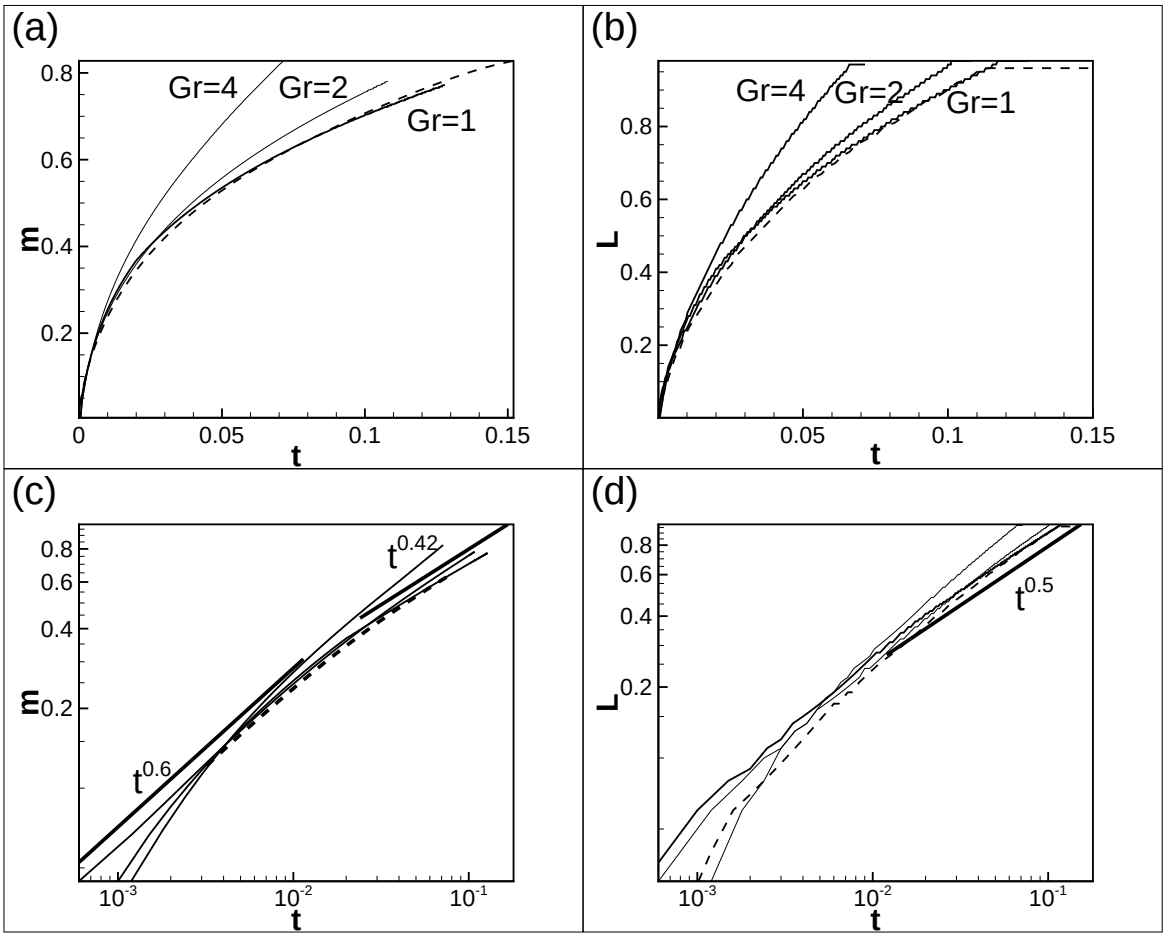

Fig. 4.31 The effect of hydrodynamics on mass transfer. (a) The mass of the solvent penetrating into the tube as a function of time. (b) The position of the solvent/solute interface as a function of time. The values of the parameter *Gr* have already been marked onto the relevant curves. The data were obtained under $Re = 100$ and the dashed line depicts data for $Re = 1000$.(c) and (d) show the same results but in logarithmic coordinates. The ticker solid lines show the reference dependencies.

Inclusion of the hydrodynamic flow

The effect of hydrodynamics depends on the parameter *Gr* and *Re*. *Gr* was already found to be able to affect the shape of solvent/solute interface. At the higher value of *Gr*, the contact angle of the interface to the tube wall increases. *Gr* is also relevant to the barodiffusion and the gravity-driven flows. In the Fickian simulation, the value of the parameter *Gr* was estimated through the experimental data. However, in the phase-field mode, all phenomenological parameters are defined differently and the values are not known. Since the obtained interface shapes are similar to the experimental observations, the value of *Gr* should be in the same order with the *Gr* used in the last section. Fig.4.31 depicts the result under different *Gr* and *Re*. The flows are found to be weak and the effect of *Re* can be omitted. The dissolution become faster when *Gr* increases but the time dependence of its rate remains unchanged (or slightly changed).

The effect of the tube's diameter

In the paper [2], the rate of dissolution was observed to be proportional to the square of the tube's diameters ($\frac{dL}{dt} \propto d^2$). Such a relation was not obtained in the previous simulations that were based on the classical Fick's law. This was re-examined within the phase-field model, though the results are found to be similar to the earlier observations of the Fickian model (Fig.4.32). For the single capillary, the dependence on the tube's diameter is negligible. In the model with added blocks, it is found that the dissolution occurs faster in the tubes of the smaller diameters. This obviously contradicts to the experimental observations. The overall time dependence is close to the previous simulations that were based on the Fick's law and the results of the thinner tube in the model with added blocks are approaching the data obtained from the single tube model.

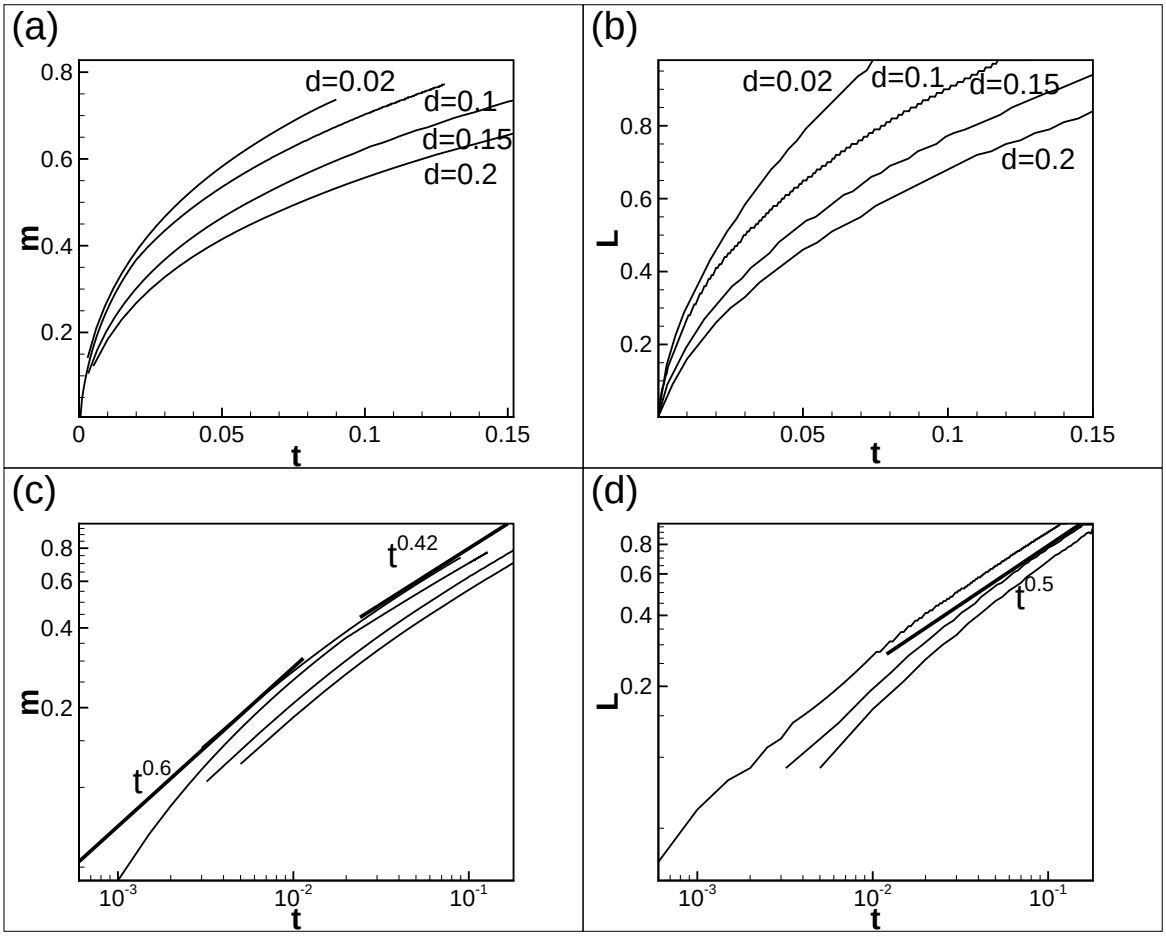

Fig. 4.32 The mass transfer in tubes of different tube diameters. (a) The mass of the solvent penetrating into the tube as a function of time. (b) The portion of the capillary occupied by the solvent phase vs time. The values of the tube's diameter have already been marked onto the relevant curves. (c) and (d) show the same results in logarithmic coordinates. The ticker solid lines show the reference dependencies.

Chapter 5

Conclusion

The aim of our study is to develop and verify the physics-based model for the accurate description of the miscible multi-phase systems. Particularly, we aim to reproduce the experimental observations of the moving solvent/solute boundaries that were reported in paper [2]). The main achievements from this work evidently show that the phase-field model (Cahn-Hillird model) can produce the experimental observations on the shape of the interface (the miscible liquid/liquid boundary). We have also proved that the classical Fickian approach is unable to reproduce the observed phenomena. However, the dynamics of diffusion observed in experiments [2] remains unexplained and the further studies are still needed.

The work was started by employing the theory based on the classical Fick's law of diffusion with strongly concentration-dependent diffusion coefficient. The result gives the general features of the Fickian diffusion that the solvent/solute boundaries stay stationary (if there are no flows) and just become thicker through diffusive smearing. The rate of diffusion was evaluated by the rate of mass transfer and it obeys the classical Fickian law, i.e. it is proportional to $t^{\frac{1}{2}}$. The model was also coupled with the Navier-Stokes equations to take into account of the effect of hydrodynamics. To accurately describe the experiment [2], two blocks were added at the sides of the tube. The results showed that the flow is relatively weak and the geometry of the added blocks changes the rate of mass transfer to be 0.6 time-dependence. The model was also improved by adding the Korteweg's force term to mimic the effect of the surface tension but the result was found to be not very different. The simulations were also extended to the 3D case by employing the commercial package ANSYS Fluent. The rate of mass transfer was found to be unchanged. By modelling the mixture viscosity on the basis of the mass-weighted mixing law, the results for the standard value of the gravity acceleration can be used and the rate of diffusion ($\frac{\partial m}{\partial t}$ or $\frac{\partial L}{\partial t}$) is found to be proportional to $t^{0.4}$.

Then an advanced model that is based on the phase-field approach was developed. Within this approach, the phenomenological relation for the diffusion flux is redefined. In the Fick's law, it is assumed that diffusion is driven by the gradient of concentration. However, in the phase-field approach, it is assumed that diffusion is driven by the gradient of the chemical potential. The expression of the chemical potential includes new terms that generate new effects (surface tension and barodiffusion). The simulations were repeated for the same geometries. The distinguishable interfaces separating two liquids can be clearly observed. The interface was observed balanced by the gravity and surface tension forces. The inclined shape of the interface was observed to be very similar to the experimental observations. However, the rate of mass transfer is still observed to follow the dependence of the Fickian diffusion, that is proportional to $t^{\frac{1}{2}}$. In the geometries with the two side-added blocks, the rate of mass transfer also changes to be 0.6 time-dependence. The model is also coupled with the Navier-Stokes equations. The addition of the hydrodynamic motion did not change the result. As the interfaces are distinguishable, it allows tracking the position of the interface but the result is still similar to its rate of mass transfer. Despite all those efforts, it has to be concluded that the understanding of diffusion in liquid/liquid mixture is improved but still remains incomplete.

Only some experimental observations could be reproduced. The shape of the distinguishable interface can be clearly observed, but the kinetics of diffusion in liquid/liquid mixtures remain unexplained. The results for the Fick's and phase-field models were found to be quite similar except the shape of the interface. In addition, neither approach allows reproducing the experimentally observed dependencies of the speed of the solute/solvent boundary on the tube's diameter. In the experiment, the dissolution occurred slower in smaller tubes, with the speed proportional to d^2 (here d is the tube's diameter). This was also not observed in the numerical simulations, where the rate of dissolution is either is independent of the tube's diameter, or even increases in the tubes of smaller diameters.

The attempts are also made by redefining the phenomenological relation between the diffusion flux and the viscous stress tensor. This means the driven forces is determined by the gradient of the chemical potential and the gradients of the velocity components. This is similar to the diffusion in the solvent/polymer systems, where Non-Fickian diffusion is frequently reported. It is known that diffusion in polymers at rubbery state is mostly Fickian diffusion and the polymers behave more like the liquid if its molecular weight is small or chain length is shorter. If the polymer is at glassy state or experience a phase transformation between the rubbery state and glassy state, diffusion is found to be non-Fickian. After applying one model for diffusion in glassy polymer and one model for diffusion with glass transition, it is found the model brings unrealistic features into the models and thus it is

not an option. Thus, the further study is stil needed to explain the kinetics of diffusion in liquid/liquid mixture. The possible direction of the further research can be done by including anisotropy or studying the effect of latent heat in dissolution, which will be discussed in the next chapter.

Chapter 6

Future work

Diffusion in liquid/liquid mixture has been studied within both the classical Fickian approach and an advanced model - the phase-field approach. Within the phase-field model, the effect of the surface stress, barodiffusion and hydrodynamics were included. Nevertheless, not all experimental observations were reproduced. In this section, we would like to briefly discuss some possible directions for further studies. Firstly, the diffusive interface model can be improved by adding anisotropy. In chapter 1, it was mentioned that the results from molecular dynamics simulations [72, 73] showed the mobility coefficients along the interface and perpendicular to the liquid/liquid interface are different. This means an accurate model of the liquid/liquid interface should be anisotropic. In the current model, the classical isotropic relations between thermodynamic forces and fluxes are used and this can be reconsidered. We made an attempt to use the mathematical model for polymer systems to describe our problem but the simulated phenomena were found different from our expectation. Another direction is to include the non-isothermal effect. Although the diffusion process in the experiment [2] underwent under the isothermal condition, latent heat may be released/absorbed because of the liquid/liquid phase transition. We discuss more details about these two directions in this chapter.

6.1 Anisotropy

The current phase-field model assumes the medium is locally isotropic (i.e that all directions are identical). This is not true in the presence of the liquid/liquid interface, because interfacial diffusion occurs differently in the different directions (i.e. along and across the interface). It should be noticed that the bulk phases of the two liquids system are isotropic, and problem of anisotropic is only introduced because of the presence of the liquid/liquid interface.

To add the anisotropy to the model, the phenomenological relations between the thermodynamic fluxes and the thermodynamic forces need to be reconsidered. Roshin and Truskinovsky [136] discussed the form of the transport equations for the medium with local anisotropy. In their model, the expression of the viscous stress tensor reads as,

$$\begin{aligned}\varsigma_{ij} = &(a_1 e_{kk} + a_2 e_{kl} v_k v_l - a_4 \mu) + 2a_5 \left(e_{ij} - \frac{1}{3} e_{kk} I_{ij} \right) + 2a_6 \left(e_{jk} v_i v_k + e_{ik} v_i v_k \right) \\ &+ (a_2 e_{kk} + a_7 e_{kl} v_k v_l - a_8 \mu) v_i v_j. \end{aligned} \tag{6.1}$$

Here, $e_{ij} = \frac{1}{2}\left(\nabla_i v_j + \nabla_j v_i\right)$ is the strain tensor.

The equation for the mass transport reads as,

$$\rho \frac{dC}{dt} = -a_3 e_{kk} - a_8 e_{kl} v_k v_l - \rho \Gamma \mu, \tag{6.2}$$

Here, it should be noticed that the model in paper [136] assumes the kinetics is described by the Landau-Ginzburg model ($\frac{dC}{dt} = -\Gamma \frac{\partial f}{\partial C}$). As it has been discussed in Chapter 1, it should be replaced by the Cahn-Hilliard model for a liquid/liquid mixture. This alters the equation of the mass transport to be,

$$\rho \frac{dC}{dt} = -a_3 e_{kk} - a_8 e_{kl} v_k v_l + \rho \Gamma \nabla^2 \mu. \tag{6.3}$$

In above equations, a_1 to a_8 are all phenomenological coefficients. In paper [136], it only discussed some constrains for these coefficients, which are, a_1 a_5, a_6, a_7, and Γ are not negative values, and also $a_1 a_7 \geq a_2 a_2$.

If we neglect the non-isothermal effects and all velocity terms, the kinetic equation of diffusion in a liquid/liquid mixture can be written as,

$$\frac{dC}{dt} = \Gamma \nabla^2 \frac{\partial f}{\partial C}. \tag{6.4}$$

This equation is same with the Cahn-Hilliard equation used in Chapter 2, which means this model does not include the anisotropy for the problem of the pure diffusion.

From the above discussion, it is clear that the anisotropy can be included in Roshin and Truskinovsky's model [136] when hydrodynamics is taken into account. A 2D formulation of the new phenomenological relations between thermodynamic forces and fluxes for the dissolution in a liquid/liquid based including hydrodynamics can be written as,

The viscous stress tensor reads as,

$$\begin{aligned}\varsigma_{xy} = a_5\left(\nabla_x v_y + \nabla_y v_x\right) + a_6\left(\left(\nabla_y v_x + \nabla_x v_y\right) v_x^2 + \left(\nabla_x v_y + \nabla_y v_x\right) v_y^2\right) + \\ a_2\left(\nabla_x v_y + \nabla_y v_x\right) v_x v_y + a_7\left(\nabla_x v_y + \nabla_y v_x\right)\left(v_x v_y\right)^2 + \left(a_4 + a_8 v_x v_y\right)\nabla^2\mu.\end{aligned} \tag{6.5}$$

And the equation of mass transport reads as,

$$\frac{dc}{dt} = -\frac{a_8}{\rho}\left(\nabla_x v_y + \nabla_y v_x\right) v_x v_y + \Gamma\nabla^2\mu. \tag{6.6}$$

It should be noticed that the classical theory for the isotropic medium only contains the terms with coefficient a_5 and Γ. Thus the additional terms should describe the anisotropy medium. The Cahn-Hilliard-Navier-Stokes equations with the substitutions of the above relations (Eq.6.5 and Eq.6.6) will then take into account of the anisotropy of the heterogeneous medium introduced by the presence of interface.

6.2 Non-isothermal effects

To illustrate the non-isothermal effects that may occur over the dissolution, we start by writing the equilibrium condition for a non-isothermal liquid/liquid mixture [56]:

$$\mu_1\left(P,T\right) - C_1 T = \mu_2\left(P,T\right) - C_2 T. \tag{6.7}$$

Here, P and T are the pressure and temperature of the system. At a given pressure which we assumed in previous sections, the chemical potential only depends on temperature. μ_1, μ_2, C_1, and C_2 are the chemical potential and concentration for the liquid 1 and the liquid 2. The term $C_1 T$ and $C_2 T$ implies that diffusion occurs between two liquids. Assume at another point (P_0, T_0), there is no diffusion between two phases and the equilibrium condition of two pure liquid phase can be written as:

$$\mu_1\left(P_0,T_0\right) = \mu_2\left(P_0,T_0\right). \tag{6.8}$$

If we assume the liquid/liquid mixture reaches its equilibrium state (P_0, T_0) from an non-equilibrium state (P,T), a series expansion in terms of $\Delta T = T - T_0$ and $\Delta P = P - P_0$ can be written as:

$$\frac{\partial\mu_1}{\partial T}\Delta T + \frac{\partial\mu_1}{\partial P}\Delta P - C_1 T = \frac{\partial\mu_2}{\partial T}\Delta T + \frac{\partial\mu_2}{\partial P}\Delta P - C_2 T. \tag{6.9}$$

Because the term $\frac{\partial\mu}{\partial T} = -S$ is entropy and $\frac{\partial\mu}{\partial P}$ is the volume of the solvent. Eq.(6.9) can be

written as:

$$(-S_1 + S_2)\,\Delta T + (V_1 - V_2)\,\Delta P = (C_1 - C_2)\,T. \tag{6.10}$$

Here, $(S_2 - S_1)T = q$ is the amount of energy released or absorbed during the phase change, ($q = ml$, m is the mass of the substance, l is the specific latent heat for the substance). Thus we can see the latent heat will be released during the phase transformation. The typical phase transformation that the latent heat is included in the problem of melting or boiling where phase changes from solid to liquid or from liquid to gas. However, the experiment work [137] shows the heat can be released along with diffusion between two gases.

The non-isothermal effects for incompressible fluids are described by the general heat equation. This equation is derived from the equation of energy conservation, which reads as [67, 138],

$$\rho c_p \left(\frac{\partial T}{\partial t} + \vec{v} \cdot \nabla T \right) = \nabla (\kappa \nabla T) + \tau_{ik} \frac{v_i}{h_k}. \tag{6.11}$$

Here, c_p is the specific heat of the substance at constant pressure, κ is the thermal conductivity, and $\tau_i k \frac{v_i}{h_k}$ is contributed from the effect of the viscosity. If we neglect all terms with velocity and viscosity, the general heat equation changes to be the Fourier's equation for thermal conduction,

$$\frac{\partial T}{\partial t} = \nabla (\kappa \nabla T). \tag{6.12}$$

Papers [68, 69, 71] studied the non-isothermal problem in miscible liquids based on the classical Fick's law. In their model, the cross effect of diffusion on thermal diffusion is ignored. The effect of the latent heat is normally considered to be small compared with the large temperature gradient used in the works [68, 69, 71]. Thus the problem is likely to be described by the full set of transport equations for heat and mass transfer, which can be written as below:

$$\frac{\partial T}{\partial t} + \vec{v} \cdot \nabla T = \kappa \nabla^2 T, \tag{6.13}$$

$$\frac{\partial C}{\partial t} + \vec{v} \cdot \nabla C = D \nabla^2 C, \tag{6.14}$$

$$\frac{\partial \vec{v}}{\partial t} + (\vec{v} \cdot \nabla)\,\vec{v} = -\frac{1}{\rho} \nabla P + \frac{1}{\rho} \nabla \varsigma, \tag{6.15}$$

$$\nabla \cdot \vec{v} = 0. \tag{6.16}$$

The above model neglects the cross effect of diffusion on thermal diffusion. In general, the heat flux depends on both the temperature gradient (∇T) and the concentration gradient

(∇C):

$$J_{heat} = M_T \nabla T + M_{TC} \nabla C. \tag{6.17}$$

The general expression for the mass flux can be written as,

$$J_{mass} = M_C \nabla C + M_{CT} \nabla T. \tag{6.18}$$

In Eq.6.17 and Eq.6.18, M_T, M_C, M_{TC} and M_{CT} are the coefficients of the heat transfer, the mass transfer, the cross effect of diffusion on heat transfer, and the cross effects of heat transfer on diffusion, respectively. The thermal effect on diffusion is known as Soret effect. Currently, the model to study the Soret-driven dissolution [139, 140] assumes the density of mixture is defined as,

$$\rho = \rho_0 \left(1 - \beta_t \left(T - T_0\right) - \beta_C \left(C - C_0\right)\right) \tag{6.19}$$

Here, ρ_0, C_0 and T_0 are the background values. β_t and β_C are the thermal and mass expansion coefficients, defined by $\beta_t = -\frac{1}{\rho_0}\left(\frac{\partial \rho}{\partial T}\right)_C > 0$ and $\beta_C = -\frac{1}{\rho_0}\left(\frac{\partial \rho}{\partial C}\right)_T < 0$. In the paper [140], the values of these parameters for a water-ethanol mixture with the initial concentration of water to be $C_0 = 0.6088\%wt$ were given as $\beta_T = 7.86 \times 10^{-4} K^{-1}$ and $\beta_C = -2.12 \times 10^{-1}$.

In the paper [139], the governing equations to describe the Soret-driven dissolution with the Boussinesq approximations were written as:

$$\begin{aligned}
\nabla \cdot \vec{v} &= 0, \\
\frac{\partial \vec{v}}{\partial t} + (\vec{v} \cdot \nabla)\vec{v} &= -\frac{1}{\rho_0}\nabla p + \upsilon \nabla^2 \vec{v} + g\left[\beta_T \left(T - T_0\right) + \beta_C \left(C - C_0\right)\right]\vec{\gamma}, \\
\frac{\partial T}{\partial t} + (\vec{v} \cdot \nabla)T &= \chi \nabla^2 T, \\
\frac{\partial C}{\partial t} + (\vec{v} \cdot \nabla)C &= D\nabla^2 C + D_T \nabla^2 T.
\end{aligned} \tag{6.20}$$

Here, υ is the kinematic viscosity of the mixture, χ is the thermal diffusivity of the mixture. D is the diffusion coefficient, and D_T is the thermal diffusion coefficient.

The above model still uses the classical Fick's law to described diffusion. The phase-field model for the non-isothermal liquid/liquid system is yet to be developed. In the book [67], the diffusion flux $\vec{i}$ and the heat flux $\vec{q}$ for the thermal diffusion are written as:

$$\vec{i} = \alpha \nabla \mu - \beta \nabla T, \tag{6.21}$$

$$\vec{q} = \left(\mu + \frac{\beta T}{\alpha}\right)\vec{i} - \kappa \nabla T. \tag{6.22}$$

Here, α and β are all coefficients. The gradient of chemical potential can also be expressed as

$$\nabla \mu = \left(\frac{\partial \mu}{\partial C}\right)_{P,T} \nabla C + \left(\frac{\partial \mu}{\partial T}\right)_{C,P} \nabla T + \left(\frac{\partial \mu}{\partial P}\right)_{(C,T)} \nabla P. \tag{6.23}$$

Then the diffusion flux and heat flux can be rewrite as:

$$\vec{i} = -\rho D\left(\nabla C + \frac{\kappa_T}{T}\nabla T + \frac{\kappa_P}{P}\nabla P\right), \tag{6.24}$$

$$\vec{q} = \left[\kappa_T \left(\frac{\partial \mu}{\partial C}\right)_{P,T} - T\left(\frac{\partial \mu}{\partial T}\right)_{C,P} + \mu\right]\vec{i} - \kappa \nabla T. \tag{6.25}$$

Here, $D = \frac{\alpha}{\rho}\left(\frac{\partial \mu}{\partial C}\right)_{P,T}$, $k_T = \frac{T}{D\rho}\left[\left(\frac{\partial \mu}{\partial T}\right)_{C,P} + \beta\right]$, and $k_p = \frac{P\left(\frac{\partial V}{\partial C}\right)_{P,T}}{\left(\frac{\partial \mu}{\partial C}\right)_{P,T}}$ (V is the specific volume).

In the paper [117], the thermodynamic entropy density for the case of dendritic solidification is defined as a function of the order parameter ϕ, the concentration C and energy density e. Then the time-dependent evaluations of the above variables are expressed as below. Firstly, the species balance equation reads as,

$$\begin{aligned}\frac{\partial C}{\partial t} = {} & \nabla \cdot \left[M_C\left(\frac{R}{V_m}\frac{1}{C(1-C)} - \frac{2}{T}\Omega(\phi)\right)\nabla C\right] + \\ & \nabla \cdot \left[\frac{M_C}{T}\left(\left(\frac{\partial f_A}{\partial \phi} - \frac{\partial f_B}{\partial \phi}\right) + \frac{d\Omega(\phi)}{d\phi}(1-2C)\right)\nabla \phi\right].\end{aligned} \tag{6.26}$$

Here, M_C is the coefficient of the diffusional mobility of different phases. R is the ideal gas constant. V_m is the molar volume. T is the temperature, f_A and f_B are the free energy densities. $\Omega(\phi)$ is a parameter related to the enthalpy of the mixing. The order parameter ϕ is evaluated by:

$$\frac{\partial \phi}{\partial t} = M_\phi\left[\varepsilon^2 \nabla^2 \phi - (1-C)\frac{1}{T}\frac{\partial f_A}{\partial \phi} - C\frac{1}{T}\frac{\partial f_B}{\partial \phi} - \frac{1}{T}\frac{d\Omega(\phi)}{d\phi}C(1-C)\right]. \tag{6.27}$$

Here, M_ϕ is the mobility coefficient for the order parameter. Finally, the energy density is evaluated by:

$$\frac{\partial e}{\partial T}\dot{T} + \frac{\partial e}{\partial \phi}\dot{\phi} + \frac{\partial e}{\partial C}\dot{C} = \nabla \cdot \left(\frac{M_e}{T^2}\nabla T\right). \tag{6.28}$$

Here, M_e is the coefficient related to the heat conduction. The thermal effect along with phase transition is evaluated through the general equation of heat. This model was solved computationally in paper [141] to model the phase transition between solids and liquids. They [141] obtained the growth rate of the thickness of the intermediate phase caused by the phase transition, which was reported to be proportional to $t^{0.2}$. Furthermore, the position of the interface[7] was reported to be proportional to $t^{0.5}$.

In the model of solidification/melting, the latent heat was defined to drive the intermediate phase layer. In paper [142], latent heat transfer ΔH is evaluated by,

$$\frac{\partial \rho H}{\partial t} + \nabla \cdot (\rho \vec{v} H) = \nabla \cdot (k \nabla T), \tag{6.29}$$

and,

$$H = H_0 + \int_{T_0}^{T} dT + \Delta H. \tag{6.30}$$

Here, H is latent heat, the notation 0 denotes the background values. Velocity $\vec{v}$ is calculated from the Navier-Stokes equations.

The effect of the temperature gradients is crucial for the accurate modelling of the phase transition driven by heat. For such problems, the latent heat is also a necessary thermodynamics property that needs to be considered. Generally, diffusion in the liquid/liquid mixture is exclusively a process of mass transport and the temperature of the mixture is considered to be constant. However, as it has been mentioned at the beginning of this section, such effect should exist. Among various types of phase transition, the problem of the liquid/vapour interface maybe the case that is most closed to the liquid/liquid interface. There is very few studies reported the phase-field model of the liquid/vapour transition that includes the temperature gradients [143]. The set of the governing equation can be written as [144]: The free energy function read as,

$$F = F_0(\rho, T) + \frac{\varepsilon}{2} (\nabla \rho)^2, \tag{6.31}$$

Here, they [144] take F as the volumetric free energy.

[7] In paper [141], it is defined as the average position between the two interfaces separated by the liquid, the intermediate phases and the solid.

The classical part of the free energy reads as,

$$F_0(\rho,T) = A(T)(\rho-\rho_v)^2(\rho-\rho_l)^2 + g_0 + \frac{\frac{Cv_v}{\rho_l}-\frac{Cv_l}{\rho_v}}{\frac{1}{\rho_v}-\frac{1}{\rho_l}}\left(T\ln\left(\frac{T}{T_0}\right)-(T-T_0)\right)\rho - P_0 - \frac{L_0}{\frac{1}{\rho_v}-\frac{1}{\rho_l}}\frac{T-T_0}{T_0} + \frac{Cv_v-Cv_l}{\frac{1}{\rho_v}-\frac{1}{\rho_l}}\left(T\ln\left(\frac{T}{T_0}\right)-(T-T_0)\right). \tag{6.32}$$

Here, $A(T)$ is a parameter determined by the saturation condition, i.e. $\left(\frac{\partial P}{\partial \rho}\right)_v = 2A\rho_v(\rho_l-\rho_v)^2$ and $\left(\frac{\partial P}{\partial \rho}\right)_l = 2A\rho_l(\rho_l-\rho_v)^2$. ρ_v and ρ_l are the saturation density of the vapour and liquid, respectively. g_0 is specific Gibbs free energy at equilibrium state. P_0 is the pressure at equilibrium state. L_0 is latent heat. Cv is the heat capacity at the constant volume.

The internal energy is obtained from the classical thermodynamical relation,

$$\mu = \frac{F}{\rho} + Ts. \tag{6.33}$$

Here, s is entropy.

The equation of evolution of the internal energy reads as,

$$\rho\frac{d\mu}{dt} = -\nabla\cdot\vec{q} + \Pi : \nabla\vec{v}. \tag{6.34}$$

Here, $\vec{q}$ is heat flux and Π is the stress tensor ($\Pi = -PI + \varsigma$, I is identity tensor).

The equation of mass balance reads as,

$$\frac{d\rho}{dt} + \rho\nabla\cdot\vec{v} = 0. \tag{6.35}$$

The equation of momentum balance reads as,

$$\rho\frac{d\vec{v}}{dt} = \nabla\cdot\Pi. \tag{6.36}$$

The equation of the energy balance reads as,

$$\rho\frac{de}{dt} = \nabla\cdot\left(\varepsilon\frac{d\rho}{dt}\right) + \nabla\cdot(k\nabla T) + \nabla\cdot(\vec{v}\cdot\Pi). \tag{6.37}$$

The equation of evolution of the temperature reads as,

$$\rho Cv\frac{dT}{dt} = \nabla\cdot(\kappa\nabla T) - \rho T\left(\frac{\partial s}{\partial \rho}\right)_T\frac{d\rho}{dt} + \varsigma : \nabla\vec{v}. \tag{6.38}$$

Here, ς is viscous stress tensor. In paper [144], they reported the increases the thickness of the interface. In paper [143], they observed the phenomenon of the Rayleigh–Benard instability due to the temperature gradient.

In this section, we have demonstrated several theories including non-isothermal effects and we have showed that the phase-field theory for the thermally perturbed diffusion in a liquid/liquid mixture has not been reported. We have also viewed some phase-field theories with non-isothermal effects, and the most closed case to the liquid/liquid system should be the liquid-vapour phase transition that is driven by heat. However, only few studies can be found.

References

[1] J. Crank and G. Park, *Diffusion in Polymers*. Academic Press, 1968.

[2] M. Stevar and A. Vorobev, "Shapes and dynamics of miscible liquid/liquid interfaces in horizontal capillary tubes," *Journal of Colloid and Interface Science*, vol. 383, no. 1, pp. 184 – 197, 2012.

[3] S. B. D. J. O. Shin and P. F. Linden, "Gravity currents produced by lock exchange," *J.Fluid Mech.*, vol. 521, pp. 1–34, 2004.

[4] V. Alvarado and E. Manrique, "Enhanced oil recovery: An update review," *Energies*, vol. 3, pp. 1529–1975, 2010.

[5] A. J. Brodie, B. S. Jhaveri, T. P. Moulds, and S. M. Hetland, "Review of gas injection project in bp," *Society of Petroleum Engineers*, 2012.

[6] D. Erbas, E. Duncan, P. Zhang, J. A. Brodie, and V. Daae, "Bp north sea miscible gas injection projects review," *Society of Petroleum Engineers*, 2013.

[7] S. Haszeldine, "Opportunities for co_2 storage around scotland — an integrated strategic research study," 2009.

[8] F. Odeh, A. Bawab, M. Fayyad, and A. Bozeya, "Surfactant enhanced olive oil mill wastewater remediation," *{APCBEE} Procedia*, vol. 5, pp. 96 – 101, 2013. 4th International Conference on Environmental Science and Development- {ICESD} 2013.

[9] J. M. D. Valle, G. A. Núñez, and R. I. Aravena, "Supercritical co_2 oilseed extraction in multi-vessel plants. 1. minimization of operational cost," *The Journal of Supercritical Fluids*, vol. 92, no. 0, pp. 197 – 207, 2014.

[10] D. Green and G. Willhite, *Enhanced Oil Recovery*. Richardson, US: Society of Petroleum Engineers, 1997.

[11] S. Strand, T. Puntervold, and T. Austad, "Water based {EOR} from clastic oil reservoirs by wettability alteration: A review of chemical aspects," *Journal of Petroleum Science and Engineering*, vol. 146, pp. 1079 – 1091, 2016.

[12] Y. Kim, H. Jang, and J. Lee, "Diagnostic plot model to evaluate injection performance in polymer {EOR} process," *Journal of Petroleum Science and Engineering*, pp. –, 2016.

[13] S. Kumar and A. Mandal, "Studies on interfacial behavior and wettability change phenomena by ionic and nonionic surfactants in presence of alkalis and salt for enhanced oil recovery," *Applied Surface Science*, vol. 372, pp. 42 – 51, 2016.

[14] A. Bera and H. Belhaj, "Ionic liquids as alternatives of surfactants in enhanced oil recovery—a state-of-the-art review," *Journal of Molecular Liquids*, vol. 224, Part A, pp. 177 – 188, 2016.

[15] A. Bera and T. Babadagli, "Status of electromagnetic heating for enhanced heavy oil/bitumen recovery and future prospects: A review," *Applied Energy*, vol. 151, pp. 206 – 226, 2015.

[16] M. R. Faradonbeh, T. Harding, and J. Abedi, "Semi-analytical modeling of steam-solvent gravity drainage of heavy oil and bitumen: Steady state model with linear interface," *Fuel*, vol. 183, pp. 568 – 582, 2016.

[17] V. Alvarado and E. Manrique, "Enhanced oil recovery: An update review," *Energies*, vol. 3, pp. 1529–1975, 2010.

[18] W. Guan, C. Xi, Y. Chen, X. Zhang, Muhetar, J. Liang, J. Huang, and J. Wu, "Fire-flooding technologies in post-steam-injected heavy oil reservoirs," *Petroleum Exploration and Development*, vol. 38, no. 4, pp. 452 – 463, 2011.

[19] Z. Wang and Y. Xu, "Review on application of the recent new high-power ultrasonic transducers in enhanced oil recovery field in china," *Energy*, vol. 89, pp. 259 – 267, 2015.

[20] A. F. Pashchenko and P. G. Ageev, "Elastic waves and plasma – a new era of enhanced oil recovery," *AIP Conference Proceedings*, vol. 1738, no. 1, 2016.

[21] P.-S. Kang, J.-S. Lim, and C. Huh, "Screening criteria and considerations of offshore enhanced oil recovery," *Energies*, vol. 9, p. 44, 2016.

[22] T. W. Teklu, W. Alameri, R. M. Graves, H. Kazemi, and A. M. AlSumaiti, "Low-salinity water-alternating-co2 eor," *Journal of Petroleum Science and Engineering*, vol. 142, pp. 101 – 118, 2016.

[23] M. Riazi and A. Golkari, "The influence of spreading coefficient on carbonated water alternating gas injection in a heavy crude oil," *Fuel*, vol. 178, pp. 1 – 9, 2016.

[24] U. D. o. E. National Energy Technology Laboratory, "Carbon dioxide enhanced oil recovery - untapped domestic energy supply and long term carbon storage solution," *US Department of Energy*, 2010.

[25] J. Bear, *Dynamics of Fluids in Porous Media*. Dover Civil and Mechanical Engineering Series, Dover, 1972.

[26] J. Bear and A. H. Cheng, *Modeling Groundwater Flow and Contaminant Transport*. Theory and Applications of Transport in Porous Media, Springer Netherlands, 2010.

[27] Y. S. Zhao, L. L. Li, Y. Su, and C. Y. Qin, "Laboratory evaluation of the use of solvent extraction for separation of hydrophobic organic contaminants from surfactant solutions during surfactant-enhanced aquifer remediation," *Separation and Purification Technology*, vol. 127, pp. 53 – 60, 2014.

[28] X. Qin, G. Huang, A. Chakma, B. Chen, and G. Zeng, "Simulation-based process optimization for surfactant-enhanced aquifer remediation at heterogeneous dnapl-contaminated sites," *Science of The Total Environment*, vol. 381, no. 1–3, pp. 17 – 37, 2007.

[29] E. Lowry, M. Sedghi, and L. Goual, "Molecular simulations of {NAPL} removal from mineral surfaces using microemulsions and surfactants," *Colloids and Surfaces A: Physicochemical and Engineering Aspects*, vol. 506, pp. 485 – 494, 2016.

[30] L. Torres and E. Bandala, *Remediation of Soils and Aquifers*. Nova, New York, US, 2009.

[31] K. Azad, M. G.Rasul, M. M. Khan, S. C. Sharma, and M. A. Hazrat, "Prospect of biofuels as an alternative transport fuel in australia," *Renewable and Sustainable Energy Reviews*, vol. 43, pp. 331–351, 2015.

[32] E. Bahel, W. Marrouch, and G. Gaudet, "The economics of oil, biofuel and food commodities," *Resource and Energy Economics*, vol. 35, pp. 599–617, 2013.

[33] K. Dutta, A. Daverey, and J.-G. Lin, "Evolution retrospective for alternative fuels: First to fourth generation," *Renewable Energy*, vol. 69, pp. 114–122, 2014.

[34] M. Y. Noraini, H. C. Ong, M. J. Badrul, and W. T. Chong, "A review on potential enzymatic reaction for biofuel production from algae," *Renewable and Sustainable Energy Reviews*, vol. 39, pp. 24–341, 2014.

[35] R. Harun, M. Singh, G. M. Forde, and M. K. Danquah, "Bioprocess engineering of microalgae to produce a variety of consumer products," *Renewable and Sustainable Energy Reviews*, vol. 14, pp. 1037–1047, 2010.

[36] L. Brennan and P. Owende, "Biofuels from microalgae- a review of technologies for production, processing and extractions of biofuels and co-oroducts," *Renewable and Sustainable Energy Reviews*, vol. 14, pp. 557–557, 2010.

[37] W. Farooq, W. I. Suh, M. S. Park, and J.-W. Yang, "Water use and its recycling in microalgae cultivation for biofuel application," *Bioresource Technology*, vol. 184, p. 73–81, 2015.

[38] I. Shizas and D. M. Bagley, "Experimental determination of energy contentof municipal wastewater," *J. Energy Eng*, vol. 130, pp. 45–53, 2004.

[39] M. Mubarrak, A. Shaija, and T. V. Suchithra, "A review on the extraction of lipid from microalgae for biodiesel production," *Algal Research*, vol. 7, pp. 117–123, 2015.

[40] G. Cravotto, L. Boffa, S. Mantegna, P. Perego, M. Avogadro, and P. Cintas, "Improved extraction of vegetable oils under high-intensity ultrasound and/or microwaves," *Ultrasonics Sonochemistry*, vol. 15, pp. 898–902, 2008.

[41] S. Balasubramanian, J. D. Allen, A. Kanitkar, and D. Boldor, "Oil extraction from scenedesmus obliquus using a continuous microwave system-design, optimization, and quaity," *Bioresource Technlogy*, vol. 102, pp. 3396–3403, 2011.

[42] A. M. C. Crampon, S.-A. A. Toudji, O. Lepine, and E. Badens, "Influence of pretreatment on supercritical co2 extraction from nannochloropsis oculata," *The Journal of Supercritical Fluids*, vol. 79, pp. 337–344, 2013.

[43] V. Ashokkumar, R. Rengasamy, S. Deepalakshmi, A. Sivalingam, and P. Sivakumar, "Mass cultivation of microalgae and extraction of total hydrocarbons: A kinetic and thermodynamic study," *Fuel*, vol. 119, pp. 308–312, 2014.

[44] J.-Y. Lee, C. Yoo, S.-Y. Jun, C.-Y. Ahn, and H.-M. Oh, "Comparison of several methods for effective lipid extraction from microalgae," *Bioresource Technology*, vol. 101, pp. S75–S77, 2010.

[45] S.-A. Choi, Y.-K. Oh, M.-J. Jeong, S. W. Kim, J.-S. Lee, and J.-Y. Park, "Effects of ionic liquid mixtures on lipid extraction from chlorella vulgaris," *Renewable Energy*, vol. 65, pp. 169–174, 2014.

[46] S.-A. Choi, J.-S. Lee, Y.-K. Oh, M.-J. Jeong, S. W. Kim, and J.-Y. Park, "Lipid extraction from chlorella vulgaris by molten-salt/ionic-liquid mixtures," *Algal Research*, vol. 3, pp. 44–48, 2014.

[47] M. Goto, W. H. Kanda, and S. Machmudah, "Extraction of carotenoids and lipids from algae by supercritical co2 and subcritical dimethyl ether," *The journal of supercritical Fluids*, vol. 96, pp. 245–251, 2015.

[48] S. Tang, C. Qin, H. Wang, S. Li, and S. Tian, "Study on supercritical extraction of lipids and enrichment of dha from oil-rich microalgae," *The Journal of Supercritical Fluids*, vol. 57, pp. 44–49, 2011.

[49] H.-W. Yen, S.-C. Yang, C.-H. Chen, Jesisca, and J.-S. Chang, "Supercritical fluid extraction of valuable compounds from microalgal biomass," *Renewable and Sustainable Energy Reviews*, vol. 184, pp. 291–296, 2015.

[50] E. G. Bligh and W. J. Dyer, "A rapid method of total lipid extraction and purification," *Canadian Journal of Biochemistry and Physiology*, vol. 37, pp. 911–917, 1959.

[51] H. Kanda and P. Li, "Simple extraction method of green crude from natural blue-green microalgae by dimethyl ether," *Fuel*, vol. 90, pp. 1264–1266, 2011.

[52] T. J. Lundquist, I. C. Woertz, N. W. Quinn, and J. R. Benemann, "A realistic technology and engineering assessment of algae biofuel production," tech. rep., 2010.

[53] J. V. O. F. W. T. Rodrigo A. Reis, Ronaldo Nobrega, "Self- and mutual diffusion coefficient equation for pure fluids, liquid mixture and polymeric solutions," *Chemical Engineering Science*, vol. 60, no. 16, pp. 4581–4592, 2005.

[54] R. Bird, W. Stewart, and E. Lightfoot, *Transport Phenomena*. A Wiley International edition, Wiley, 2007.

[55] J.-F. Daïan, *Equilibrium and Transfer in Porous Media 2: Transfer Laws*. John Wiley & Sons, Ltd, 2014.

[56] L. Landau, E. Lifshitz, and L. Pitaevskiĭ, *Statistical Physics*. No. pt. 2 in Course of theoretical physics, Pergamon Press, 1980.

[57] D. D. Joseph and Y. Y. Renardy, "Fundamentals of two-fluid dynamics. pt. ii: Lubricated transport, drops and miscible liquids," in *Fundamentals of two-fluid dynamics. Pt. II: Lubricated transport, drops and miscible liquids Springer-Verlag (Interdisciplinary Applied Mathematics. Vol. 4), 459 p.*, vol. 4, 1993.

[58] P. de Gennes, F. Brochard-Wyart, and D. Quere, *Capillarity and Wetting Phenomena: Drops, Bubbles, Pearls, Waves*. Springer, 2004.

[59] E. I. Franses, O. A. Basaran, and C.-H. Chang, "Techniques to measure dynamic surface tension," *Current Opinion in Colloid Interface Science*, vol. 1, no. 2, pp. 296 – 303, 1996.

[60] A. Vorobev, "Dissolution dynamics of miscible liquid/liquid interfaces," *Current Opinion in Colloid and Interface Science*, vol. 19, no. 4, pp. 300 – 308, 2014.

[61] A. Vorobev and A. Boghi, "Phase-field modelling of a miscible system in spinning droplet tensiometer," *Journal of Colloid and Interface Science*, vol. 482, pp. 193 – 204, 2016.

[62] P. Petitjeans and T. Maxworthy, "Miscible displacements in capillary tubes. part 1. experiments," *Journal of Fluid Mechanics*, vol. 326, pp. 37–56, 11 1996.

[63] C.-Y. Chen and E. Meiburg, "Miscible displacements in capillary tubes. part 2. numerical simulations," *Journal of Fluid Mechanics*, vol. 326, pp. 57–90, 11 1996.

[64] D. Wilhelm and E. Meiburg, "Three-dimensional spectral element simulations of variable density and viscosity, miscible displacements in a capillary tube," *Computers & Fluids*, vol. 33, no. 3, pp. 485 – 508, 2004.

[65] C.-Y. Chen and E. Meiburg, "Miscible displacements in capillary tubes: Influence of korteweg stresses and divergence effects," *Physics of Fluids*, vol. 14, no. 7, 2002.

[66] V. Ugrozov, A. Filippov, C. Paraskeva, G. Constantinides, and V. Starov, "Diffusive dissolution of a drop in a capillary," *Colloids and Surfaces A: Physicochemical and Engineering Aspects*, vol. 239, no. 1–3, pp. 129 – 133, 2004. A collection of papers presented at {XVIth} European Chemistry at Interfaces Conference, 14-18 May, 2003, Vladimir, Russia.

[67] L. Landau and E. Lifshitz, *Fluid Mechanics*. No. v. 6, Elsevier Science, 1959.

[68] J. A. Pojman, N. Bessonov, V. Volpert, and M. S. Paley, "Miscible fluids in microgravity (mfmg): A zero-upmass investigation on the international space station," *Microgravity - Science and Technology*, vol. 19, no. 1, p. 33, 2007.

[69] G. Viner and J. A. Pojman, "Studying diffusion of partially miscible and systems near their consolute point by laser line deflection," *Optics and Lasers in Engineering*, vol. 46, no. 12, pp. 893 – 899, 2008. Diffusion Measurements by Optical Methods: Recent Advances and Applications.

[70] D. Ambrosini and P. K. Rastogi, "Diffusion measurements by optical methods: Recent advances and applications," *Optics and Lasers in Engineering*, vol. 46, no. 12, pp. 849 – 851, 2008. Diffusion Measurements by Optical Methods: Recent Advances and Applications.

[71] D. Antrim, P. Bunton, L. Lewis, B. Zoltowski, and J. Pojman, "Measuring the mutual diffusion coefficient for dodecyl acrylate in low molecular weight poly(dodecyl acrylate) with laser line deflection (wiener's method) and the fluorescence of pyrene," *J Phys Chem B*, vol. 109, pp. 11842 – 11849, 2005.

[72] M. Meyer, M. Mareschal, and M. Hayoun, "Computer modeling of a liquid–liquid interface," *The Journal of Chemical Physics*, vol. 89, no. 2, pp. 1067–1073, 1988.

[73] C. Braga, A. Galindo, and E. A. Müller, "Nonequilibrium molecular dynamics simulation of diffusion at the liquid-liquid interface," *The Journal of Chemical Physics*, vol. 141, no. 15, p. 154101, 2014.

[74] A. Vailati and M. Giglio, "Nonequilibrium fluctuations in time-dependent diffusion processes," *Phys. Rev. E*, vol. 58, pp. 4361–4371, Oct 1998.

[75] F. B. Hicks, T. C. Van Vechten, and C. Franck, "Thermally perturbed barodiffusion in a binary liquid mixture," *Phys. Rev. E*, vol. 55, pp. 4158–4164, Apr 1997.

[76] K. Jamshidi-Ghaleh, M. T. Tavassoly, and N. Mansour, "Diffusion coefficient measurements of transparent liquid solutions using moiré deflectometry," *Journal of Physics D: Applied Physics*, vol. 37, no. 14, p. 1993, 2004.

[77] R. Vuilleumier, V. Ego, L. Neltner, and A. Cazabat, "Tears of wine: the stationary state," *Langmuir*, vol. 11, pp. 4117 – 4121, 1995.

[78] M. Santiago-Rosanne, M. Vignes-Adler, and M. G. Velarde, "Dissolution of a drop on a liquid surface leading to surface waves and interfacial turbulence," *Journal of Colloid and Interface Science*, vol. 191, no. 1, pp. 65 – 80, 1997.

[79] D. Sharp, "An overview of rayleigh-taylor instability," *Physica D: Nonlinear Phenomena*, vol. 12, no. 1–3, pp. 3 – 18, 1984.

[80] Y. Gaponenko and V. Shevtsova, "Effects of vibrations on dynamics of miscible liquids," *Acta Astronautica*, vol. 66, no. 1–2, pp. 174 – 182, 2010.

[81] S. Vanaparthy, E. Meiburg, and D. Wilhelm, "Density-driven instabilities of miscible fluids in a capillary tube: linear stability analysis," *Journal of Fluid Mechanics*, vol. 497, pp. 99 – 121, 2003.

[82] S. Vanaparthy and E. Meiburg, "Variable density and viscosity, miscible displacements in capillary tubes," *European Journal of Mechanics - B/Fluids*, vol. 27, no. 3, pp. 268 – 289, 2008.

[83] N. Eustathopoulos, G. Nicholas, and B. Drevet, *Wettability at High Temperatures*. Pergamon Materials Series, Elsevier Science, 1999.

[84] A. A. Bhuiyan and J. Naser, "Development of 3d transient wall filming mechanism during combustion by coupling eulerian-lagrangian approach and particle-wall interaction model," *Applied Thermal Engineering*, vol. 112, pp. 911 – 923, 2017.

[85] M. Khosravi, A. Bahramian, M. Emadi, B. Rostami, and E. Roayaie, "Mechanistic investigation of bypassed-oil recovery during co_2 injection in matrix and fracture," *Fuel*, vol. 117, pp. 43–49, 2014.

[86] N. V. Lisitza and Y.-Q. Song, "Manipulation of the diffusion eigenmodes in porous media," *Phys. Rev. B*, vol. 65, p. 172406, Apr 2002.

[87] J. Lewandowska, A. Szymkiewicz, K. Burzyński, and M. Vauclin, "Modeling of unsaturated water flow in double-porosity soils by the homogenization approach," *Advances in Water Resources*, vol. 27, no. 3, pp. 283 – 296, 2004.

[88] J. Bear and A. Cheng, *Modeling Groundwater Flow and Contaminant Transport*. Theory and Applications of Transport in Porous Media, Springer Netherlands, 2010.

[89] B. Ghanbarian, V. Taslimitehrani, G. Dong, and Y. A. Pachepsky, "Sample dimensions effect on prediction of soil water retention curve and saturated hydraulic conductivity," *Journal of Hydrology*, vol. 528, pp. 127 – 137, 2015.

[90] P. M. Nguyen, J. D. Pue, K. V. Le, and W. Cornelis, "Impact of regression methods on improved effects of soil structure on soil water retention estimates," *Journal of Hydrology*, vol. 525, pp. 598 – 606, 2015.

[91] U. Hornung, *Homogenization and Porous Media*. Interdisciplinary Applied Mathematics, Springer New York, 2012.

[92] E. W. Washburn, "The dynamics of capillary flow," *Phys. Rev.*, vol. 17, pp. 273–283, Mar 1921.

[93] I. Fatt, "The network model of porous media," *AIME petroleum transactions*, pp. 144–159, 1956.

[94] S. Bryant, P. King, and D. Mellor, "Network model evaluation of permeability and spatial correlation in a real random sphere packing," *Transport in Porous Media*, vol. 11, no. 1, pp. 53–70, 1993.

[95] M. Vanderlaan and S. V. Sciver, "He {II} heat transfer through random packed spheres: Pressure drop," *Cryogenics*, vol. 63, no. 0, pp. 37 – 42, 2014.

[96] V.Joekar-Niasar and S. M.Hassanizadeh, "Analysis of fundamentals of two-phase flow in porous media using dynamic pore-network models: A review," *Critical Reviews in Environmental Science and Technology*, vol. 42, no. 18, pp. 1895–1976, 2012.

[97] A. Sakhaee-Pour and S. L. Bryant, "Pore structure of shale," *Fuel*, vol. 143, no. 0, pp. 467 – 475, 2015.

[98] V. Joekar-Niasar and S. Hassanizadeh, *Analysis of Fundamentals of Two-Phase Flow in Porous Media Using Dynamic Pore-Network Models: A Review*. 2012.

[99] S. Amin, "Review on biofuel oil and gas production processes from microalgae," *Energy Conversion and Management*, vol. 50, no. 7, pp. 1834 – 1840, 2009.

[100] C. Dayananda, R. Sarada, S. Bhattacharya, and G. Ravishankar, "Effect of media and culture conditions on growth and hydrocarbon production by botryococcus braunii," *Process Biochemistry*, vol. 40, no. 9, pp. 3125 – 3131, 2005.

[101] P. Nautiyal, K. A. Subramanian, and M. G. Dastidar, "Kinetic and thermodynamic studies on biodiesel production from spirulina platensis algae biomass using single stage extraction-transesterification process," *Fuel*, vol. 135, pp. 228–234, 2014.

[102] R. Halim, B. Gladman, M. K. Danquah, and P. A. Webley, "Oil extraction from microalgae for biodiesel production," *Bioresource Technology*, vol. 102, pp. 178–185, 2011.

[103] S. Fujikawa, T. Yano, and M. Watanabe, *Vapor-Liquid Interfaces, Bubbles and Droplets: Fundamentals and Applications*. Heat and Mass Transfer, Springer Berlin Heidelberg, 2011.

[104] J. Brackbill, D. Kothe, and C. Zemach, "A continuum method for modeling surface tension," *Journal of Computational Physics*, vol. 100, no. 2, pp. 335 – 354, 1992.

[105] N. Moelans, B. Blanpain, and P. Wollants, "An introduction to phase-field modeling of microstructure evolution," *Calphad*, vol. 32, no. 2, pp. 268 – 294, 2008.

[106] A. Sheikhi and A. Ecder, "Level set analysis of two-fluid interfacial flows," *Procedia Computer Science*, vol. 18, pp. 2420 – 2423, 2013. 2013 International Conference on Computational Science.

[107] E. Olsson and G. Kreiss, "A conservative level set method for two phase flow," *Journal of Computational Physics*, vol. 210, no. 1, pp. 225 – 246, 2005.

[108] E. Olsson, G. Kreiss, and S. Zahedi, "A conservative level set method for two phase flow {II}," *Journal of Computational Physics*, vol. 225, no. 1, pp. 785 – 807, 2007.

[109] D. Lamorgese, Andrea G.and Molin and R. Mauri, "Phase field approach to multiphase flow modeling," *Milan Journal of Mathematics*, vol. 79, no. 2, pp. 597–642, 2011.

[110] J. D. van der Waals, "The thermodynamic theory of capillarity under the hypothesis of a continuous variation of density," *Journal of Statistical Physics*, vol. 20, no. 2, pp. 200–244, 1979.

[111] J. W. Cahn and J. E. Hilliard, "Free energy of a nonuniform system. i. interfacial free energy," *The Journal of Chemical Physics*, vol. 28, no. 2, pp. 258–267, 1958.

[112] J. W. Cahn and J. E. Hilliard, "Free energy of a nonuniform system. iii. nucleation in a two component incompressible fluid," *The Journal of Chemical Physics*, vol. 31, no. 3, pp. 688–699, 1959.

[113] J. Lowengrub and L. Truskinovsky, "Quasi-incompressible cahn-hilliard fluids and topological transitions," *Royal Society of London Proceedings Series A*, vol. 454, pp. 2617–2654, Oct. 1998.

[114] A. Umantsev, "Thermal effects in dynamics of interfaces," *The Journal of Chemical Physics*, vol. 116, no. 10, 2002.

[115] L. P. Csernai, J. I. Kapusta, and E. Osnes, "Domain wall dynamics of phase interfaces," *Phys. Rev. D*, vol. 67, p. 045003, Feb 2003.

[116] B. Nestler and A. Choudhury, "Phase-field modeling of multi-component systems," *Current Opinion in Solid State and Materials Science*, vol. 15, no. 3, pp. 93 – 105, 2011. Applications of Phase Field Modeling in Materials Science and Engineering.

[117] I. Singer-Loginova and H. M. Singer, "The phase field technique for modeling multiphase materials," *Reports on Progress in Physics*, vol. 71, p. 106501, 2008.

[118] P. C. Hohenberg and B. I. Halperin, "Theory of dynamic critical phenomena," *Rev. Mod. Phys.*, vol. 49, pp. 435–479, Jul 1977.

[119] S. Chan, "Steady state kinetics of diffusionless first order phase transformations," *The Journal of Chemical Physics*, vol. 67, no. 12, 1977.

[120] H. Metiu, K. Kitahara, and J. Ross, "A derivation and comparison of two equations (landau–ginzburg and cahn) for the kinetics of phase transitions," *The Journal of Chemical Physics*, vol. 65, no. 1, pp. 393–396, 1976.

[121] H. Metiu, K. Kitahara, and J. Ross, "Stochastic theory of the kinetics of phase transitions," *The Journal of Chemical Physics*, vol. 64, no. 1, pp. 292–299, 1976.

[122] A. Vorobev, "Boussinesq approximation of the cahn-hilliard-navier-stokes equations," *Phys. Rev. E*, vol. 82, p. 056312, Nov 2010.

[123] L. L. Lewis, C. S. DeBisschop, J. A. Pojman, and V. A. Volpert, "Isothermal frontal polymerization: Confirmation of the mechanism and determination of factors affecting the front velocity, front shape, and propagation distance with comparison to mathematical modeling," *Journal of Polymer Science Part A: Polymer Chemistry*, vol. 43, no. 23, pp. 5774–5786, 2005.

[124] L. L. Lewis, K. N. Massey, E. R. Meyer, J. R. McPherson, and J. S. Hanna, "New insight into isothermal frontal polymerization models: Wiener's method to determine the diffusion coefficients for high molecular-weight poly(methyl methacrylate) with neat methyl methacrylate," *Optics and Lasers in Engineering*, vol. 46, no. 12, pp. 900 – 910, 2008. Diffusion Measurements by Optical Methods: Recent Advances and Applications.

[125] B. A. Miller-Chou and J. L. Koenig, "A review of polymer dissolution," *Progress in Polymer Science*, vol. 28, no. 8, pp. 1223 – 1270, 2003.

[126] T. Alfrey, E. F. Gurnee, and W. G. Lloyd, "Diffusion in glassy polymers," *Journal of Polymer Science Part C: Polymer Symposia*, vol. 12, no. 1, pp. 249–261, 1966.

[127] D. S. Cohen, "Theoretical models for diffusion in glassy polymers. ii," *Journal of Polymer Science: Polymer Physics Edition*, vol. 22, no. 6, pp. 1001–1009, 1984.

[128] D. Cohen and J. A. White, "Sharp fronts due to diffusion and viscoelastic relaxation in polymers," *SIAM Journal on Applied Mathematics*, vol. 51, no. 2, pp. 472–483, 1991.

[129] D. A. Edwards and D. S. Cohen, "An unusual moving boundary condition arising in anomalous diffusion problems," *SIAM Journal on Applied Mathematics*, vol. 55, no. 3, pp. pp. 662–676, 1995.

[130] D. A. Vorotnikov, "Weak solvability for equations of viscoelastic diffusion in polymers with variable coefficients," *Journal of Differential Equations*, vol. 246, no. 3, pp. 1038 – 1056, 2009.

[131] T. Cosgrove, *Colloid Science: Principles, Methods and Applications*. Wiley, 2010.

[132] J. Crank, *The Mathematics of Diffusion*. Oxford science publications, Clarendon Press, 1979.

[133] J. Ferreira, M. Grassi, E. Gudino, and P. de Oliveira, "A new look to non-fickian diffusion," *Applied Mathematical Modelling*, vol. 39, pp. 194–204, 2014.

[134] O. Zikanov, *Essential Computational Fluid Dynamics*. Wiley, 2010.

[135] A. Maeda, N. Fujisawa, T. Yamagata, and H. Muramatsu, "Characterization of exchange flow in vertical pipes of circular and square cross-sections under unstable density gradient," *International Communications in Heat and Mass Transfer*, vol. 82, no. Supplement C, pp. 81 – 88, 2017.

[136] A. Roshchin and L. Truskinovskii, "Model of a weakly non-local relaxing compressible medium," *Journal of Applied Mathematics and Mechanics*, vol. 53, no. 6, pp. 715 – 720, 1989.

[137] A. Mouahid, D. Bessieres, F. Plantier, and G. Pijaudier-Cabot, "A thermostated coupled apparatus for the simultaneous determination of adsorption isotherms and differential enthalpies of adsorption at high pressure and high temperature," *Journal of Thermal Analysis and Calorimetry*, vol. 109, no. 2, pp. 1077–1087, 2012.

[138] A. Umantsev, "Thermal effects in dynamics of interfaces," *The Journal of Chemical Physics*, vol. 116, no. 10, pp. 4252–4265, 2002.

[139] T. P. Lyubimova, E. S. Sadilov, and S. A. Prokopev, "Onset of soret-induced convection in a horizontal layer of ternary fluid with fixed vertical heat flux at the boundaries," *The European Physical Journal E*, vol. 40, no. 2, p. 15, 2017.

[140] L. Yacine, A. Mojtabi, R. Bennacer, and A. Khouzam, "Soret-driven convection and separation of binary mixtures in a horizontal porous cavity submitted to cross heat fluxes," *International Journal of Thermal Sciences*, vol. 104, pp. 29 – 38, 2016.

[141] A. Umantsev, "Modeling of intermediate phase growth," *Journal of Applied Physics*, vol. 101, no. 2, p. 024910, 2007.

[142] S. Riahi, W. Y. Saman, F. Bruno, M. Belusko, and N. Tay, "Comparative study of melting and solidification processes in different configurations of shell and tube high temperature latent heat storage system," *Solar Energy*, vol. 150, pp. 363 – 374, 2017.

[143] J. Liu, C. M. Landis, H. Gomez, and T. J. Hughes, "Liquid–vapor phase transition: Thermomechanical theory, entropy stable numerical formulation, and boiling simulations," *Computer Methods in Applied Mechanics and Engineering*, vol. 297, pp. 476 – 553, 2015.

[144] D. Jamet, O. Lebaigue, N. Coutris, and J. Delhaye, "The second gradient theory: a tool for the direct numerical simulation of liquid–vapor flows with phase-change," *Nuclear Engineering and Design*, vol. 204, no. 1, pp. 155 – 166, 2001.